UNIVERSITÀ DEGLI STUDI DI PADOVA

DIPARTIMENTO DI INGEGNERIA CIVILE, EDILE E AMBIENTALE

Department Of Civil, Environmental and Architectural Engineering

Corso di Laurea Magistrale in Environmental Engineering

TESI DI LAUREA

3D Modelling of Enhanced Groundwater Dynamics in Artificial Salt Marshes of the Venice Lagoon

Supervisor:	Candidate:
Chiar.mo Prof. PIETRO TEATINI	MARIA TEODORO
	2122117

ANNO ACCADEMICO 2024-2025

ABSTRACT

Salt marshes are coastal wetlands that provide essential ecosystem services, such as wave attenuation, sediment trapping, nutrient buffering, and carbon sequestration. Despite their recognized value, they have undergone extensive decline in recent decades, making their conservation and restoration a global priority. Salt marsh restoration is a common practice to recreate a part of these landforms lost over the last decades because they may have eroded or drowned. However, these areas often have no vegetation, as the low elevation of the deposited sediments exposes the marsh to frequent and longer inundation periods and the absence of a creek network prevents proper soil desaturation. Indeed, creeks play a main role in natural salt marshes to facilitate groundwater drainage when tidal levels lower and marsh platform emerges above the mean sea level. The presence of internal channels is recognized as a crucial factor for the establishment of vegetation. Recent experimental efforts have focused on facilitating the formation of tidal creeks in restored or artificial salt marshes. This study aims to apply a three-dimensional variable-saturated groundwater flow model to simulate and visualize drainage dynamics within a real artificial salt marsh in the Venice Lagoon. Simulations were conducted using the GroundWater Simulator. Initially, modelling has been carried out on an idealised marsh and subsequently on a real artificial marsh, assessing the impact of tidal creek networks on saturation and pressure head evolution. Both sinusoidal and real tides were investigated, and the influence of different boundary conditions was also evaluated. Results showed that channels significantly enhanced drainage, reducing full saturation duration and allowing the marsh to reach lower saturation values. Simulations with real tidal regimes revealed more complex saturation patterns, where only the highest tidal peaks induced saturation of the whole marsh body and the creek allows subsequent decrease of the water content in the area surrounding the drainage element. A model sensitivity analyses revealed that mesh refinement, which is a critical issue in modelling the evolution of the water content in large 3D landform domain, affects result accuracy. Moreover, as expected, higher hydraulic conductivity of soil used to restore a salt marsh accelerates drainage and expands the desaturated area. Overall, this study provides insights to guide restoration practices, improving salt marsh resilience and mitigating sea level rise impacts.

TABLE OF CONTENTS

1. Introduction

Salt marshes are coastal wetlands situated at the boundary between terrestrial environments and saline or brackish waters, where they are periodically inundated by tidal flows (Marani et al., 2006). They hold significant social, economic, ecological, and geomorphological value, providing a wide range of ecosystem services, including attenuation of tidal currents and wave energy, sediment trapping, buffering of nutrient fluxes from land to sea and carbon sequestration. In addition, salt marshes act as vital nursery and habitat for diverse coastal biota, vegetation, and benthic communities (Zoccarato et al., 2022).

Despite their recognized value, salt marshes worldwide have undergone extensive decline in recent decades due to anthropogenic pressures such as land reclamation, pollution, industrial development, and poorly managed coastal engineering interventions (Gedan et al. 2009). These losses are further exacerbated by sea-level rise and land subsidence, which threaten the capacity of marshes to maintain their elevation relative to the mean sea level (Zoccarato et al., 2022; Carbognin et al., 2005). Consequently, their conservation and restoration have become a global priority, especially in regions where these habitats constitute a fundamental component of environmental and cultural heritage.

The Venice Lagoon represents a unique case study for examining the dynamics, degradation, and restoration of salt marsh ecosystems. To protect its fragile environment, the lagoon has undergone intense transformations over centuries, from river diversions and land reclamation to industrial exploitation and modern flood-protection infrastructure. In this context, restoration practices, including the creation and management of artificial salt marshes, have emerged as adaptive strategies to safeguard both ecological integrity and coastal resilience. The study focuses on a real salt marsh, which is analysed in detail as a representative case study.

1.1 Salt marshes and their ecosystem services

Salt marshes are landforms characterized by a complex morphology resulting from the continuous interaction between sediment deposition, driven by marine and fluvial inputs, sediment erosion, primarily caused by wave action and tidal forces (Marani et al., 2006), and sediment auto-compaction, enhanced by the large porosity and compressibility of the top sedimentary sequence (Zoccarato and Teatini, 2017). Tidal fluctuation serves as one of the dominant environmental driver, regulating not only sediment dynamics but also key parameters such as soil salinity and moisture content. The interaction of hydrodynamic processes with the irregular topography of the marsh surface and distinct morphological features generates a heterogeneous network of microhabitats that supports ecological richness and functional diversity of the marsh ecosystem (Figure 1).

Figure 1: Salt marshes of the Venice lagoon

The stability and resilience of these ecosystems are largely governed by their vegetation, which plays a central role in shaping both physical and ecological processes. Although salt marsh environments are characterized by soils flooding and high salinity, which pose significant challenges to plant survival, certain species have developed specialized adaptations to thrive under these conditions. Halophytes, in particular, are capable of tolerating elevated salinity levels and tend to form distinct patches, resulting in a characteristic zonation pattern across the marsh. This zonation has been closely linked to topographic elevation, with species distribution strongly influenced by variations in submersion duration associated with differences in soil elevation (Ursino et al., 2004).

For thousands of years, salt marshes have provided coastal protection from waves and storm surge, as well as from coastal erosion. The presence and structure of marsh vegetation are central to the long-term stability of tidal marshes. Vegetation stabilizes surface sediments, increases friction to hydrodynamic flow and reduces water sediment transport capacity, thereby promoting sediment deposition. Furthermore, it inhibits the formation of wind-induced waves, reducing sediment resuspension (Ursino et al., 2004). Compared to unvegetated mudflats, vegetated marshes also contribute to attenuating both the height and duration of storm surges by increasing water uptake and storage capacity (Barbier et al., 2011).

Moreover, wetlands have a high and long-term capacity to improve water quality. They effectively reduce nutrient loads in both surface and subsurface runoff by removing excess nitrate and phosphorus from through-flowing water. Among these functions, nitrate removal from subsurface runoff under anaerobic soil conditions is the most extensively documented. This process primarily occurs through denitrification, where microbial decomposition of organic matter takes place in oxygen-deprived environments. In this context, nitrate serves as an electron acceptor and is ultimately converted into atmospheric nitrogen (N_2), which is then released from the system. In addition to microbial processes, vegetation also plays a role in nutrient uptake as water flows through the marsh, contributing to long-term nitrogen storage. Phosphorus removal has likewise been observed in riparian habitats, driven primarily by sedimentation, adsorption to soil particles, and plant assimilation (Verhoeven et al., 2005).

Lastly, wetlands are recognized as significant carbon sinks and global climate regulators (Mitsch and Gosselink, 2007). In salt marshes, the anoxic conditions of the soil enable long-term storage of carbon captured through photosynthesis. Rather than cycling back into the atmosphere within decades, this carbon is often buried as slowly decaying peat, effectively transferring it from the short-term to the long-term carbon cycle. This distinctive capacity for durable carbon sequestration has positioned salt marshes as a valuable nature-based solution to climate change, with the potential to store large quantities of carbon over prolonged periods of time (Barbier et al., 2011).

1.2 Spatial distribution and conservation challenges

Despite their importance, the current spatial distribution of salt marshes is quite difficult to define due to active sedimentation, changes in land use, periodic tidal inundation and diverse vegetation (Xin et al., 2022). As coastal ecosystems face increasing anthropogenic and environmental pressures, comprehensive global data on the distribution and extent of salt marshes are needed to enhance the understanding of these ecosystems and the benefits they provide. Such data can support resource management, inform policy and decision-making, and facilitate monitoring progress towards conservation goals set by multilateral environmental agreements (McOwen et al., 2017).

Estimates of global salt marsh coverage have varied widely, ranging from 22,000 to 400,000 km^2. However, more recent assessments suggest a global extent of approximately 54,951 km^2, spread across

43 countries and territories (McOwen et al., 2017). As shown in Figure 2, salt marshes are typically found in estuaries, tidal inlets, embayments, and open coasts where sufficient intertidal accommodation space exists. Globally, salt marshes are most extensive in North and Central America, Oceania, and Northern Asia. A significant majority, approximately 55.1%, of the world's salt marshes is located in the northern temperate zone (23.5°–66.5°N), while an additional 13.4% lies in the northern frigid zone (66.5°–73.6°N). In contrast, salt marshes are relatively rare in subtropical and tropical regions, where mangrove ecosystems dominate (Xin et al., 2022).

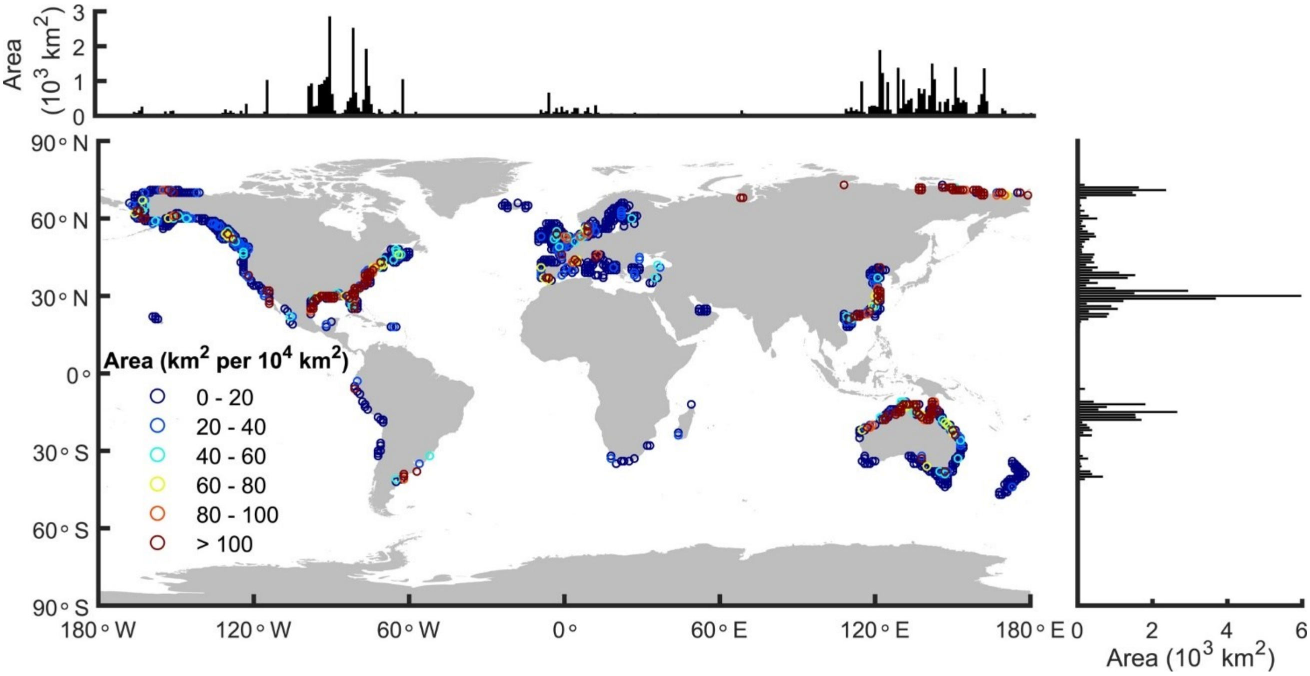

Figure 2: Global distribution of salt marshes based on data from McOwen et al. (2017). The latitudinal and longitudinal areal extent of salt marshes per 1° grid cell are shown in above and right subplots, respectively. (after Xin et al., 2022).

At the national level, the United States, Australia, and Russia hold the largest salt marsh areas, accounting for roughly 70% of the global total. The United States alone hosts 18,849 km² (34.7%), followed by Australia with 13,259 km² (24.1%) and Russia with 7,007 km² (12.8%) (McOwen et al., 2017).

Coastal marshes have experienced significant global decline over recent decades, with an estimated loss of approximately 35% between 1970 and 2015 (Ramsar Convention on Wetlands, 2018). Historically, these ecosystems have been endangered by poorly regulated coastal management practices. Large areas have been reclaimed for agriculture, urban development, and industrial use, while others have been degraded by pollution from upstream agricultural runoff and industrial activity. Despite increasing recognition of their ecological value, land conversion for industry, port infrastructure, transportation networks, and waste disposal remains a persistent threat (Gedan et al., 2009).

In addition to anthropogenic pressures, climate change poses a growing risk to the long-term survival of salt marshes. Sea-level rise contributes to both the erosion and submersion of these intertidal habitats, particularly when they cannot maintain their elevation relative to rising water levels. The persistence of coastal marshes under these conditions depends largely on their ability to accumulate sediment and organic material fast enough to keep pace with relative sea-level (RSL) rise. This vertical accretion is governed by a combination of physical (e.g., sediment deposition during tidal flooding), biological (e.g., plant productivity), and chemical (e.g., decomposition) processes, all of which are tightly linked to the marsh's position within the tidal frame (Zoccarato et al., 2022).

Despite ongoing challenges, there has been a growing awareness, among both environmentalists and the broader public, of the crucial role salt marshes play in supporting biodiversity, enhancing ecological productivity, and providing valuable ecosystem services. Recently, this shift has driven greater efforts in salt marsh conservation, restoration, and adaptive management (Petillon, 2023).

1.3 Artificial salt marshes as nature-based solutions

Recognizing their ecological and protective value, artificial salt marshes have been progressively incorporated into the Nature-Based Solutions (NBS) framework. According to the IUCN (2016), NBS are defined as “actions to protect, sustainably manage, and restore natural or modified ecosystems that address societal challenges effectively and adaptively, while simultaneously providing human well-being and biodiversity benefits.” Within this context, nature-based coastal defence is gaining importance as an approach that not only protects shorelines but also enhances biodiversity, mitigates climate change impacts, and sustains vital ecosystem services. Unlike conventional engineering, which often relies on rigid structures, nature-based strategies offer adaptable, multifunctional benefits. Scaling up these approaches from isolated pilot sites to landscape-level implementation holds significant potential for expanding coastal wetland areas and strengthening ecological resilience. However, the implementation of nature-based projects is frequently hindered by practical, institutional, and regulatory challenges that must be addressed (Baptist et al., 2021).

2. Study area: the Venice lagoon

Located in northeastern Italy, the Venice Lagoon (Figure 3) is the country's largest lagoon and one of the most extensive in the Mediterranean region, covering an area of approximately 550 km^2 (Day Jr et al., 1999). Hydrologically connected to the Adriatic Sea through three inlets, the lagoon has undergone significant transformations in its sediment dynamics and hydrological balance over the past several centuries (Gatto and Carbognin, 1981). Historically, the Adige, Bacchiglione, Brenta, Sile, and Piave rivers discharged directly into the lagoon, but, mainly during 16th and 17th centuries, they were rerouted to flow into the sea (Bondesan and Furlanetto, 2012). As a result, fluvial sediment input has been greatly diminished, with current contributions limited to a few minor rivers carrying a combined flow of roughly 30 m^3/s (Bendoricchio et al., 1993). These alterations have led to a net sediment loss from the system, estimated at around 10^6 m^3/year (Bettinetti et al., 1995).

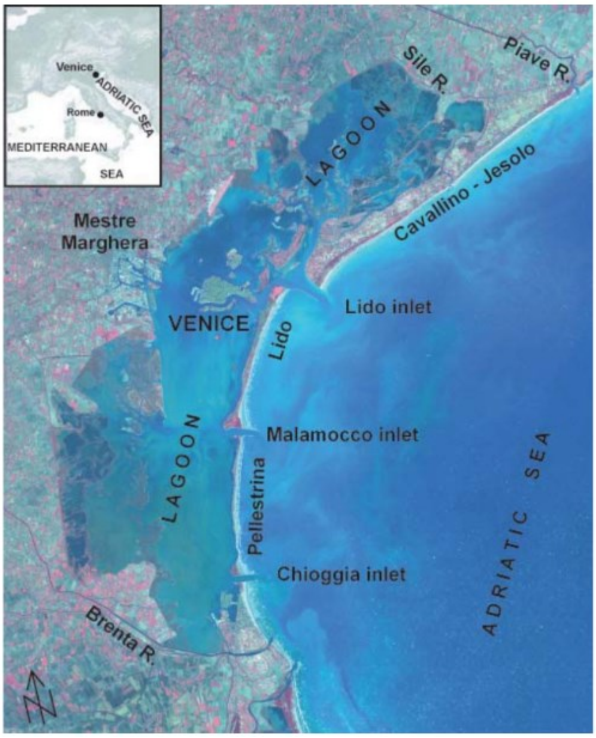

Figure 3: ASTER image of the Venice Lagoon and its surrounding mainland. Main localities are indicated (after Brambati et al., 2003)

The morphology of the lagoon consists of a large central water body of about 370 km² surrounded by extensive intertidal salt marshes (Day Jr et al., 1999). With an average depth of 1.1 me and a tidal range of 0.6–1 m, approximately 50 km² of tidal flats are exposed at low tide. Subtidal regions support a mix of macroalgae and seagrasses, including *Zostera marina*, *Zostera noltii*, and *Cymodocea nodosa*. The salt marshes are vegetated by halophytic species such as *Limonium serotinum*, *Puccinellia palustris*, *Arthrocnemum fruticosum*, and *Spartina maritima*, contributing to the area's high productivity and ecological value (Géhu et al., 1984).

Over the past century, the extent of salt marshes in the lagoon has declined dramatically, passing from approximately 12,000 ha to just 4,000 ha, largely as a result of land reclamation, industrial development, pollution, dig of navigable channels, and both natural and human-induced subsidence (Favero, 1992; Runca et al., 1996). This loss has raised concerns about the resilience of coastal ecosystems and has highlighted the need for integrated restoration efforts.

2.1 Historical evolution

The Venice lagoon was formed during the Late Holocene transgression (about 6000 years BP) on low-lying terrains that were already partly inhabited by human communities (Barbero et al., 2004). Its origin is linked to the Flandrian transgression, when rising sea levels shaped a coastal line close to the present one. Extending into the sea, the deltas of the main Venetian rivers, particularly the Piave and Adige, supplied sediments that played a key role in shaping the littoral, which progressively enclosed the newly formed lagoon (Gatto and Carbognin, 1981). Early reconstructions suggest that the original lagoon was smaller than today, concentrated mainly behind the present littoral, whose position has remained essentially unchanged over time (Gatto e Previatello, 1974). Two main processes governed the early evolution of the lagoon:

1. Alluvial supply from rivers: Adige, Bacchiglione, Brenta, Sile, and Piave rivers continuously delivered sediments to the lagoon. The filling rate exceeded the natural subsidence of about 1.3 mm/year, mainly caused by the consolidation of late alluvial deposits.
2. Coastal feeding and silting of inlets: strong coastal feeding promoted the gradual silting-up of lagoon inlets (historically about eight openings around 1000 AD), the emergence of new sandbanks, and the creation of new external lagoons (Gatto, 1981).

The combined effect of these two processes created a persistent threat of silt-up, which would have eventually converted the lagoon into dry land, merging it with the Venetian plain. As a response, significant human intervention began in the fourteenth century, when it was decided to divert the major tributaries directly into the sea. This massive undertaking triggered a reversal of the lagoon's natural evolution, as without the steady input of alluvial sediments natural subsidence was no longer balanced, causing the lagoon bed and surrounding lands to sink more deeply. As a result, stretches of water expanded, some islands disappeared, and former agricultural-woodland areas along the lagoon margins were submerged, giving way to marshy intertidal flats. The diversion of fresh water also eliminated the lagoon's brackish characteristics, making it increasingly saline, and saltwater seepage into the younger bottom soils further lowered the lagoon floor. Over this period, the lagoon both deepened and widened until it reached approximately its present configuration, as shown in Figure 4 (Gatto and Carbognin, 1981).

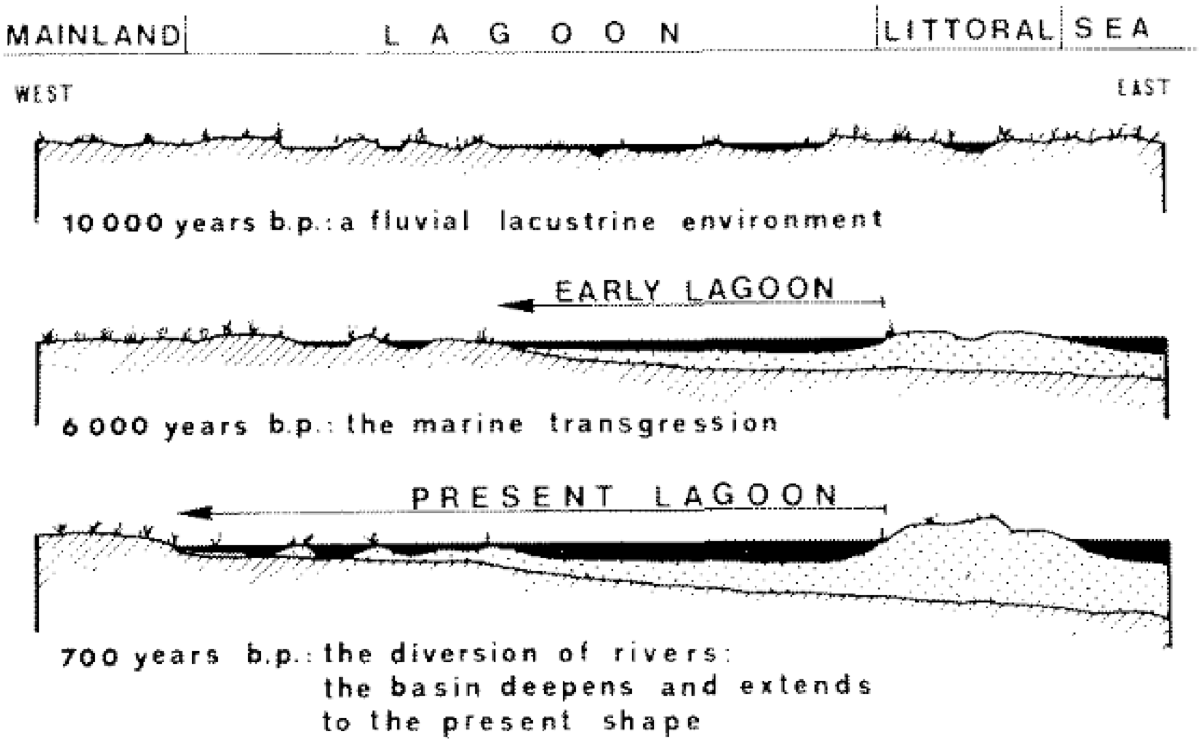

Figure 4: Origin and evolution of the Venice Lagoon. A cross section schematic representation of its middle part (after Gatto and Previatello, 1974).

From the beginning of 1800 onward, human activity began to reshape the Venetian lagoon with more intensity (Avanzi et al., 1980). Large portions of its surface were reclaimed for agriculture, fish farming, and new industrial and urban districts purposes. At the same time, major alterations were made to its natural inlets. The eight original sea openings were reduced to three, Lido, Malamocco, and Chioggia, and new deep canals for internal navigation were dug to serve the industrial harbour adequately, dramatically altering the hydraulic balance of the lagoon. The most notable of these is the "Canale dei Petroli", which connects Marghera to Malamocco's inlet (Figure 5).

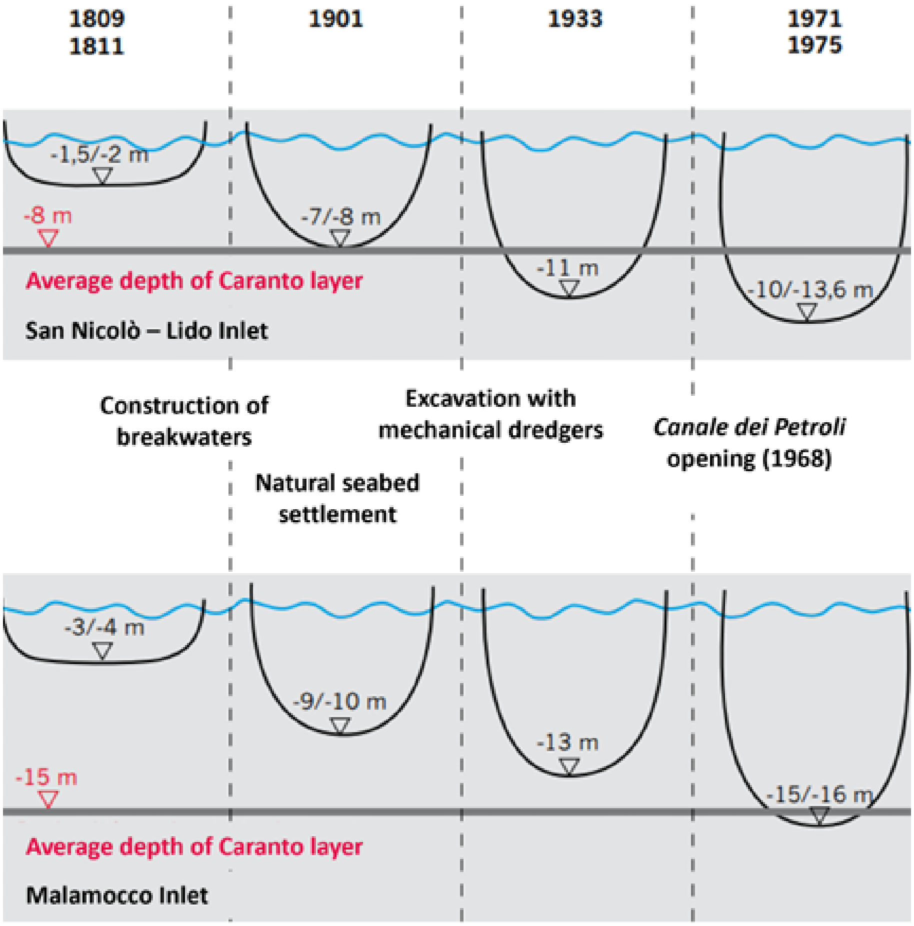

Figure 5: Evolution of the average depth of the three inlets (after Boato, n.d.)

Additionally, the industrial water supply was provided by a rash exploitation of the underground water inducing a serious sinking which consequently deepened the bottom of the basin even further. Progressive exploitation of the six artesian aquifers, located in the upper 350 m of the 1000-m-thick unconsolidated Venetian Quaternary formation, began in the 1930s with the first industrial installations, grew with the post-war industrial development, and peaked in the 1950-1970 period, together with the subsidence velocity (η mean $\cong$ 2.5 mm/yr). The anthropogenic geomechanical subsidence induced by groundwater over-exploitation, together with the geological subsidence and the eustatic sea level rise have induced a loss in land elevation over the last 100 years of about 23 cm, has shown in Figure 6.

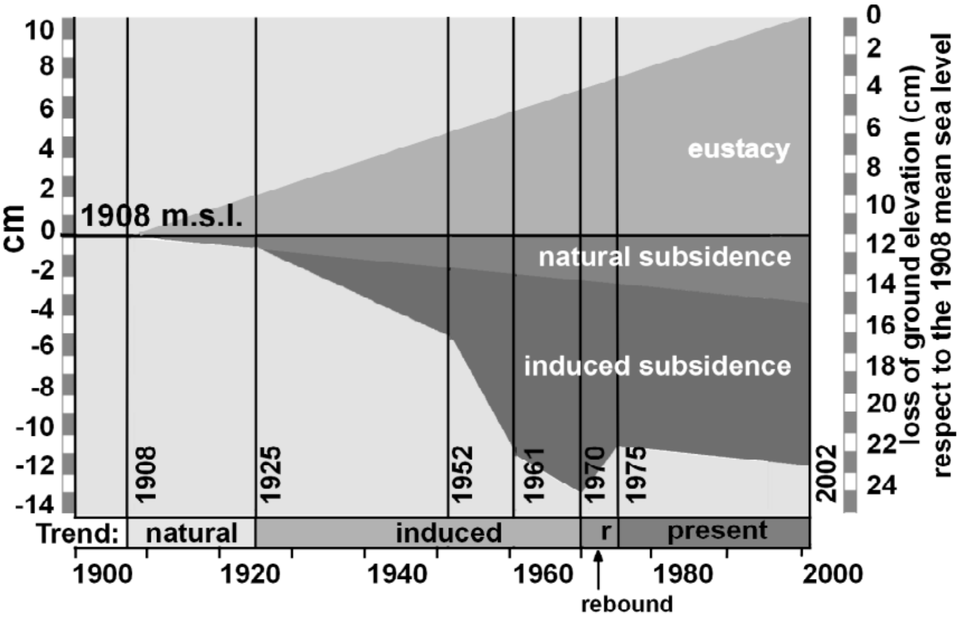

Figure 6: Graphical representation of the three components of the relative ground elevation loss at Venice consisting of about 3 cm of natural subsidence, 9 cm of anthropogenic subsidence, and 11 cm of sea level rise (after Carbognin et al., 2005)

Today, the Venice lagoon is divided into three basins (North, Central, South), one for each of the three inlets to the sea, with limited exchanges between them. The morphological changes affecting the lagoon do not occur uniformly across these three areas. The Central lagoon, the most heavily urbanized, is the one most impacted by erosion caused by wind-generated waves and human activities; the Southern lagoon is characterized by dynamics dominated by the excavation of large navigation channels; finally, the Northern lagoon has the most well-preserved salt marsh system, although in recent decades it has been undergoing significant morphological and biological changes (Istituto Veneto, n.d.).

Finally, the most recent interventions on the lagoon are also described. After the *Acqua Granda* (exceptional high tide) of 1966, when the water level reached a record 194 cm above the Venice datum, and the severe flooding of 2019, with a peak of 187 cm, urgent measures were required to safeguard the city and its fragile environment. To adress this threat, construction of the MOSE system began in 2003, a project consisting of four barriers made up of 78 independent mobile gates capable of temporarily separating the lagoon from the sea and protecting Venice from exceptional tidal events. The barriers are located at the Lido, Malamocco, and Chioggia inlets, through which the tide flows from the Adriatic Sea into the lagoon. When inactive, the gates are filled with water and lie in housings on the seabed. In the event of particularly high tides that could cause flooding, compressed air is pumped into the gates to empty them of water (MOSE, 2025). As the water gradually exits, the gates rotate around their hinges, rising until they emerge and block the incoming tide to enter the lagoon (Figure 7).

Figure 7: MOSE barrier system (MOSE, 2025)

The primary purpose of the MOSE system is to protect Venice from flooding, a critical issue given the increasing risk of rising sea levels and the city vulnerability. However, the system's impact on the delicate ecological balance of the lagoon has been the subject of recent studies. The MOSE infrastructure was originally designed to be activated only a few times per year, with an expected closure frequency ranging between two and five events annually. However, projections under the worst climatic scenario indicate that, with the closure threshold set at 110 cm, the system could be required to operate for up to 5,000 hours per year by the end of the century, equivalent to 57% of the year (Giupponi et al., 2024). Such frequent and prolonged closures would not only challenge the system's functionality but also raise serious concerns about their ecological impacts on the lagoon, casting doubt on the long-term viability of this solution. The morphological evolution of the Venice Lagoon is primarily shaped by the redistribution of sediment resuspended within the basin. Deposition measurements under non-regulated conditions and concurrent water-level and meteorological observations show that storm-driven events contribute more than 70% of the annual sediment accumulation on marsh surfaces. This indicates that sediment accretion on salt marshes depends largely on intense, episodic storm surges rather than mild, rhythmic tidal flooding. Consequently, storm-surge barriers have the potential to significantly reduce sediment delivery to coastal wetlands, further weakening their already fragile equilibrium and amplifying the adverse effects of sea-level rise on their survival (Tognin et al., 2021).

2.2 Salt marshes classification

A lagoon is a coastal wetland connected to the sea through inlets, where the movement of water is governed by the tide. As a transitional environment between land and water, it exists in a state of constant instability: its morphology is continuously reshaped by the interplay between sediment inputs from rivers or the sea and the erosive forces of waves and tides (MOSE, 2025). Within the Venice Lagoon, the salt marsh environment is characterized by several distinct elements:

- Salt marsh (*Barena*): it is a flat and silty area of the lagoon covered by halophytic plants typical of brackish environments. It is submerged during high tide only;

- Tidal creek (*Ghebo*): a small and winding channel that runs through the salt marsh and connects its inner parts to deeper lagoon channels;
- Salt Pan (*Chiaro*): a small depression in the salt marsh where brackish water trapped during high tide mixes with rainwater to form a pond;
- Mudflat (*Velma*): a shallow muddy area characterised by soft soil that only emerges at low tide; they form a transition zone between the salt marshes and the deeper parts of the lagoon (Smart and Viñals, 2004).

The lagoon’s land system comprises all emerged areas, both natural and artificial, and accounts for about 8% of the lagoon’s total surface. The remaining 92% belongs to the water system, which is made up of canals (11.9%) as well as seabed, mudflats, and salt marshes (80.1%). Although salt marshes often rise higher above sea level than certain parts of Venice’s historic centre, they are classified within the water system due to their functional role, which is to regulate the lagoon's hydrodynamics without opposing the expansion of the tides (MOSE, 2025).

Different types of natural salt marshes differ in their origin and consequently in their characteristics and dynamics. Recognizing these differences is essential for effective conservation and management. In the Venice Lagoon, salt marshes are classified by their formation and subsequent evolution, resulting in several distinct types, each with unique features (Istituto Veneto, n.d.). The main types are outlined below:

- Lagoon-edge salt marshes: these salt marshes are the remaining visible part of the coastal plain. Constantly saturated with saline water, they can only sustain halophytic vegetation specially adapted to such harsh conditions. This kind of salt marshes are located along the Lagoon edge towards the mainland, like the ones between Campalto and the Dese area. In the past, they were directly influenced by the mainland, which supplied sediments and vegetation. Once the lagoon barrier interrupted this input, however, they entered a phase of gradual erosion.

- Internal area salt marshes: located in the inner parts of the lagoon, these marshes have a particularly complex history. Initially influenced by saline waters, they later evolved into freshwater marshes and peat bogs as rivers flowed into the lagoon. When these waterways were eventually diverted, the marshes reverted to typically lagoonal conditions. Today, they are mainly found in the southern lagoon, between Marghera and Chioggia. The interruption of sediment supply caused by river diversion led to a graduate lowering of the marsh surface, a process further aggravated by wave erosion and land subsidence.
- Salt marshes along the old tributaries to the lagoon: these marshes developed along the old waterways that once flowed into the lagoon, formed through ancient sediment drifts. Due to their proximity and easy access from the mainland, many of these areas have been converted into agricultural fields.
- Salt marshes along the lagoon waterways: these marshes are primarily formed from sediments transported by marine currents. As the currents slowed, suspended material settled, with additional input from the erosion of canal beds. This kind of salt marsh is typical of the northern lagoon (S. Erasmo, San Felice, San Lorenzo, and Burano), where many sediments are dropped after flowing into the Lagoon from the Lido lagoon inlet by a reduced current speed. Their morphology reflects this process: the marsh edge is taller along the side of the supplying canal and gradually lowers outward, transitioning into *velma*. These formations are absent near the Malamocco and Chioggia inlets, where incoming waters lack sufficient sediment to build such features. Today, their greatest threat is erosion caused by intense wave action from heavy boat traffic.

- Paleo salt marshes: unlike other marsh types, paleo salt marshes did not form through sediment accumulation but as a result of sea-level lowering. Their long-term persistence has been proven by traces of oxidation and preserved plant remains.

2.3 Salt marshes restoration

Following the exceptional high tide of 1966, Law No. 171 of April 16, 1973, known as the first Special Law for Venice, was introduced to address in a comprehensive way the many challenges faced by the city. The law declared the safeguarding of Venice and its lagoon to be a matter of primary national interest, and the Italian Republic committed itself to protecting the landscape, historical, archaeological, and artistic heritage of Venice and its lagoon, preserving its hydraulic balance, shielding its environment from air and water pollution, and ensuring its social and economic vitality within the broader framework of regional development and territorial planning (Article 1). To oversee and coordinate these objectives, the Commission for the Safeguarding of Venice was established. Subsequent legislation strengthened this framework: Laws No. 798 of 1984, 360 of 1991, and 139 of 1992 built upon the 1973 Special Law framework to strengthen the protection of Venice and its lagoon, providing additional measures, reinforcing institutional coordination, and ensuring the ongoing preservation of the city and its fragile environment.

Focusing on salt marshes protection and restoration, over the years many projects and different designs have been tested. Recently, the emphasis has been placed on adopting an integrated approach, which has the main objective of preventing salt marsh erosion through a series of small, spatially-diffuse soil-bioengineering protections works. These interventions are primarily implemented using semi-manual labour, ensuring that they have minimal impact on both the environment and the landscape. The long-term effectiveness of these protective measures is ensured through routine, continuous monitoring and maintenance, which are carried out consistently over time and across the entire protected area (Barausse, 2015).

There are several sediment retention structures for salt marsh edges which vary in their effectiveness against wave energy, as well as in terms of their environmental impact and durability. When intense erosion threatens the salt marsh edges, screens made of wooden poles or gabions are commonly employed. A wooden pole screen consists of poles placed side by side along the marsh edge, with a geotextile layer positioned internally, between the poles and the marsh. While this technique has been widely used over the years, it is expensive, as each meter of screen requires approximately 4-5 wooden logs, as well as heavy machinery to install the poles. Additionally, wooden pole screens tend to reflect the wave instead of absorbing its energy, creating reflected waves that erode and undermine the base, leading to depressions and triggering destructive processes in the surrounding mudflats. To overcome these challenges, gabions can be used as an alternative. Gabions are tubular structures made by natural or synthetic fibre nets filled with a variety of materials, such as sediments, wooden fibers, branches, fascines, halophyte clods, sand, stones, and shells. Placed on the tidal flats near the salt marsh edge, they are more effective at dissipating wave energy, but their longevity is highly dependent on the materials used. Gabions constructed with biodegradable materials, for example, require more frequent maintenance but are better suited to the natural dynamics of the evolving lagoon. In contrast, those made from synthetic materials are more durable but less adaptable to the changes in the lagoon's morphology. In addition to these structural protections, techniques aimed at promoting sedimentation and soil stabilisation, such as sediment pumping, the installation of sedimentation-inducing barriers, and the transplantation of vegetation, have also been implemented (Bonometto, 2003).

2.4 Artificial salt marshes: the Amira salt marsh case study

For the restoration of a salt marsh that may have collapsed or sunk, where a salt marsh once existed, more complex restoration practices are required. In these cases, artificial salt marshes are often created to replace or reconstruct the lost landform. Artificial saltmarshes are the result of successive depositions of dredged sediments removed from navigable channels within the lagoon and placed in the restoration site. For long periods of time, both during the nourishment phases and after the sediment disposal is completed, they appear as stretches of bare soil without vegetation or a creek network.

Sediments that can be used for nourishment in the Venice lagoon must comply with the "Protocollo Fanghi" ("Sludge Protocol") which establishes environmental safety criteria for the excavation, transport, and reuse of dredged materials from the Venice canals. The protocol defines the potential destinations for dredged materials, which are classified into four categories (A, B, C, and beyond C), based on the average results of chemical analyses carried out on collected samples. For projects aimed at restoring lagoon morphology, such as the reconstruction of eroded salt marshes or the recovery of depressed areas, where dredged materials may come into direct or indirect contact with lagoon waters and potentially re-enter the aquatic environment, only sediments that meet the criteria for Class A may be used. On the other hand, sediments classified as Class B or C may be used, respectively, for the recovery and restoration of lagoon islands, or for the enlargement and elevation of permanently emerged islands or inland areas adjacent to the lagoon contamination zone. Lastly, materials with contaminant concentrations exceeding the limits set for Class C, but not classified as toxic or hazardous, may still be used for raising the elevation of depressed areas located outside the lagoon (Ministero dell'Ambiente, 1993).

As previously stated, in their early stages these marshes appear as flat, bare soils with no vegetation or natural creek network. One of the main causes of these initial conditions is the low elevation of the deposited sediments, which exposes the marsh to frequent inundation and prevents proper soil desaturation. Studies have shown that artificial marshes experience significantly higher rates of subsidence compared to natural marshes, with median values decreasing from around 4 mm/year in the newest man-made marshes (2007–2008) to approximately 0.4 mm/year in older (500–1000 yr BP) natural marshes (Da Lio et al., 2018). This rapid subsidence is largely due to the auto-compaction of freshly deposited sediments, which are compressed under the weight of additional material. As the marsh loses elevation, it becomes increasingly prone to prolonged inundation, creating saturated soil conditions that hinder vegetation establishment. While salt marsh plants are adapted to tolerate high salinity and periodic flooding, they cannot survive in soils that remain almost permanently saturated, as poor drainage limits root growth and reduces soil oxygenation.

To overcome this drainage problem, the presence of internal tidal creeks is recognized as a crucial factor for the establishment of vegetation, particularly because interior marshes often exhibit greater inundation stress and lower resilience than more well-drained marsh edges (Qi and Gedan, 2025). In fact, poor drainage of these interior zones results in consistently higher water levels and slower recession at low tide (Qi and Gedan, 2025). Tidal creeks, typically absent in artificial marshes, enhance groundwater drainage during low tides and facilitate the penetration of air into the shallow soil layers where halophyte roots are concentrated. In line with this understanding, recent experimental efforts in artificial salt marshes have aimed to create openings in marsh boundaries to promote the formation of tidal creeks.

To further investigate these processes, this study aims to apply a three-dimensional variable-saturated groundwater flow model to simulate and visualize drainage dynamics within an artificial salt marsh in the Venice Lagoon. The analysis focuses on a case study of a real salt marsh, here referred as "Amira" in order to preserve confidential data. Located in the southern lagoon within the Canale Bastia area, the Amira salt marsh is a region that has been the focus of extensive and ongoing morphological restoration efforts since the early 2000s (Figure 8).

Figure 8: Map of the Venice Lagoon with location of the "Amira" salt marsh (red area); a timeline of restoration projects on the site is shown in the inset.

The modelling analysis has been performed on just a part of the marsh, on the south-west side, in the area where a channel system had developed (Figure 9). This section underwent a series of interventions that facilitated the formation of a drainage network, as the area is characterized by the absence of strong currents, which prevented significant sediment export. The initial intervention involved the creation of openings in the infill perimeter, allowing the spontaneous formation of new channels.

Subsequent works focused on excavating the channel, extending it further into the marsh to enhance drainage and water circulation.

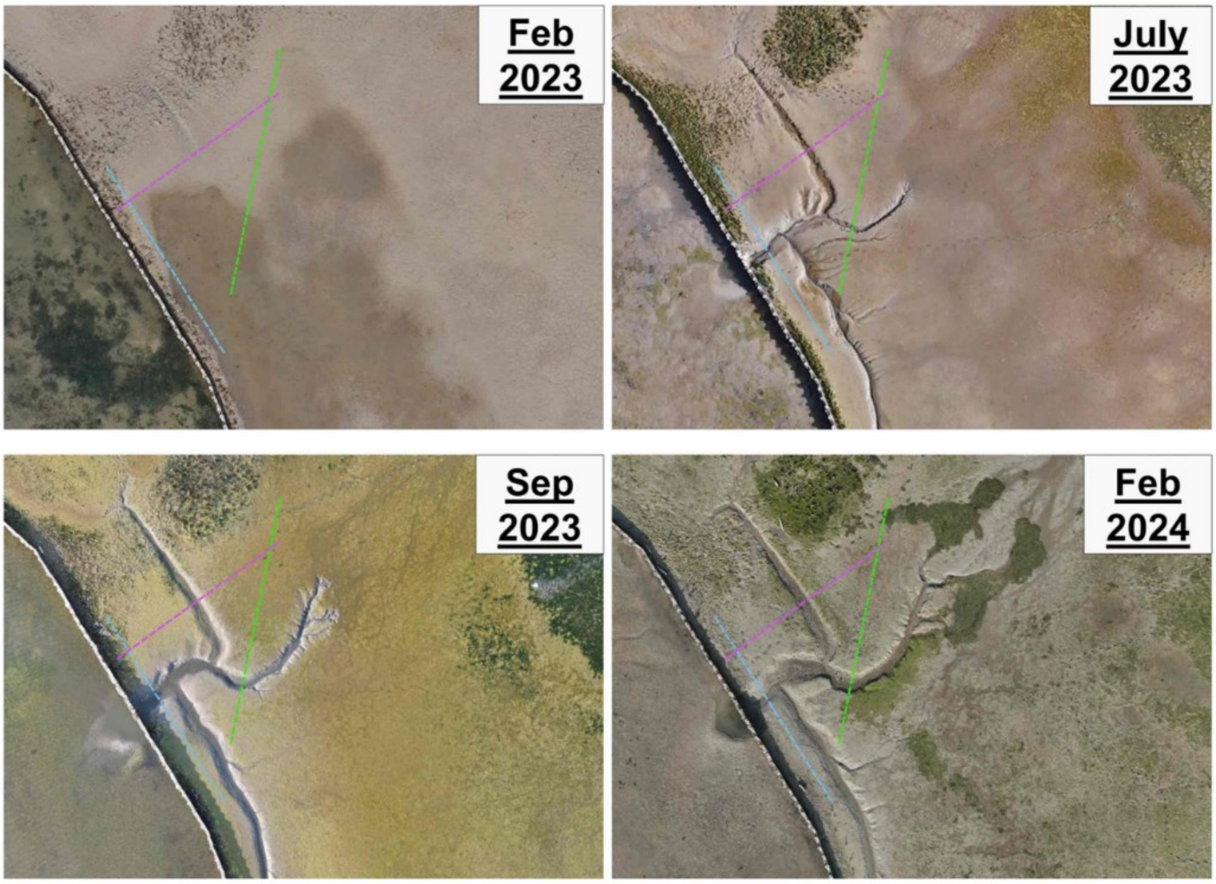

Figure 9: Orthophoto from drone of the channel evolution on an artificial salt marsh (Vital, 2024)

3. Mathematical models and methodology

The study aims to apply a 3D variable-saturated groundwater flow simulator to investigate the effects of channel creation on the drainage of an artificial salt marsh. Specifically, the primary focus is on unconfined unsaturated soils subjected to tidal inundation in salt marshes. A detailed examination of the key definitions and governing equations of water flow in porous media is provided, laying the foundation for the modelling approach and analysis.

3.1 Unsaturated zone

The unsaturated zone, or vadose zone, is the layer of porous soil between the land surface and the groundwater table in which the pore spaces are only partly filled with water, while the remaining voids contain air (USGS, 2013).

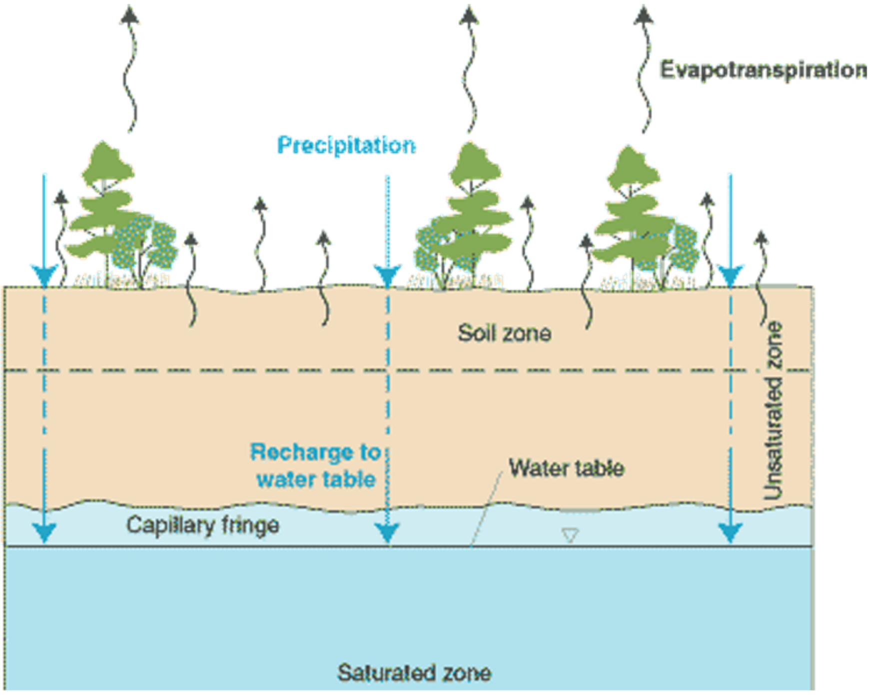

Figure 10: Schematic diagram showing a vertical section from the land surface through the vadose zone, capillary fringe, and into an unconfined aquifer (after Alley et al., 1999)

The unsaturated zone is typically divided into three subzones:

1. Soil water zone or root zone: located near the ground surface, this zone extends through the root systems of plants. It plays a critical role in vegetation growth, as plant roots require both air and water. Moisture content here is highly variable and influenced by surface conditions such as precipitation, irrigation, evaporation, and temperature. Water movement occurs both downward (infiltration) and upward (evaporation and transpiration).
2. Intermediate zone: situated between the soil water zone and the capillary fringe, this layer is often thicker in arid regions or where the water table lies deep. Moisture movement is slower, and the water content is relatively stable compared to the root zone.
3. Capillary fringe: this zone lies directly above the water table and extends to the maximum height water can rise due to capillary action, which depends on pore size distribution. In fine-grained soils, the capillary fringe can be several meters thick, while in coarse materials, it may be nearly absent. Pores in this zone are completely filled with water, and the pressure remains below atmospheric.

The combined behaviour of these three subzones governs how water is stored and moves through the unsaturated zone, influencing hydrological processes, plant growth, and groundwater recharge.

3.2 Darcy's law

Darcy's law is an equation that describes the flow of a fluid through a porous medium. This principle was formulated by Henry Darcy, based on his experiments on the flow of water through sand filters (Atangana, 2018). Using the experimental set-up shown in the Figure 11, Darcy observed that the volumetric flow rate of water through the sand filter per unit time, denoted by Q, depends on several factors:

- A: the cross-sectional area of the sand filter

- $h_1 - h_2$: the difference in piezometric head between the inlet and outlet
- L: the length of the sand filter (flow path)

From his observations, Darcy proposed that the flow rate is proportional to the cross-sectional area and the piezometric head difference, and inversely proportional to the flow path length:

$$Q = K \cdot A \cdot \left(\frac{h_1 - h_2}{L}\right)$$

where K is known as hydraulic conductivity, which varies as a function of the soil and fluid characteristics.

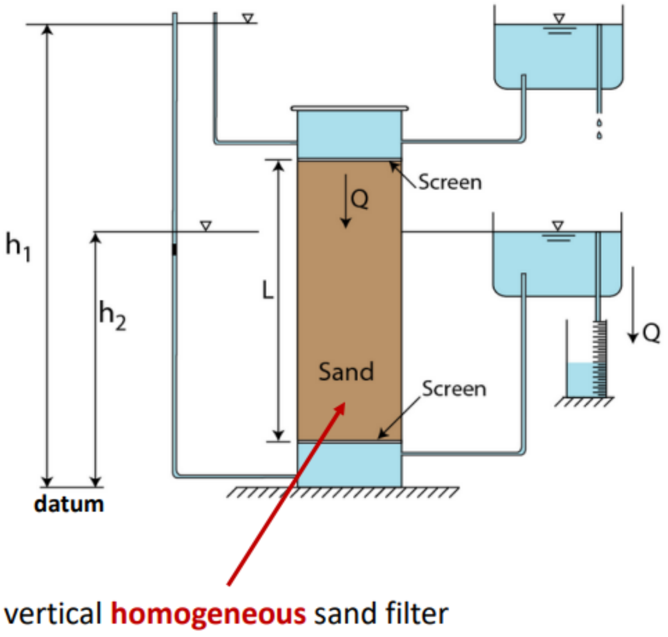

Figure 11: Schematic representation of Darcy's experimental apparatus

By defining the specific discharge (also known as Darcy's velocity) as $q = \frac{Q}{A}$ and introducing the hydraulic gradient $i = \frac{h_1 - h_2}{L}$, the equation can be rewritten as:

$$q = K \cdot i$$

The Darcy's Law was derived experimentally for one dimensional flow in a homogeneous porous medium. The generalized three-dimensional form of the equation for in-homogeneous and anisotropic media can be expressed as:

$$\boldsymbol{q} = -\,\boldsymbol{K}(x, y, z) \cdot \boldsymbol{i}$$

The negative sign in the above equations means that water flows in the direction of decreasing potential.

3.3 Unsaturated soil parameters and suction behaviour

Flow is governed not only by hydraulic conductivity but also depends on other spatially dependent characteristics. As previously stated, water and air coexist in the pore spaces of the unsaturated zone, alongside the solid soil matrix. This partitioning can be expressed volumetrically as:

$$V = V_s + V_w + V_a$$

where V is the total soil volume and V_s, V_w and V_a are the volumes of soil, water, and air, respectively.

Based on this relationship, several key parameters can be defined. Porosity, φ, represents the ratio between the volume of the voids (V_v), which is given as the sum of volume of water and air, and the total volume:

$$\varphi = \frac{V_v}{V} = \frac{V_a + V_w}{V}$$

While specific discharge (q) represents the flow rate per total cross-sectional area, it does not account for the fact that only a fraction of the area actually carries water. This is where porosity becomes important, as only φA is available for flow. Thus, the seepage velocity (v), the actual average velocity of water particles, is:

$$v = \frac{Q}{\varphi \ \mathrm{A}} = \frac{q}{\varphi}$$

Another important parameter is the water content, θ, which is the ratio between the volume of water and the total volume:

$$\theta(t) = \frac{V_w(t)}{V}$$

For unsaturated soil θ varies from 0 up to the value of the porosity φ. Going more into specifics, saturated soil moisture content (θ_s) refers to the water content when the porous medium is fully saturated, thus, by definition, it is equal to the porosity. On the other hand, residual soil moisture content (θ_r) is the water content retained in the soil once gravity drainage has stopped.

Lastly, saturation (S_w) is defined as the ration between the volume of water and the volume of voids:

$$S_w(t) = \frac{V_w(t)}{V_v}$$

For saturated soil S_w=1, while for unsaturated soil $0 < S_w < 1$.

The interdependence of the three parameters is given by:

$$\theta(t) = S_w(t)\ \varphi$$

While the determination of the above parameters is important, it is not sufficient to fully describe flow processes in unsaturated soils. To capture the driving forces of water movement, it is necessary to introduce the concept of suction (or suction head, ψ), which represents the negative (i.e. below the atmospheric value) pressure under which water is held within soil pores due to capillary forces. The hydraulic potential is usually expressed as the total head (H), defined as:

$$H = z + h$$

where h is the pressure head and z the elevation head. In unsaturated porous media, the pressure head is generally replaced by the suction head ψ, reflecting the capillary effects that dominate in the vadose zone. At the pore scale, an unsaturated medium would reveal curved water surfaces bridging from grain to grain within the pore channels, where the radius of curvature of each interface is directly related to the surface tension forces. This microscopic configuration gives rise to the macroscopic expression of suction, which governs how strongly water is held in the unsaturated soil and thus influences its availability and movement.

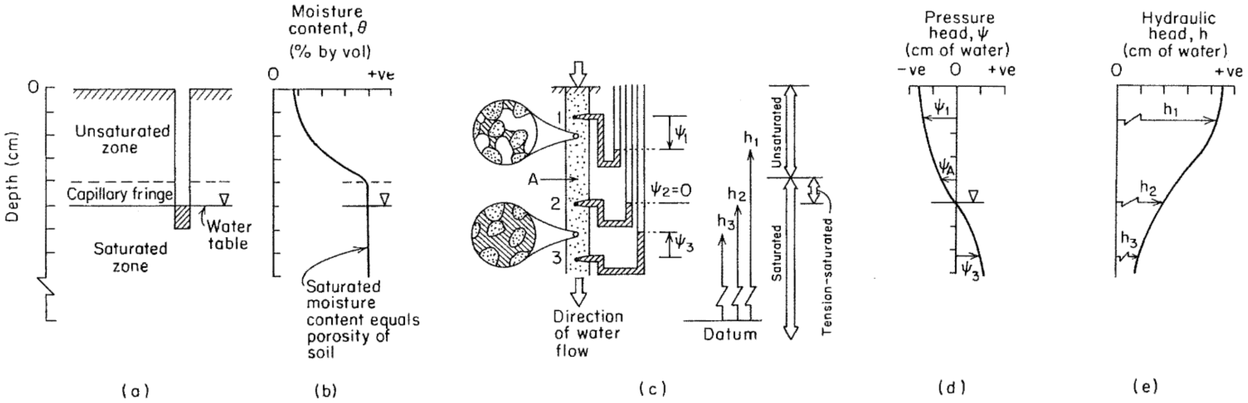

Figure 12: Groundwater conditions near the ground surface. (a) Saturated and unsaturated zones; (b) profile of moisture content versus depth; (c) pressure-head and hydraulic-head relationships; insets: water retention under pressure heads less than (top) and greater than {bottom) atmospheric; (d) profile of pressure head versus depth; (e) profile of hydraulic head versus depth (after Freeze and Cherry, 1979)

The relationship between water content and suction is described by the soil-water characteristic curve, or retention curve (Figure 13). This curve is characterised by a hysteretic behaviour, meaning that the path followed during drying differs from that during wetting. In addition, soil texture strongly influences the shape of the curve: finer soils such as clays, characterized by smaller pores and stronger soil–water interactions, develop higher suction values than sands at the same water content. Conversely, for a given suction, clays are more humid than sandy soils, reflecting their greater water-holding capacity.

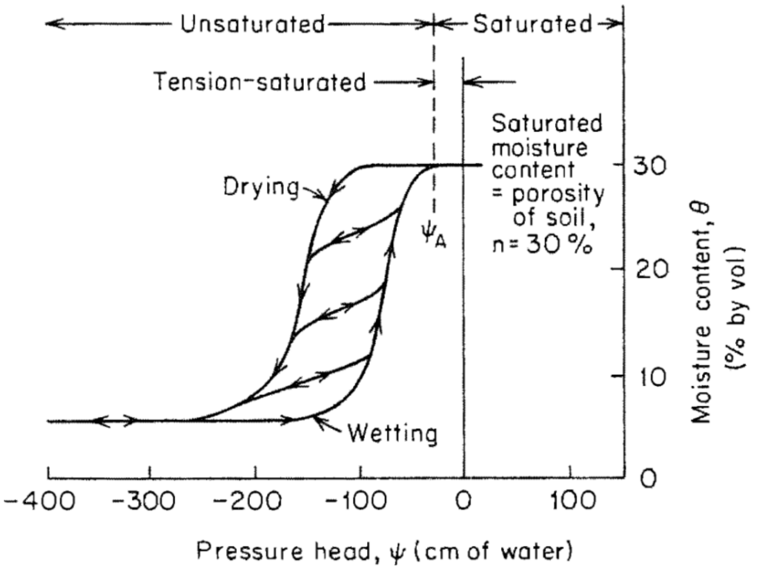

Figure 13: Characteristic curves relating moisture content to pressure head for a naturally occurring sand soil (after Liakopoulos, 1965).

Several methods have been developed to estimate soil hydraulic properties from easily measurable characteristics such as grain size distribution. These approaches are particularly appealing because obtaining grain size data is generally simpler than conducting detailed static or dynamic hydraulic measurements. Each method involves several coefficients that must be calibrated by fitting measured experimental data to analytical expressions. Among these, the van Genuchten model (1980) is one of the most widely used, relating volumetric water content θ to matric suction ψ through the expression:

$$\frac{\theta - \theta_r}{\theta_s - \theta_r} = (1 - (\alpha\psi)^n)^{-1+\frac{1}{n}}$$

where $\alpha = \frac{1}{\psi_a}$ is the inverse of the air entry pressure and n is an empirical measure of the pore-size distribution.

3.4 The continuity equation and Richards equation

Beside Darcy's law, another relation is necessary to describe how water flows in a variably saturated porous medium. This relation is the continuity equation that expresses the fundamental principle of mass conservation, stating that in a representative elementary volume (REV, Figure 14) having edges of length Δx, Δy, Δz the net result of inflow I minus outflow O is balanced by the change in water mass M stored or released in a given period of time.

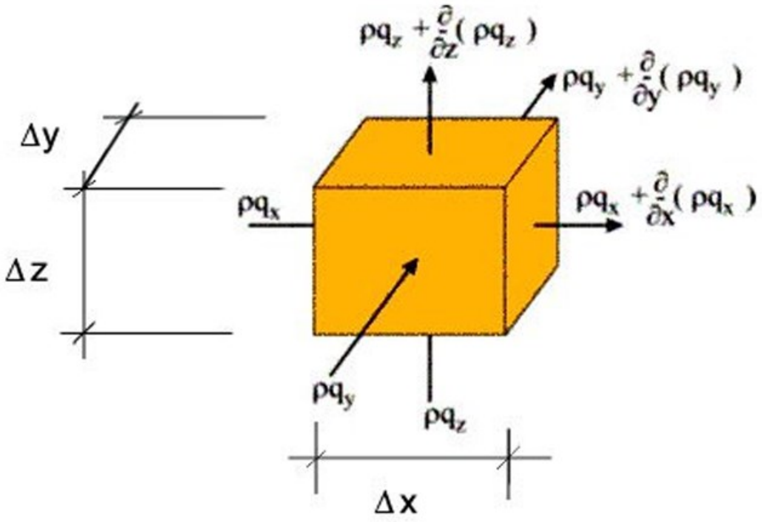

Figure 14: Representative elementary volume for flow through porous media.

This relationship can be expressed mathematically as:

$$I - O = \frac{\delta M}{\delta t}$$

The mass inflow I_x during the interval Δt through the left face of area $\Delta y \Delta z$ is:

$$I_x = \rho \; V_x = \rho \; q_x \; \Delta t \; \Delta y \; \Delta z$$

Using the Taylor series expansion along x-axis and keeping only the first two terms, the outflow O_x in the same interval Δt is:

$$O_x = \rho \; V_{x+\Delta t} = \left[\rho \; q_x + \frac{\delta(\rho \; q_x)}{\delta x} \Delta x\right] \Delta t \; \Delta y \; \Delta z$$

Considering also the other two directions, the balance of the total mass inflow and the total mass outflow can be written as:

$$I - O = \left[\frac{\delta(\rho\, q_x)}{\delta x} + \frac{\delta(\rho\, q_y)}{\delta y} + \frac{\delta(\rho\, q_z)}{\delta z}\right] \Delta x\, \Delta y\, \Delta z\, \Delta t = -div(\rho\, q)\, \Delta x\, \Delta y\, \Delta z\, \Delta t$$

As for the right side of the continuity equation, the mass of groundwater *M(t)* existing in the REV at the moment *t* is:

$$M(t) = \rho \cdot \theta \cdot V = \rho \cdot \theta \cdot \Delta \mathrm{x} \cdot \Delta \mathrm{y} \cdot \Delta \mathrm{z}$$

and the mass *M(t + Δt)* can be approximated using the first two terms of the Taylor series expansions as:

$$M(t + \Delta t) = M(t) + \frac{\delta M}{\delta t}\Delta t = M(t) + \frac{\delta(\rho\, \theta\, \Delta \mathrm{x}\, \Delta \mathrm{y}\, \Delta \mathrm{z}\ )}{\delta t}\Delta t$$

It follows that:

$$\delta M = M(t + \Delta t) - M(t) = \frac{\delta(\rho\, \theta\, \Delta \mathrm{x}\, \Delta \mathrm{y}\, \Delta \mathrm{z}\ )}{\delta t}\Delta t$$

The water density and the volumetric water content are functions of the spatial variables and of time: $\rho = \rho\ (x, y, z, t)$ and $\theta = \theta\ (x, y, z, t)$. The water density as well as the control volume varies in time due to the water pressure variation. Still, the deformations of the control volume are neglected. As a result, the derivative in the previous relation can be expressed as:

$$\frac{\delta(\rho\, \theta\, \Delta \mathrm{x}\, \Delta \mathrm{y}\, \Delta \mathrm{z}\ )}{\delta t} = \frac{\delta \rho}{\delta t}\theta\, \Delta \mathrm{x}\, \Delta \mathrm{y}\, \Delta \mathrm{z} + \rho \frac{\delta \theta}{\delta t}\Delta \mathrm{x}\, \Delta \mathrm{y}\, \Delta \mathrm{z} = \rho \left(\frac{\theta}{\rho}\frac{\delta \rho}{\delta t} + \frac{\delta \theta}{\delta t}\right) \Delta \mathrm{x}\, \Delta \mathrm{y}\, \Delta \mathrm{z}$$

The continuity equation is obtained by equalizing the total net inflow mass to the change in mass into the REV:

$$-div(\rho\, q)\, \Delta x\, \Delta y\, \Delta z\, \Delta t = \rho \left(\frac{\theta}{\rho}\frac{\delta \rho}{\delta t} + \frac{\delta \theta}{\delta t}\right) \Delta \mathrm{x}\, \Delta \mathrm{y}\, \Delta \mathrm{z}\, \Delta t$$

Dividing by Δx Δy Δz Δt, considering that in the case of unsaturated media the variation of the water mass density can be neglected and that the water mass density can be considered constant, the continuity equation becomes:

$$-div(q) = \left(\frac{\delta\theta}{\delta t}\right)$$

By introducing the Darcy's law into q, the general soil water transfer equation can be obtained:

$$div[K(\theta)gradH] = \left(\frac{\delta\theta}{\delta t}\right)$$

where H represents the total soil moisture potential: $H = \psi + z$, ψ is the matric potential in units of length and z the elevation above the reference plan.

In order to obtain the general equation expressed only as a function of ψ, $K(\theta)$ will be replaced by $K(\psi)$ and taking into account that $\theta = \theta(\psi) == \theta(\psi(x,y,z,t))$, the right side of the equation will be rewritten as:

$$\left(\frac{\delta\theta}{\delta t}\right) = \frac{\delta\theta}{\delta\psi}\,\frac{\delta\psi}{\delta t}$$

Substituting, the general equation becomes:

$$div[K(\psi)gradH] = \frac{\delta\theta}{\delta\psi}\,\frac{\delta\psi}{\delta t}$$

where the ratio $C(\psi) = \frac{\delta\theta}{\delta\psi}$ is defined as specific moisture capacity and represents the derivative of the characteristic curve. The final equation can be rewritten as follows:

$$div[K(\psi)grad(\psi - z)] = C(\psi)\,\frac{\delta\psi}{\delta t}$$

The above equation is known as Richards' equation, in honour of the soil physicist who first developed it in 1931.

3.5 The Finite Element Method and the GroundWater Simulator

To solve the Richards equation for variably saturated flow, the Finite Element Method (FEM) was adopted. The Richards equation is a partial differential equation that requires numerical methods to provide solutions. Among the different discretization techniques available, the Finite Element Method is particularly well suited for solving groundwater flow problems. FEM is based on subdividing the spatial domain into smaller, simple elements (triangles, quadrilaterals, tetrahedra, etc.), over which the governing equation is approximated. This approach allows great flexibility in representing complex geometries, heterogeneous soil properties, and varying boundary conditions.

For the present work, simulations were carried out using the GroundWater Simulator (GWS), a software developed at the Department of Mathematical Methods and Models for Scientific Applications of the University of Padua (Paniconi et al., 1994). Currently implemented in Fortran90, GWS has been further developed and updated by M3E Srl. The software uses the FEM to solve coupled flow and transport equations, and uses the Galerkin formulation to approximate the underlying partial differential equations. To perform simulations, the software requires a discretized domain represented by a mesh of tetrahedral elements, together with a set of input files that define the initial conditions and the boundary conditions of Dirichlet, Neumann, and Seepage Face type.

4. Materials

The modelling activities began with the analysis of the groundwater dynamics in simplified and smaller-case tests. This step is aimed at becoming familiar with the modelling tools and procedures. These preliminary simulations also served to provide an initial understanding of the model's sensitivity and dynamic responses under controlled conditions. Following these initial trials, the study focused on a real case: a portion of the artificial Amira salt marsh. This site was selected for its relevance to current restoration practices and availability of elevation and hydrological data.

For both the simplified and real-case simulations, a consistent workflow was followed. First, the mesh was generated using Gmsh, allowing for precise control of spatial discretization and surfaces definition. Subsequently, Python scripts were employed to define and apply boundary conditions, define tidal fluctuations, and adjust model input parameters. These scripts ensured flexibility and reproducibility throughout the modelling process. In the case of the Amira salt marsh, additional data preprocessing was required. Topographical elevation data of the marsh surface were extracted from a Digital Surface Model (DSM) and further processed using Surfer software. Finally, groundwater simulations were conducted using the GroundWater Simulator (GWS), and results were visualized in Visit.

4.1 Mesh generation

In this work, all simulations were carried out using meshes generated with Gmsh, an open-source 3D finite element mesh generator. Gmsh is structured around four core modules (geometry, mesh, solver, and post-processing) which can be accessed through its graphical interface, command-line tools, scripting through its native .geo file format, or through the C++, C, Python, Julia and Fortran application programming interface. The generated meshes primarily consisted of tetrahedral elements, with refined resolution applied in the upper layers and close to the channel region. This adaptive meshing strategy ensured a good compromise between computational efficiency and solution accuracy, particularly in areas where greater detail was necessary for capturing hydrodynamic behaviour.

For the initial phase of testing, a simple parallelepiped flat marsh with dimensions 5 m × 10 m × 2.5 m was discretized as a baseline (case S0) to validate the mesh generation process and the simulation workflow (Figure 15). The marsh elevation was fixed at +0.5 m above msl.

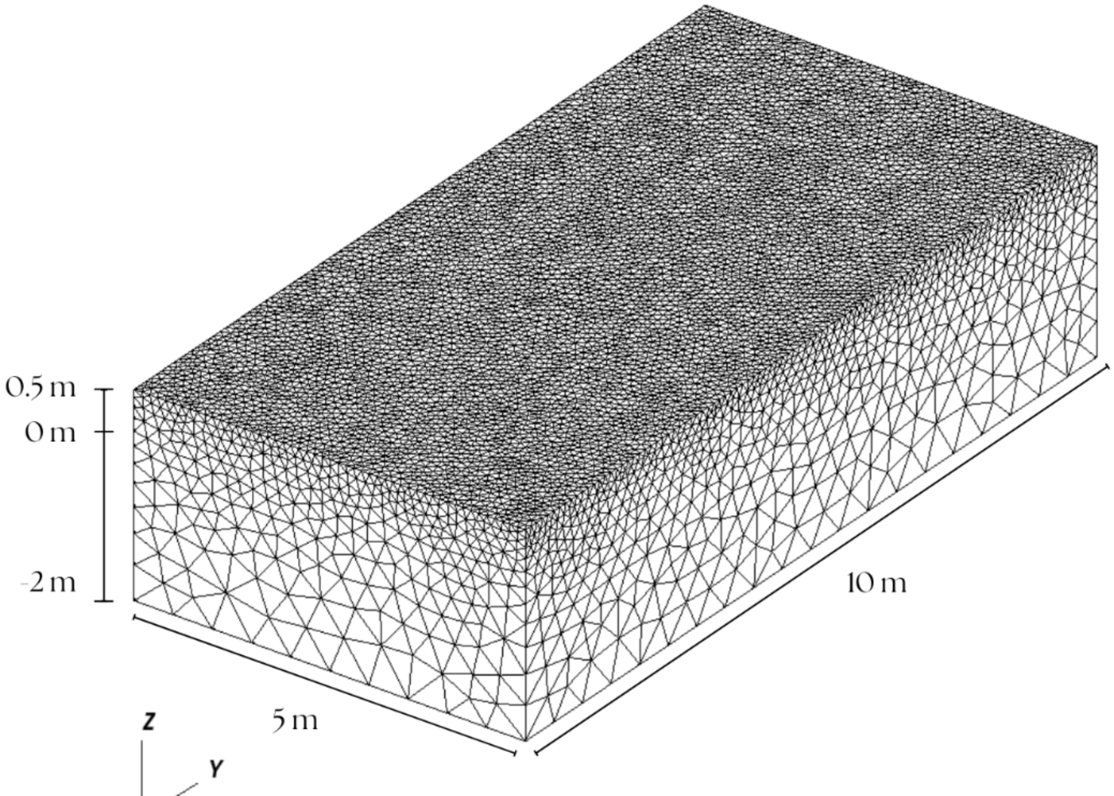

Figure 15: Mesh with flat platform (case S0).

In addition to the basic configuration, the analysis was extended to include two more configurations: the first representing a salt marsh with a straight channel of rectangular cross-section 8 m long, 0.7 m wide, and 0.35 m deep (case S1); and the second featuring a more realistic meandering channel geometry (Figure 16 and Figure 17, respectively) (case S2). This latter setup was designed to more accurately reproduce the natural morphology of tidal creeks typically found in lagoon environments. In the complex configuration, the channel depth also varied along its course, with shallower sections towards the inner parts of the salt marsh. While the straight-channel configuration enabled a controlled analysis of flow dynamics in simplified conditions, the more realistic case was designed to investigate how tidal flows interact with complex, naturally occurring topographic features, offering a closer representation of actual lagoon conditions.

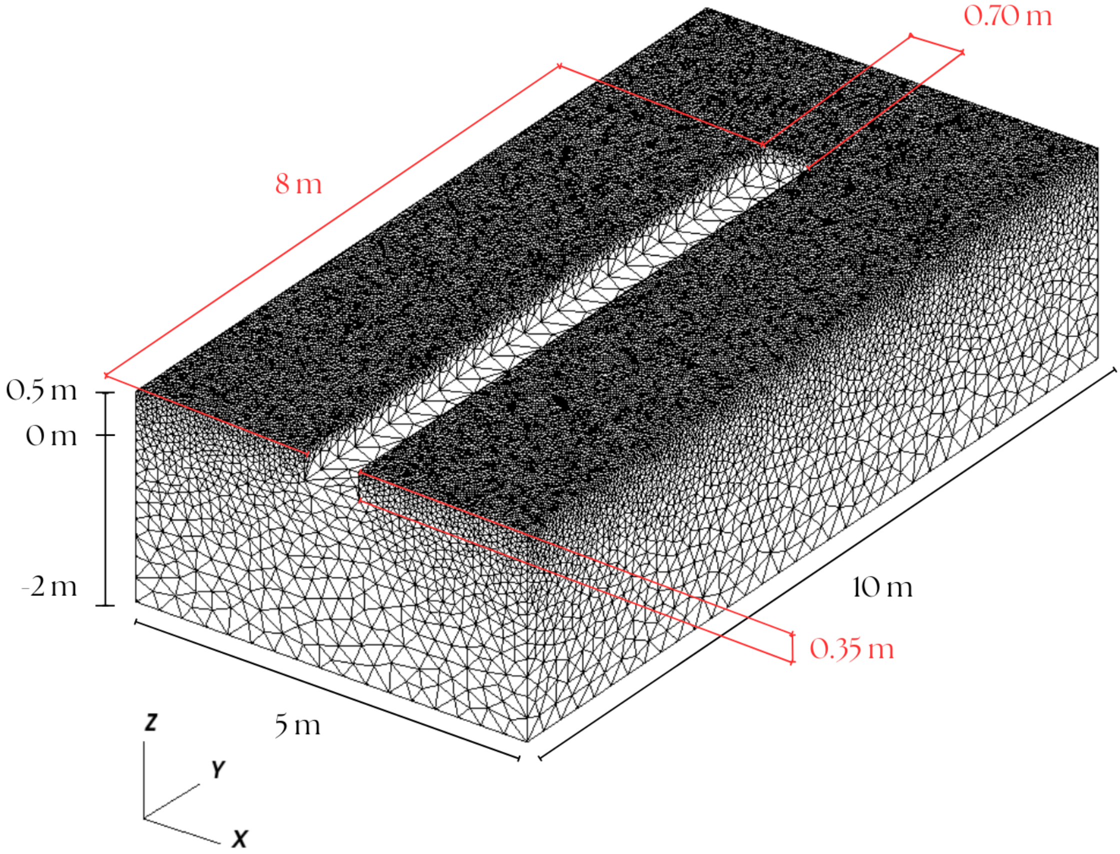

Figure 16: Mesh with straight channel crossing the platform (case S1).

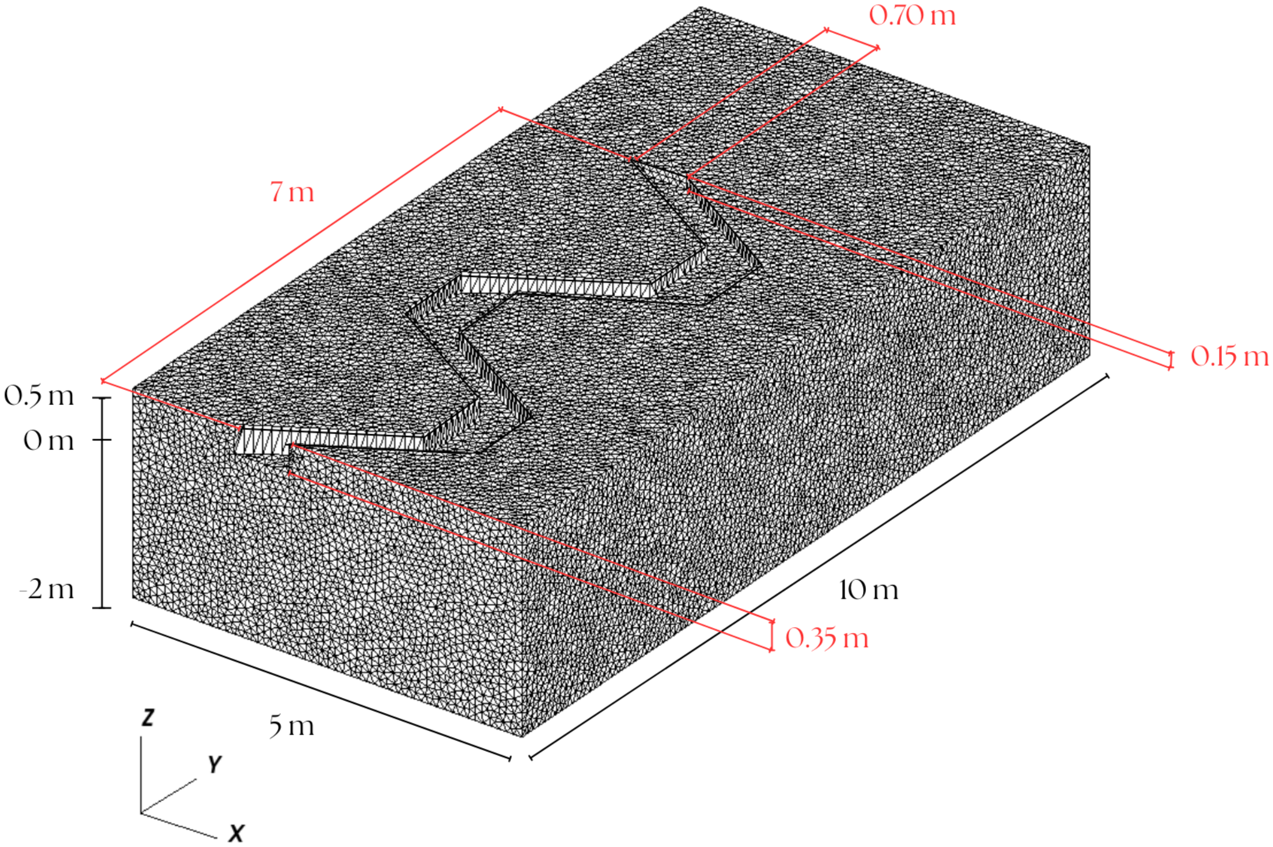

Figure 17: Mesh with a meandering channel (case S2).

For the Amira artificial salt marsh, a representative portion of the landform was selected on the south-west side, where a channel system had developed (Figure 18). This section underwent a series of interventions that facilitated the formation of a drainage network. The initial intervention involved removing the containment structures in part of the marsh, allowing a channel to form naturally. Subsequent work focused on excavating and deepening the channel, extending it further into the marsh to enhance drainage and water circulation.

Initially, a mesh with a flat top surface was created for preliminary testing (Figure 19). Subsequently, the mesh top surface was modified to reflect actual elevation values across the entire domain, using data extracted from a DSM dated 24/02/2025 based on a Lidar acquisition. The integration of the DSM data onto the mesh surface was carried out using a combination of Python scripts and Surfer software, which enabled the adaptation of the surface geometry.

Figure 18: Portion of the Amira salt marsh (in yellow) addressed by the simulations.

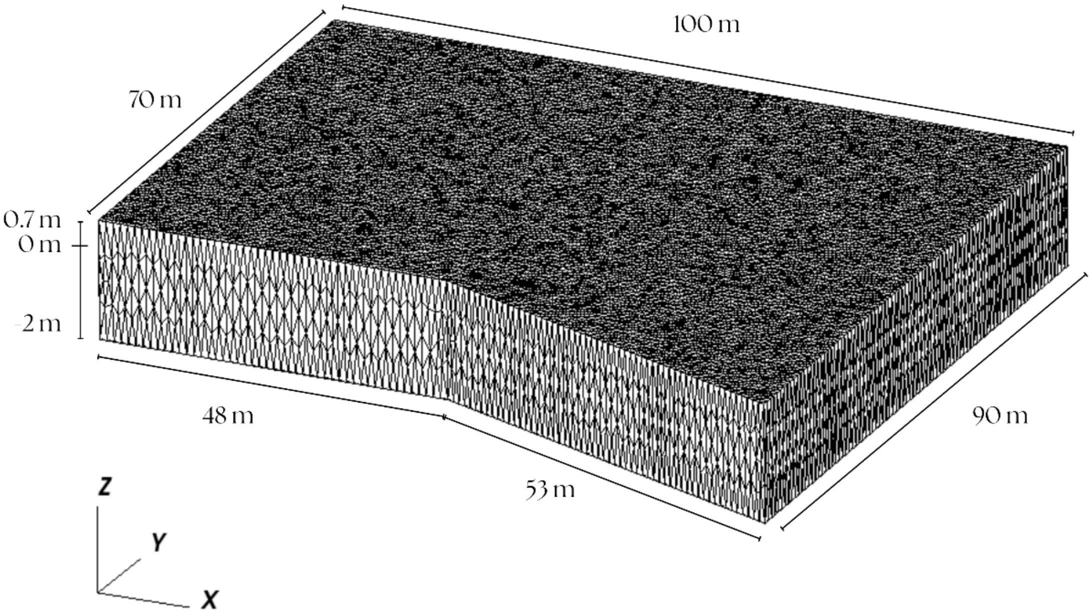

Figure 19: Intitial mesh of the Amira salt marsh with flat top surface used for initial testing (case A0).

The DSM used in this study provided elevation data with a spatial resolution of 2 cm, offering detailed information on surface topography. This level of precision enabled an accurate reconstruction of the upper surface morphology within the model domain, which is essential for simulating hydrological processes influenced by small-scale elevation variability. To integrate this topographic data into the mesh, Surfer, a powerful contouring, gridding, and surface mapping software developed by Golden Software, was employed. Through its gridding and residuals calculation features, Surfer enabled the transition from top nodes that initially shared a uniform average height to a more realistic top-surface elevation profile derived from the actual DSM. Subsequently, a Python script was employed to update the elevation of all mesh nodes. The process began by replacing the initial average elevations of the top surface nodes with the actual values obtained from Surfer. Beyond substituting the top node elevations, it was also necessary to adjust the elevations of all underlying nodes so that their positions remained consistent with the updated surface. The final elevation of the underlying nodes was calculated as:

$$z_{final} = z_{initial} + \Delta z \cdot a$$

where $z_{initial}$ is the initial elevation of the underlying node, Δz represents the elevation change of the closest surface node relative to its initial average elevation, and $a = \frac{h_0}{S_0}$, with h_0 defined as the vertical distance between the node and the bottom of the mesh and S_0 as the initial mesh thickness (Figure 20).

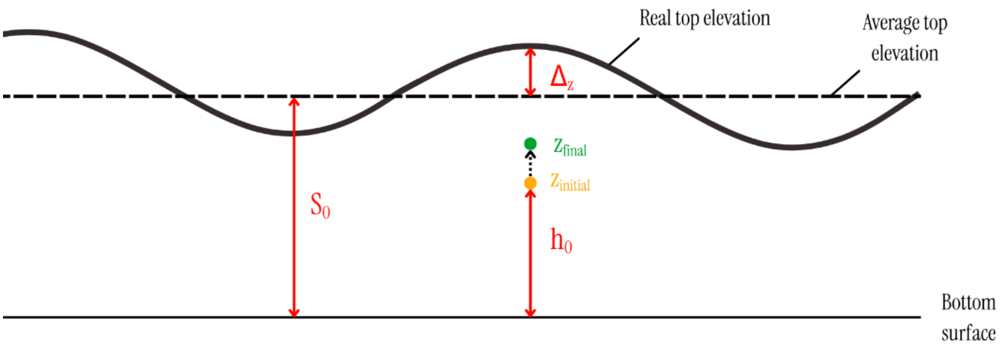

Figure 20: Schematic representation of the parameters used to adjust the elevation of underlying nodes.

Also in this case, three different model configurations were developed to assess the influence of surface morphology on system behaviour:

- The first configuration (case A1) consisted of a mesh incorporating the adapted elevation values (Figure 22). Later, to allow greater control over the simulations, channels were introduced manually.
- The second mesh (case A2) included a single main channel (Figure 23);
- The third mesh (case A3) incorporates a more realistic network of channels (Figure 24), based on the topographic details provided by the DSM. The depth of the channels was also varied and made shallower in the inner parts of the salt marsh to better reflect natural conditions. These channels depth variations were derived directly from the DSM data, as illustrated in Figure 21.

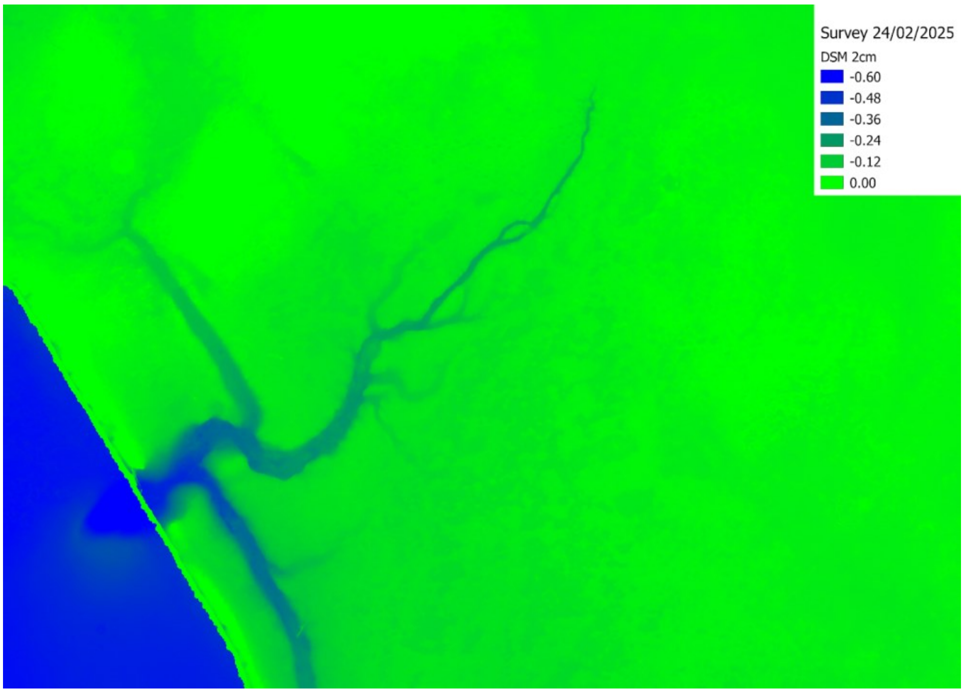

Figure 21: Channel distribution and depth as obtained from the DSM of 24/02/2025.

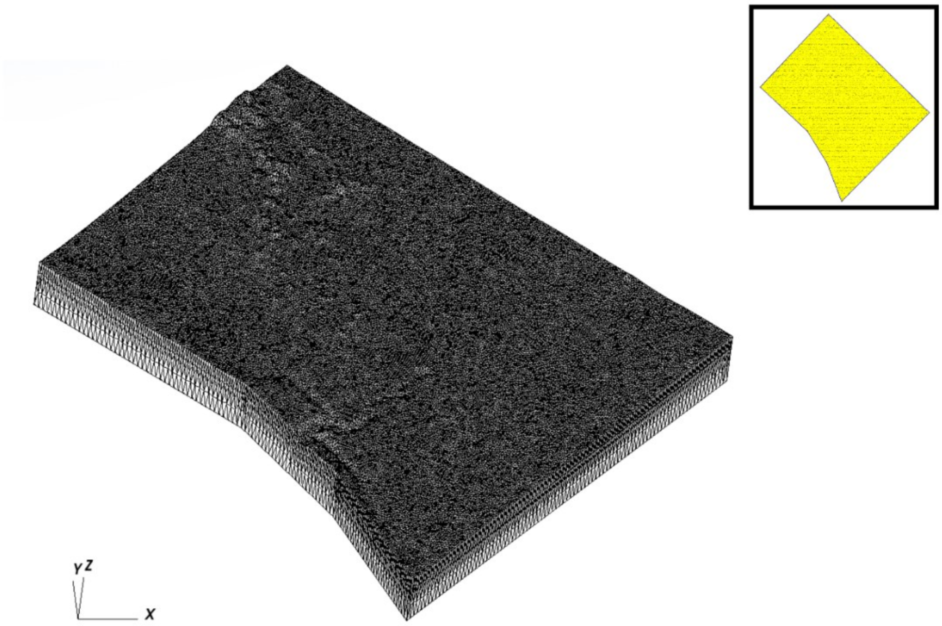

Figure 22: Mesh with adapted elevation profile based on the DSM of 24/02/2025. Vertical exaggeration factor is equal to 6. A top visualization of the mesh is provided in the upper-right section (case A1).

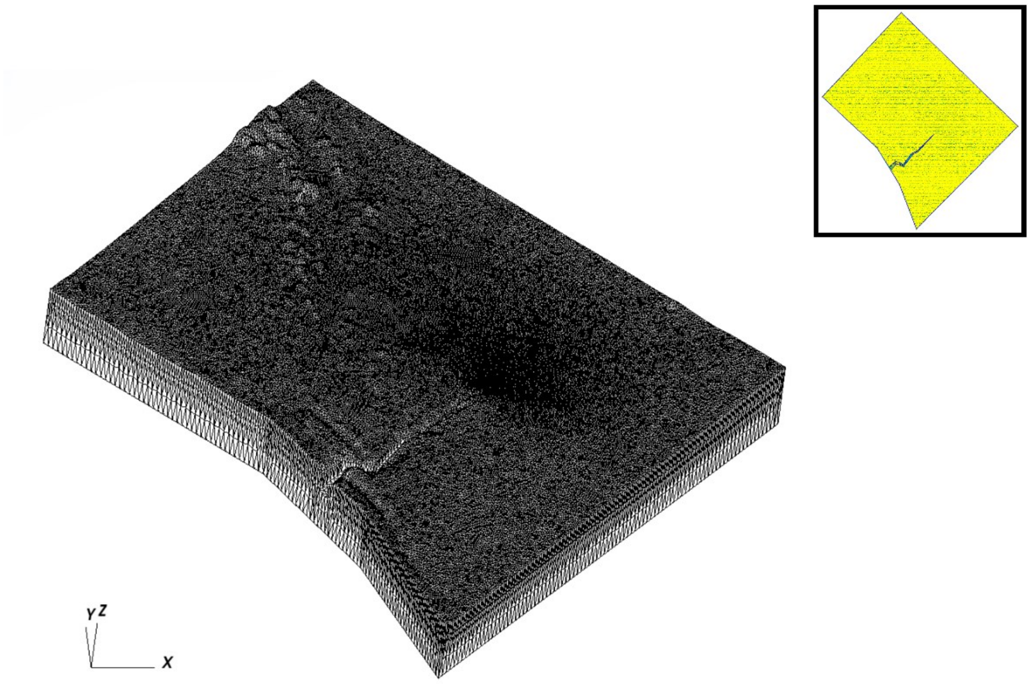

Figure 23: Mesh with adapted elevation profile based on the DSM of 24/02/2025, including a single tidal channel. Vertical exaggeration factor is equal to 6. A top visualization of the mesh is provided in the upper-right section (case A2).

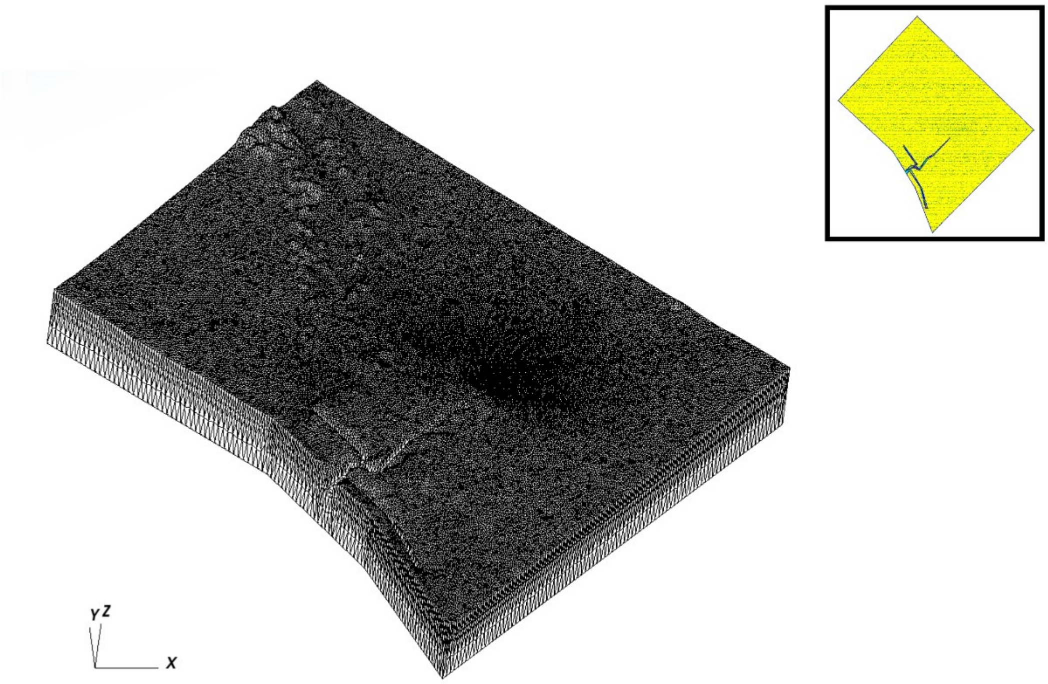

Figure 24: Mesh with adapted elevation profile based on the DSM of 24/02/2025, including a three-channel network. Vertical exaggeration factor is equal to 6. A top visualization of the mesh is provided in the upper-right section (case A3).

4.2 Input files

To run the simulations using the GroundWater Simulator, a series of input files needed to be generated. Hydrogeologic parameters were specified. Initial and boundary conditions were established defining Dirichlet, Neumann, and seepage face conditions depending on the physical characteristics of the domain. Topological information and the total number of nodes were extracted directly from the generated mesh. All data preparation and formatting were handled using custom Python scripts, enabling efficient automation and integration into the simulation workflow.

4.2.1 Soil properties

In order to reduce complexity and enhance computational efficiency, the model assumed a single, homogeneous soil type uniformly distributed across the entire computational mesh. Soil properties were kept constant throughout all the simulations, with the exception of the case of hydraulic conductivity variation explored in detail in Chapter 5.5.3. The hydraulic conductivity value and the van Genuchten model parameters used are summarized in Table 1.

Table 1: Soil parameters used in the simulations

$\boldsymbol{K}$ **(m/s)**	$\boldsymbol{\alpha}$ **(m^{-1})**	$\boldsymbol{n}$	$\boldsymbol{\theta_r}$	$\boldsymbol{\varphi}$
$7 \cdot 10^{-4}$	7.5	1.89	0.1	0.45

4.2.2 Initial conditions

Initial conditions were defined in terms of pressure head, assuming a hydrostatic distribution representative of a system in equilibrium. As illustrated in Figure 25 the pressure field was initialized by setting the water level in the main channels bounding the salt marsh to correspond with mean sea level (0.0 m above MSL). Under this assumption, a positive hydrostatic pressure was applied to all nodes located below the water table, representing saturated conditions, while a negative pressure head was assigned to nodes above the water table, accounting for unsaturated conditions within the vadose zone.

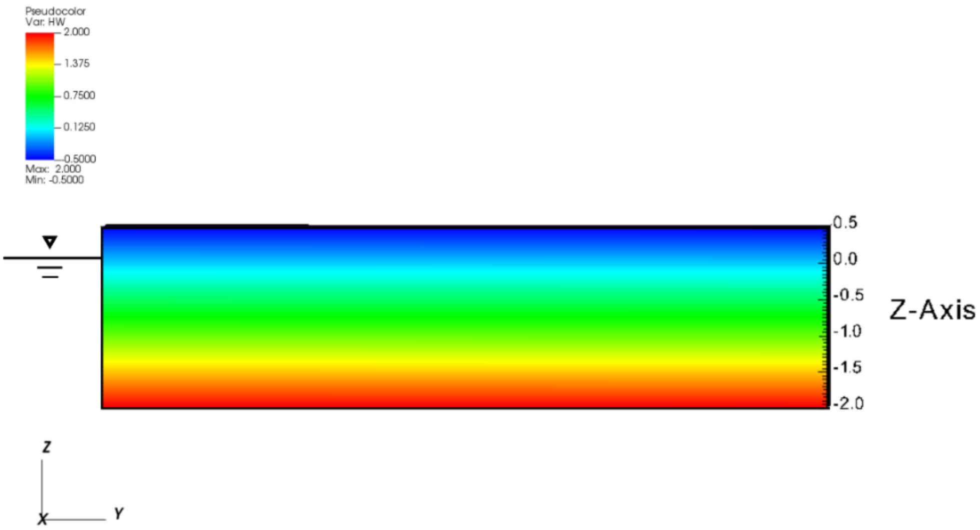

Figure 25: Initial pressure head distribution for the simplified and Amira mesh configuration.

4.2.3 Boundary conditions

Boundary conditions in the model were assigned according to well-defined physical and hydrological criteria, aiming to realistically represent the system behaviour under varying tidal and flow conditions. To better understand the variability of results, different boundary configurations were applied (Figure 26).

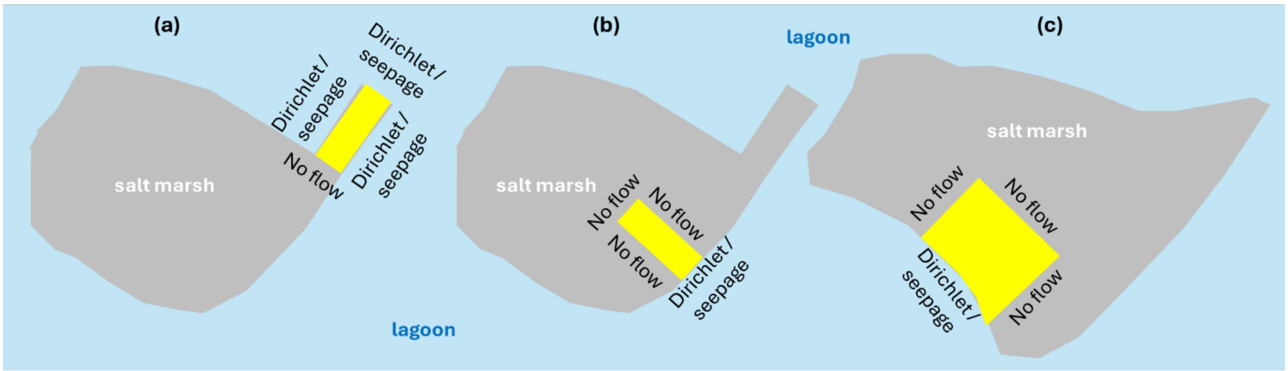

Figure 26 : Sketch representing the boundary conditions applied over the lateral surfaces of the simulated salt marsh for the three selected configurations: (a) first simple test; (b) second simple test; and (c) Amira

For the initial simplified tests, the boundary conditions were defined as follows:

- Front and lateral surfaces: dynamic seepage face boundary condition is applied to the portion of the boundary above the tidal level, representing the drainage condition at atmospheric pressure. Below the water table time-variable Dirichlet conditions are applied, with the pressure head calculated based on the difference between the tidal level and the local elevation (Figure 26a).
- Top surface: when the tidal level exceeds the marsh elevation and the surface is completely flooded, the surface is characterised by a Dirichlet boundary condition. When the water level is below the ground surface, a no-flux boundary condition is applied to the surface, represented by a Neumann boundary condition.

- Bottom and back surfaces: no-flux boundary conditions are applied in both cases due to the presence of low-permeable soil and the symmetry condition, respectively (Figure 26a).

With the introduction of a channel into the model domain, boundary conditions were established to reflect the new geometry. The original boundary conditions on all other surfaces remained unchanged, while the channel was treated as follows:

- Channel lateral surfaces: dynamic seepage face boundary condition is applied to the portion of the bank above the tidal level, representing the drainage condition at atmospheric pressure. Below the water table, a hydrostatic pressure distribution is assigned, according to a Dirichlet boundary condition.
- Bottom of the channel: no flux boundary conditions are applied

To further assess the impact of lateral boundary assumptions, additional one-side flow simulations were carried out by modifying the original setup. In these scenarios, the time-variable Dirichlet conditions on the lateral boundaries were replaced with no-flux (Neumann) conditions. The front surface, however, maintained the same boundary conditions as in the original configuration, with a dynamic seepage face above the tidal level and time-variable Dirichlet conditions below (Figure 26b). This allowed for the evaluation of model sensitivity to lateral flow and its influence on internal flow dynamics. In relation to these two settings of the boundary conditions, in the following the case with tidal fluctuation applied on the front and two lateral boundaries are denoted by 'a', whereas if the front boundary is considered only the case is denoted by 'b', respectively, e.g., case S0a and case S0b.

For the real-case simulations, boundary conditions were established to match the actual conditions observed in the field as much as possible:

- Front surface: dynamic seepage face boundary condition is applied to the portion of the boundary above the tidal level, representing the drainage condition at atmospheric pressure. Below the water table time variable Dirichlet conditions are applied, with the pressure head calculated based on the difference between the tidal level and the local elevation (Figure 26c).
- Top surface: when the tidal level exceeds the marsh elevation and the surface is completely flooded, the surface is characterised by a Dirichlet boundary condition. Differently from the previous simulations, when the water level is below the ground surface, a dynamic seepage face boundary condition is applied to the portion of the boundary above the tidal level.
- Bottom, lateral and back surfaces: no-flux boundary conditions are applied in these cases due to the presence of low-permeable soil, parallel direction with respect to the main groundwater flow direction, and the symmetry condition relative to groundwater flow, respectively (Figure 26c).

Similar to the previous tests, with the introduction of a channel into the model domain, the channel lateral surfaces were assigned a combination of dynamic seepage face conditions above the tidal level and Dirichlet boundary conditions below it. Additionally, in this configuration, the bottom of the channel was treated in the same manner as the lateral surfaces, reflecting a consistent approach to boundary condition assignment along the channel boundaries.

4.2.4 Tide fluctuations

For the simplified tests, simulations were carried out using both a standard sinusoidal tide and a real tidal record from March 2010, based on data provided by the Municipality of Venice.

The simulations started with a standard sinusoidal tide (Figure 27), assuming a tidal excursion with an amplitude of 1 m and a period of 12 hours. The simulations period lasts for 72 hours, which corresponds to 4320 minutes. This duration allows the system to stabilize and accurately reflect typical tidal behaviour, covering six full tidal cycles. The tidal variation is modelled using a simple harmonic function:

$$h(t) = H \sin(\omega t + \varphi)$$

where $h(t)$ represents the height of the tide at a given time, H is the wave amplitude, ω is the angular frequency (given by $\omega = 2\pi/T$, where T=720 minutes is the period of the tide), and φ is the phase shift.

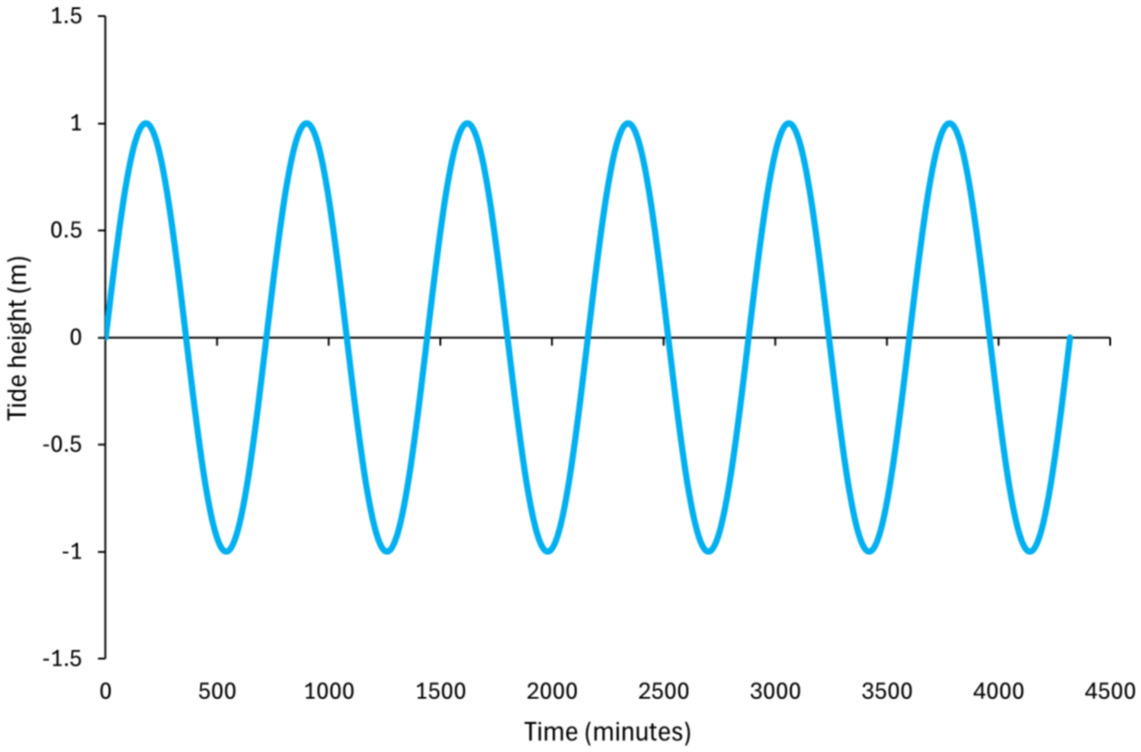

Figure 27: Standard sinusoidal tide of six full tidal cycles

In this first case a perfect sinusoidal oscillation was assumed. However, the tide recorded in a certain place is always given by the sum of two factors: an astronomical and meteorological component. The astronomical tide is described as the daily oscillation of marine water masses under the influence of the gravitational strength of the system Earth-Moon-Sun. The tide is influenced differently during the month and according to the lunar phases: during the full moon or new moon phase the highest tidal ranges are observed, while for the first and last quarter of the lunar month the tide has a lower range. Tide levels are also influenced by meteorological factors, which are primarily variations in the atmospheric pressure and the wind (like Sirocco coming from the SE and Bora coming from NNE). The atmospheric pressure is given by the strength performed by air masses on the Earth surface. Specifically, low pressure values are matched by higher values in the sea levels. The effect of the wind is more complex and depends on its strength, direction and duration, as well as on the shape and reach of the basin on which it blows. The sum of these two physical phenomena is called “overise” and leads to positive or negative increases as compared with normal astronomical oscillations (ISPRA, 2012). To capture a more realistic tidal pattern, a one-month record of observed tide data over March 2010 was selected for the simulation (Figure 28).

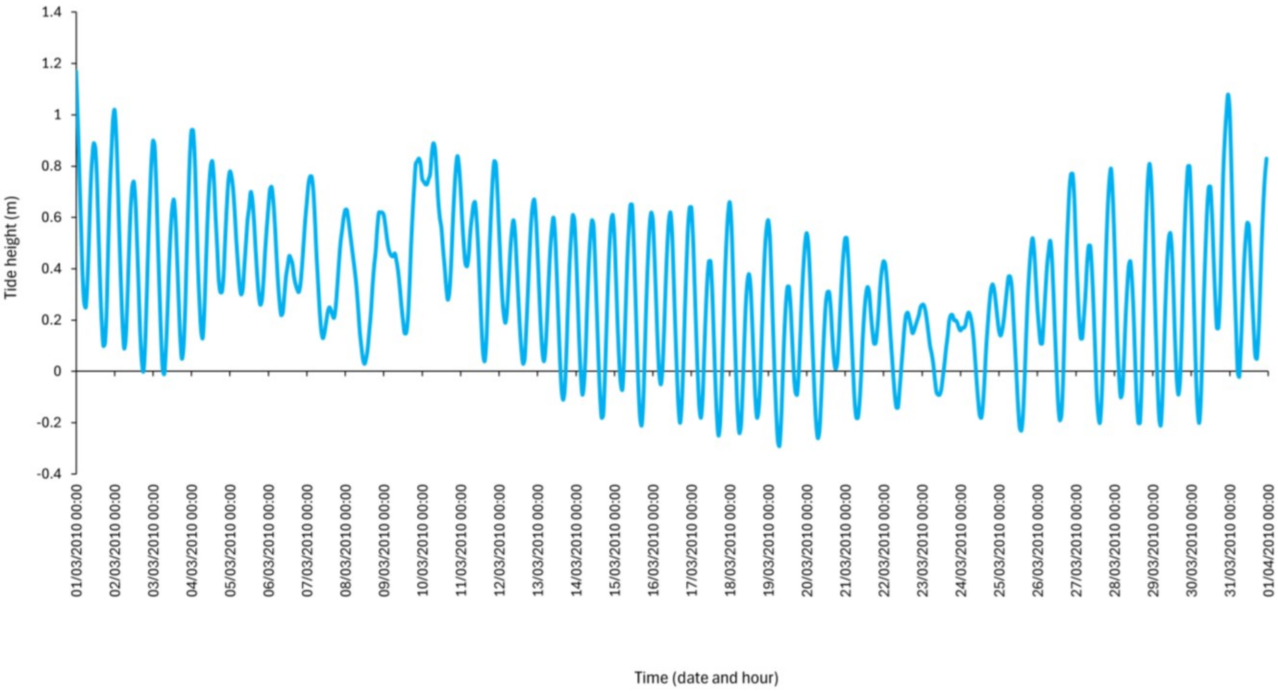

Figure 28: Real tidal record over March 2010 (Comune di Venezia, 2024).

For the Amira simulations, both a standardized sinusoidal tide and a real tidal regime were implemented. The sinusoidal tide was the same as previously described, while the real tidal input was based on data collected from tide gauge installed directly at the marsh side. Two 72-hour simulations were carried out: one using tidal data representative of summer conditions (from 15th to 17th of July 2023), and the other using data from the autumn period (from 12th to 14th of November 2023). The periods were selected with particular attention to capturing representative extremes, with a characteristically low tide for the summer period and the highest tide of the entire dataset for the autumn period. The corresponding tidal fluctuations are shown in Figure 29 and Figure 30.

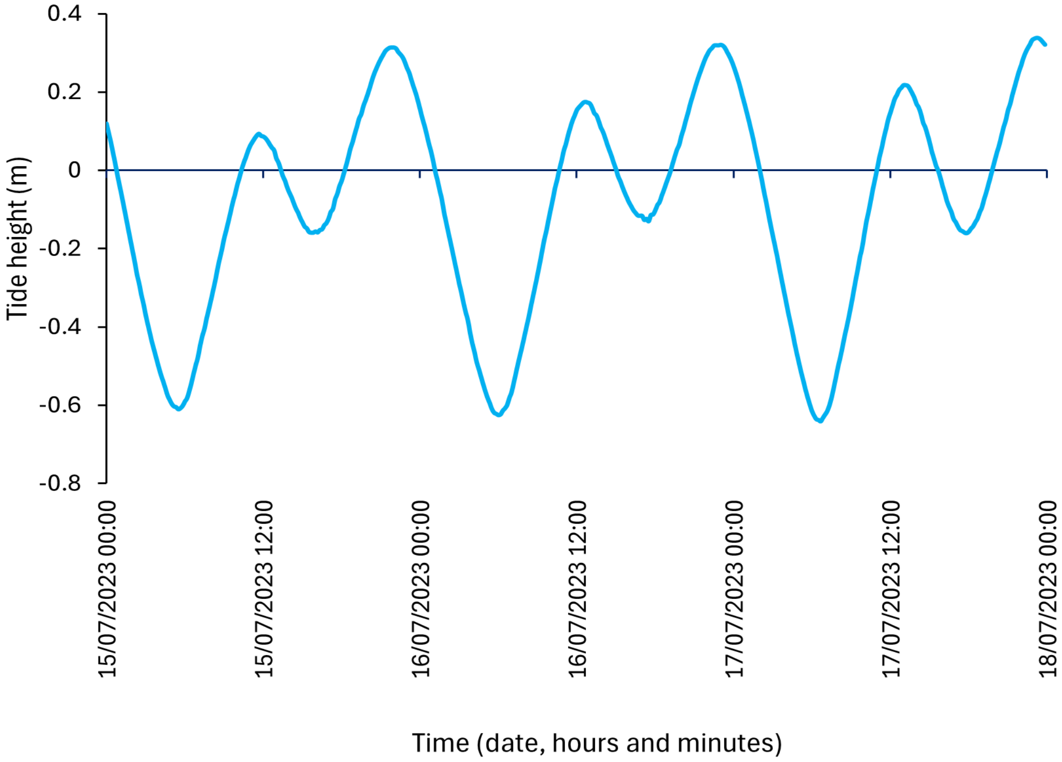

Figure 29: Real summer tide from 15/07/2023 to 17/07/2023 in front of the Amira salt marsh

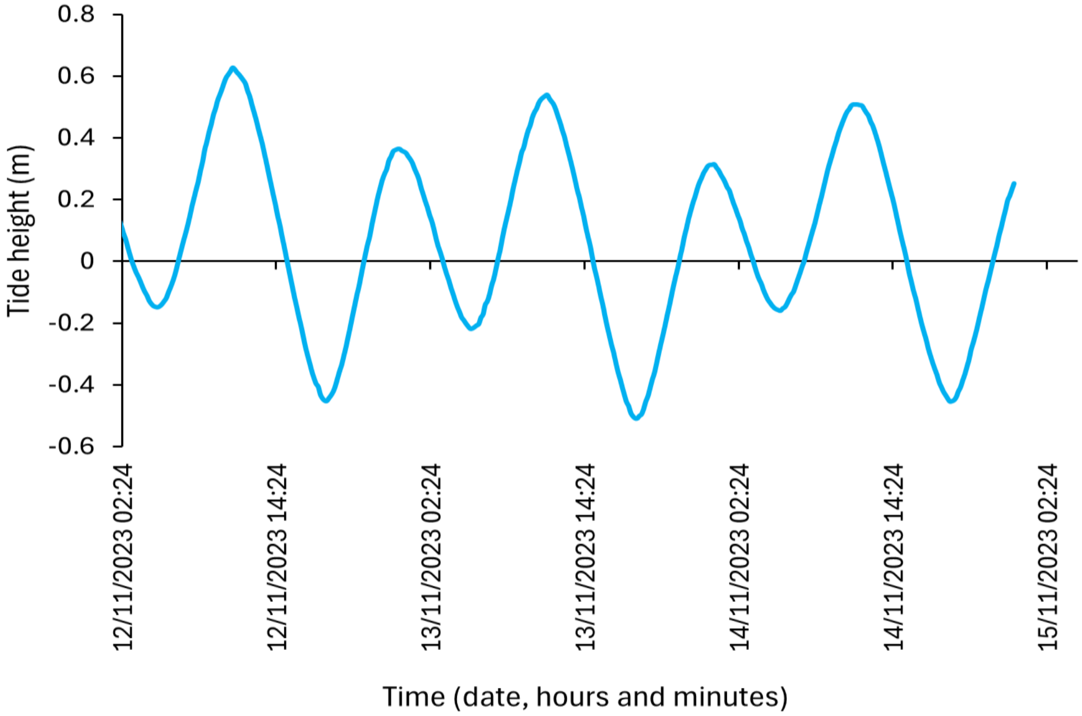

Figure 30: Real autumn tide from 12/11/2023 to 14/11/2023 in front of the Amira salt marsh

4.3 Data visualization

All simulation results from the GroundWater Simulator were visualized using VisIt (https://visit-dav.github.io/visit-website/), an open-source software distributed under Lawrence Livermore National Laboratory (LLNL), for interactive analysis and visualization of data defined on two- and three-dimensional meshes. In particular, VisIt was used to explore the spatial and temporal evolution of key variables such as pressure head and saturation. Slicing tools allowed for the inspection of system behaviour in different parts of the mesh, helping to identify spatial variations, especially near the channel. Time queries were also used to extract information at specific nodes, allowing the observation of how the presence of the channel influenced the parameters over time.

5. Results and discussion

The outcomes of the numerical simulations conducted using the GroundWater Simulator were analysed and visualized through VisIt. The primary focus of the simulations was to explore the spatial and time evolution of water saturation and pressure head under various salt marsh settings, with the goal of understanding how the presence of tidal channel promotes a more effective water drainage, thus creating conditions more suitable for the development of vegetation.

The initial set of simulations was carried out on the simplified domain representing a marsh with a flat platform (case S0). This baseline scenario points out the water saturation dynamics driven solely by drainage along the marsh boundaries, thus resembling an artificial marshland just realized. Then, the model was adapted to incorporate channels into the domain (case S1 and case S2). These modified configurations allowed for a comparative evaluation of how the introduction of tidal channels influences the drainage efficiency and drainage of the marsh, particularly in the inner regions. The simulations were run with the various boundary conditions presented above, to assess how restricted flow conditions influence water movement.

After establishing the hydrologic behaviour under idealized conditions, the analysis was extended to the Amira marsh, the constructed wetland with existing geomorphological and hydrological data. This second phase of the study assesses the model performance under more complex and realistic conditions. The three configurations of the Amira marsh described above (case S1, case S2, and case S3) are examined. These scenarios were tested using two types of tidal forcing: an idealized sinusoidal tide and measured tidal data, allowing for a deep evaluation of how tidal variability influence marsh hydrodynamics.

5.1 Simplified salt marsh with sinusoidal tide

In the first set of simulations, conducted on case S (S0, S1, and S2), five representative timesteps were selected for the visualization of the results (Figure 31). These timesteps were specifically chosen from the final phase of the simulation, ensuring that the results are no longer influenced by the initial conditions and reflect the stabilized, typical tidal behaviour:

1. 3420 minutes (minimum tidal elevation);
2. 3600 minutes (mean sea level with rising tide);
3. 3780 minutes (maximum tidal elevation);
4. 3960 minutes (mean sea level with falling tide);
5. 4140 minutes (minimum tidal elevation).

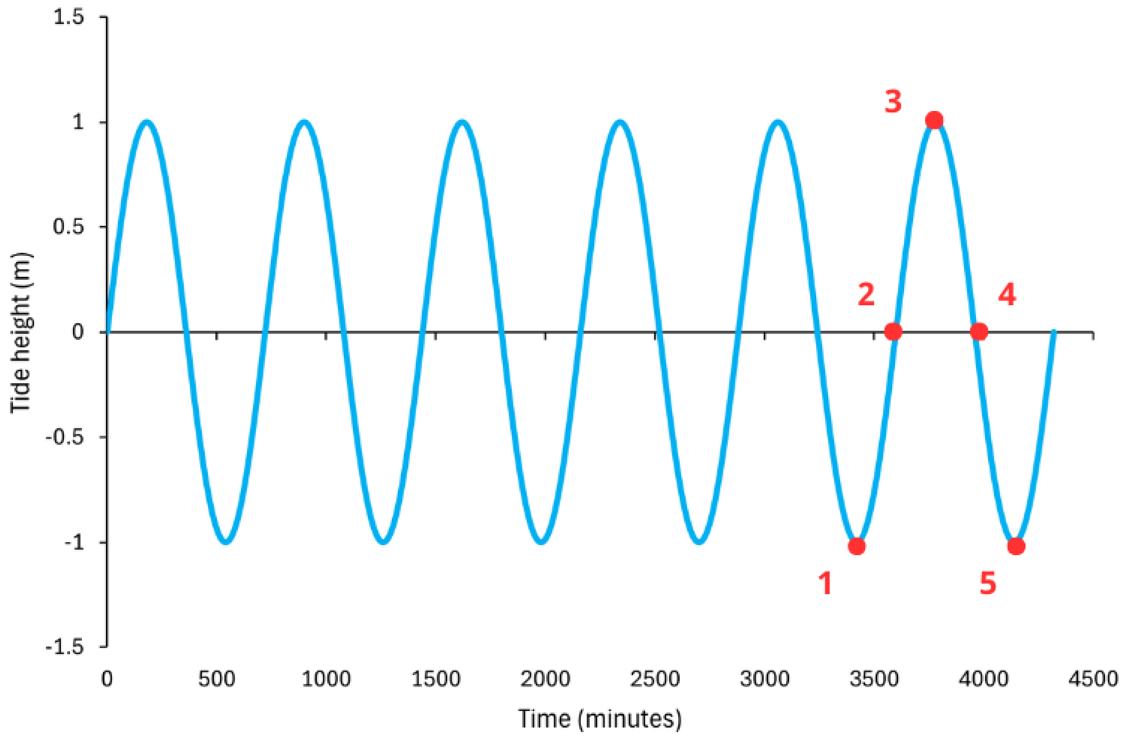

Figure 31: Sinusoidal tide applied in the simulations. The five selected timesteps for result visualisation are highlighted in red.

5.1.1 Setting "a": three-side drainage

As previously mentioned, the simulations were initially run with Dirichelt / seepage counditions applied to both the front and the two lateral surfaces of the domain.

As shown in Figure 32, the saturation levels degree S_w fluctuated significantly over the course of the tidal oscillation. At time 1 (3420 minutes), the domain was predominantly unsaturated, with slight variations in saturation across the front and lateral edges, where values were lower. In contrast, the central regions exhibited higher saturation, reaching values around S_w= 0.75. This trend became more pronounced at time 2 (3600 minutes), when saturation levels on the top surface dropped further, with some areas reaching values as low as S_w= 0.55. As the tide peaked at 1 m (time 3), the entire marsh became fully saturated. When the tide began to fall (time 4), it became clear that while the outer regions, particularly along the front and sides, drained rapidly, the inner zones remained saturated for a longer period. By the end of the cycle (time 5), saturation levels returned to values similar to those observed at the time 1, with the outer portions of the marsh showing a slightly lower saturation degree.

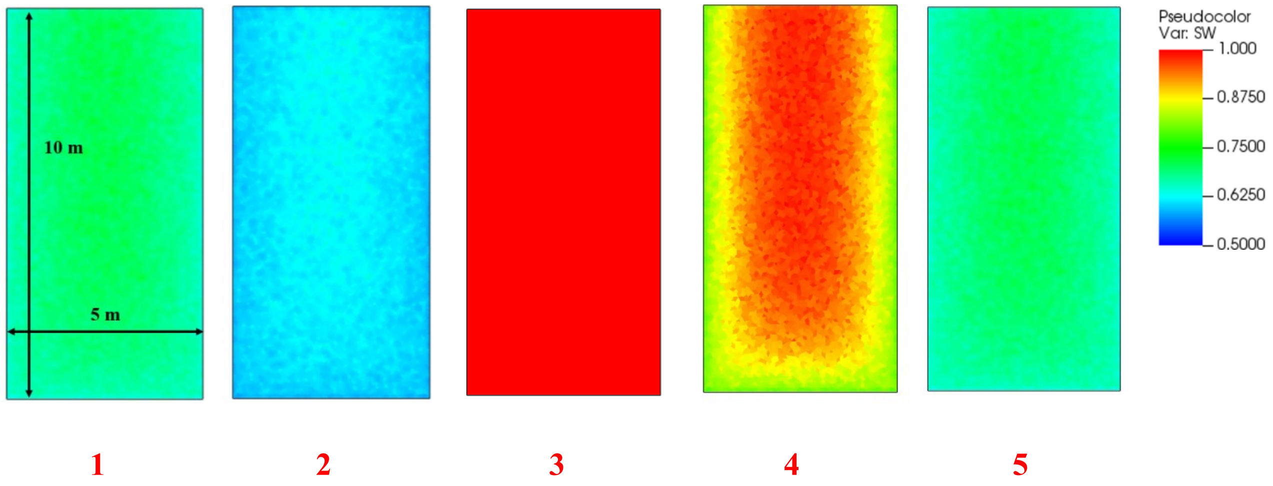

Figure 32: Case S0a - saturation distribution on the marsh top surface for the selected five representative times. A sinusoidal tide is imposed.

In terms of pressure head evolution, at time 1 the values on the marsh surface were negative, reflecting water levels below the sal marsh platform that is characterized by a 0.5 m above msl elevation. As the tide rose to 1 m, the pressure head increased and shifted to positive values, reaching approximately H_w=0.45 m. Following the peak tide, as water levels began to fall, the pressure head gradually returned to negative values, reflecting a decrease in hydraulic pressure as the marsh drained. This behavior can be clearly observed in Figure 33, which visualizes the pressure head evolution throughout the simulation at the 5 selected times.

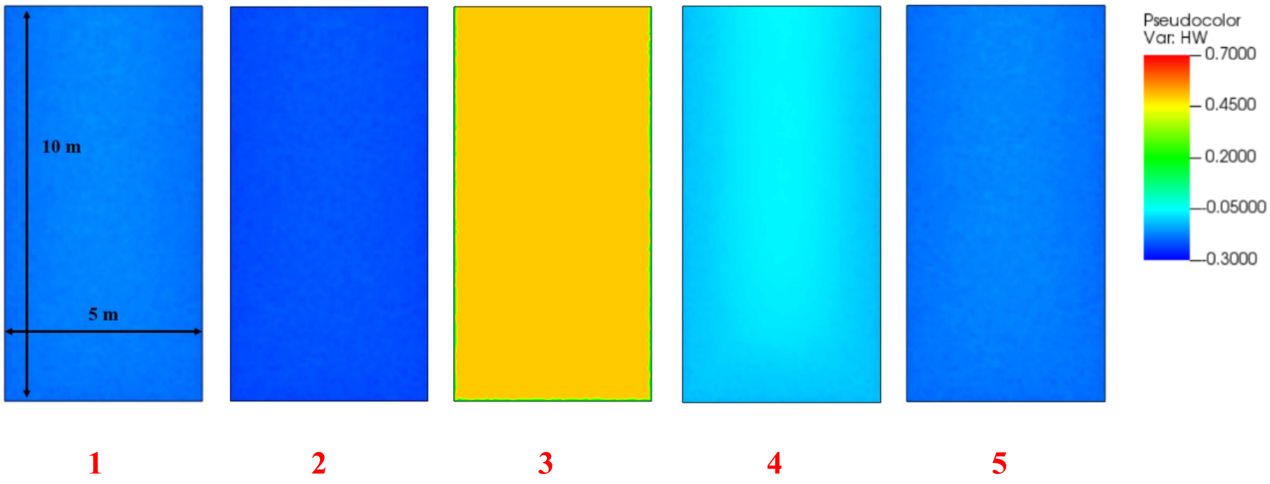

Figure 33: Case S0a - pressure head distribution (m) on the simple marsh top surface for the five representative times. A sinusoidal tide is imposed.

By generating cross-sectional slices through the middle of the marsh, the internal distribution of S_w was visualized, as shown in Figure 34. At a tide height of -1 m (time 1), the water table established within the salt marsh body ($S_w = 1$) exhibited a convex profile, with a lower elevation near the lateral surfaces indicating that water drainage from the central portion of the mash is ongoing. As the tide began to rise, the depth of the water table appeared more flat across the marsh. At the maximum tide level, the entire marsh became fully saturated. As the tide decreased, the regions near the lateral surfaces were the first to drain, while the inner area remained completely saturated, as indicated by the red colour.

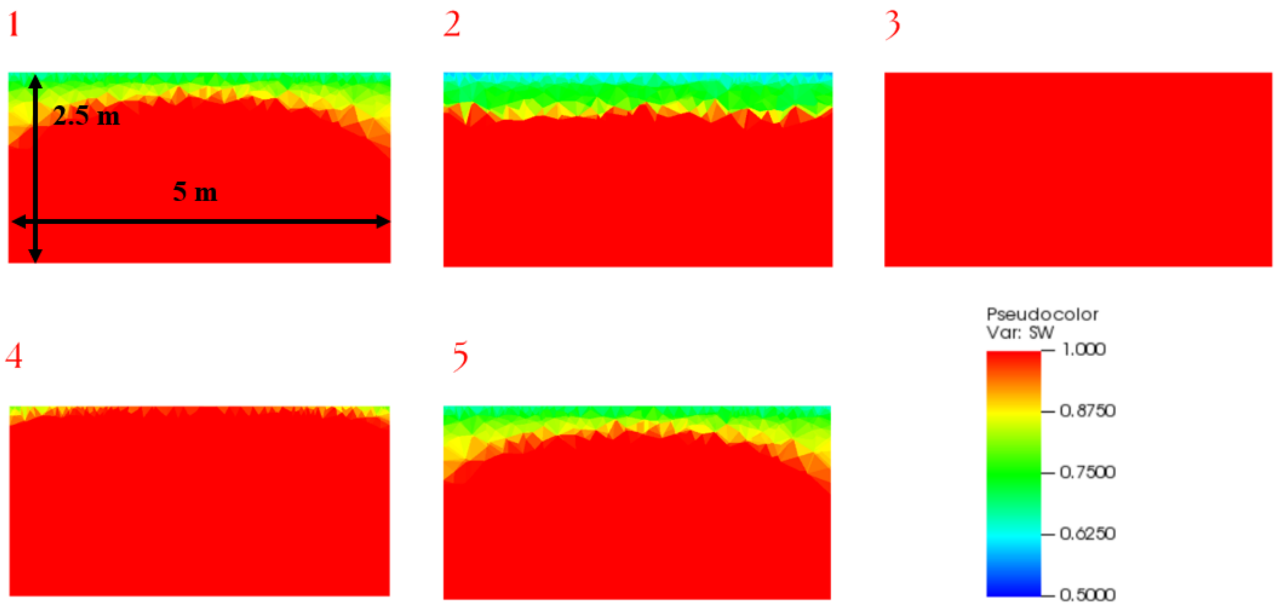

Figure 34: Case S0a - saturation distribution on a vertical cross section through the simple marsh at the five representative times. A sinusoidal tide is imposed.

In the next phase of the simulation, an 8-m long, 70-cm wide, and 35-cm deep creek was introduced crossing the marsh (case S1a). As shown in Figure 35, at time 1, the top surface of the marsh was not fully saturated. Examining the bottom surface of the creek, the inner section was nearly saturated, while the area close to the channel outlet t showed significantly lower saturation values. At time 2, both the top surface and the channel bottom showed a relatively low S_w, in the range between 0.6 and 0.7, with the distribution becoming more uniform across the channel, although the outer areas still exhibited a slightly lower saturation value. At time 3, when the tide fully inundated the marsh, the entire system reached full saturation. As the tide began to fall, it was evident that the outer regions, along with the areas surrounding the channel, drained rapidly, leaving only a small saturated zone near the inner portion of the marsh. The bottom of the channel, however, remained saturated. Finally, by the end of the cycle, the saturation conditions returned to levels similar to those observed at the time 1.

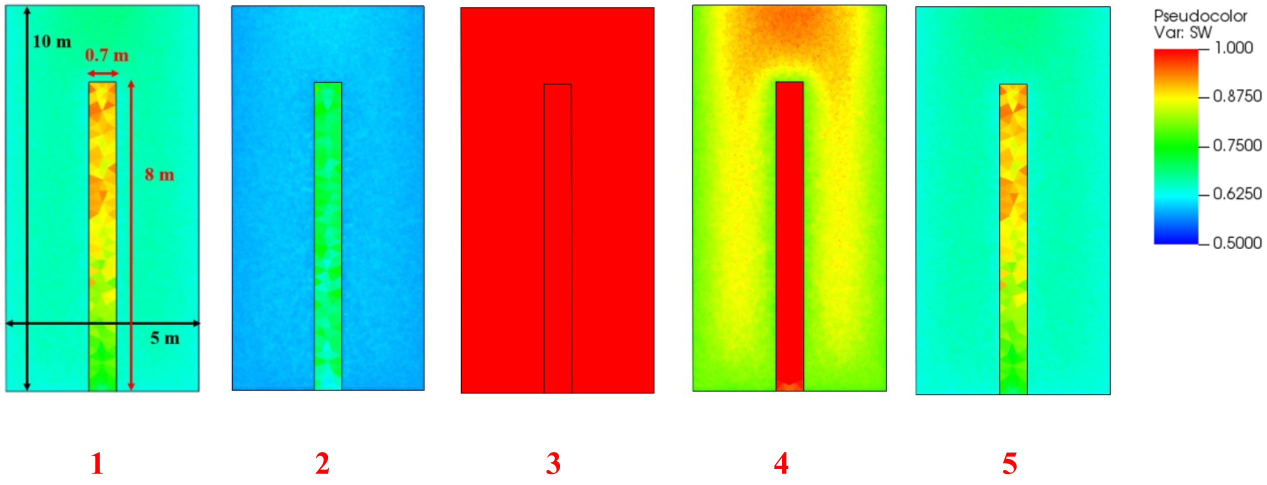

Figure 35: Case S1a - saturation distribution on the marsh top /creek bottom for the selected five representative times. A sinusoidal tide is imposed.

Focusing on the evolution of the potential head (Figure 36), initial values were negative reflecting low water levels. As the tide reached its peak at 1 m above msl, the pressure head shifted to positive values, as expected with the rising water levels. After the tide began to fall, the pressure head gradually returned to negative values, corresponding to the draining of the top surface. The channel exhibited a relatively uniform pressure head distribution, with consistent values from the inner part to the region near the outlet.

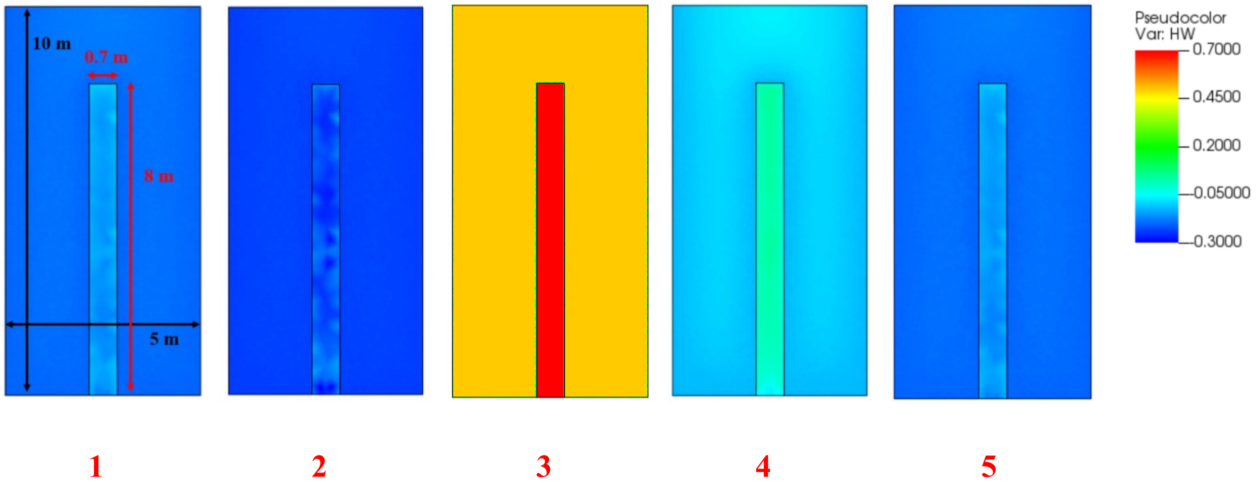

Figure 36: Case S1a - pressure head distribution on the marsh top /creek bottom for the selected five representative times. A sinusoidal tide is imposed.

The outcomes in terms of S_w along a vertical cross-sections of the marsh (Figure 37) clearly highlight the effect of the tidal creek. At time 1, the water table exhibited a convex profile similar to that obtained for case S0a. At time 2, i.e. tidal elevation equal to 0 m above msl and rising tide condition, the saturation degree at the marsh top was lower ($S_w = 0.5$) than that observed in case S0a ($S_w = 0.75$). Moreover, the water table changed to a concave profile with the deepest location in the inner marsh where the creek, whose bottom depth is +0.15 m above msl, is still draining groundwater from the central marsh. When the tide reached 1 m, the entire marsh became fully saturated. As the tide decreased (time 4), the regions near the lateral surfaces were the first to drain, and in this case also the ones in proximity of the creek banks were characterized by a certain desaturation depth. This was different from case S0a, when the inner area remained completely saturated. By the final time, as the tide reached the minimum value, the characteristic curvature of the water table reappeared.

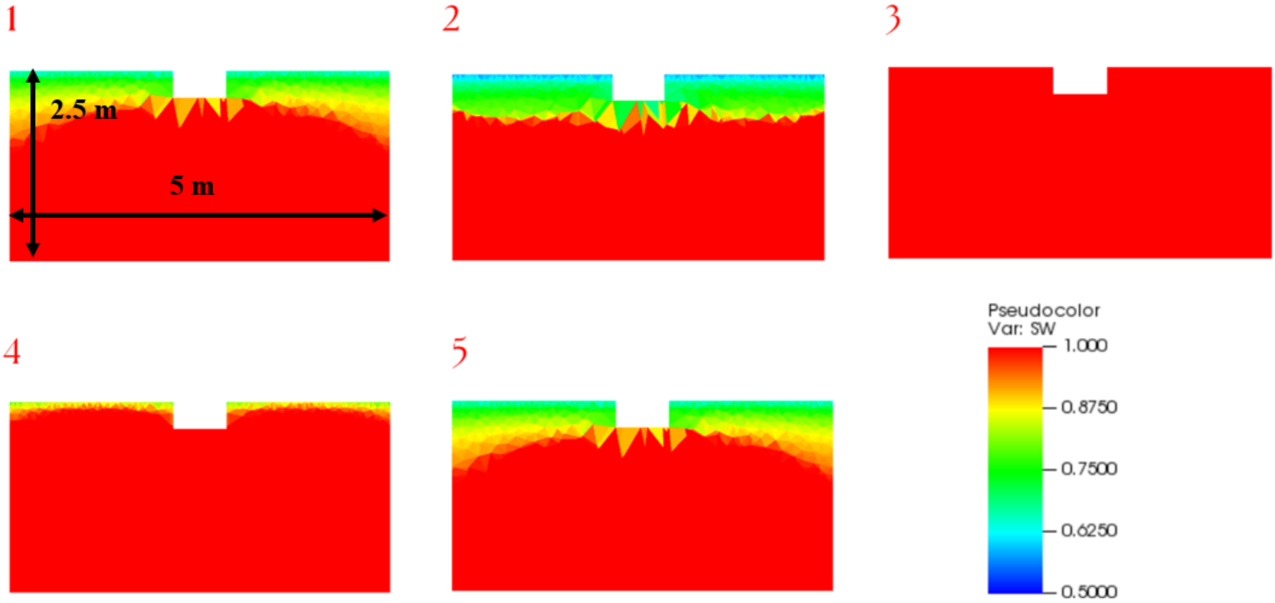

Figure 37: S1a - saturation distribution on a vertical cross section through the simple marsh at the five representative times. A sinusoidal tide is imposed.

Lastly, a simulation featuring a meandering tidal creek (case S2a) was conducted to better replicate the natural morphology of salt marshes commonly found in lagoon environments. As shown in Figure 38, the evolution of saturation followed a pattern like that observed in case S1a. Initially, the saturation level was uniform across the top surface, with slightly higher values at the bottom of the channel, which is deeper, and near the back surface, which is further away from the draining elements. At time 2, the saturation degree decreased further. As the tide reached its peak, the marsh became fully saturated, with $S_w = 1$ across the entire domain. When the tide fall, much like in the straight-creek marsh configuration, the lateral sides together with the areas surrounding the creek drained rapidly, while the inner zone near the back surface remained saturated. By the final timestep, at 4140 minutes, the saturation conditions returned to levels similar to those observed at time 1.

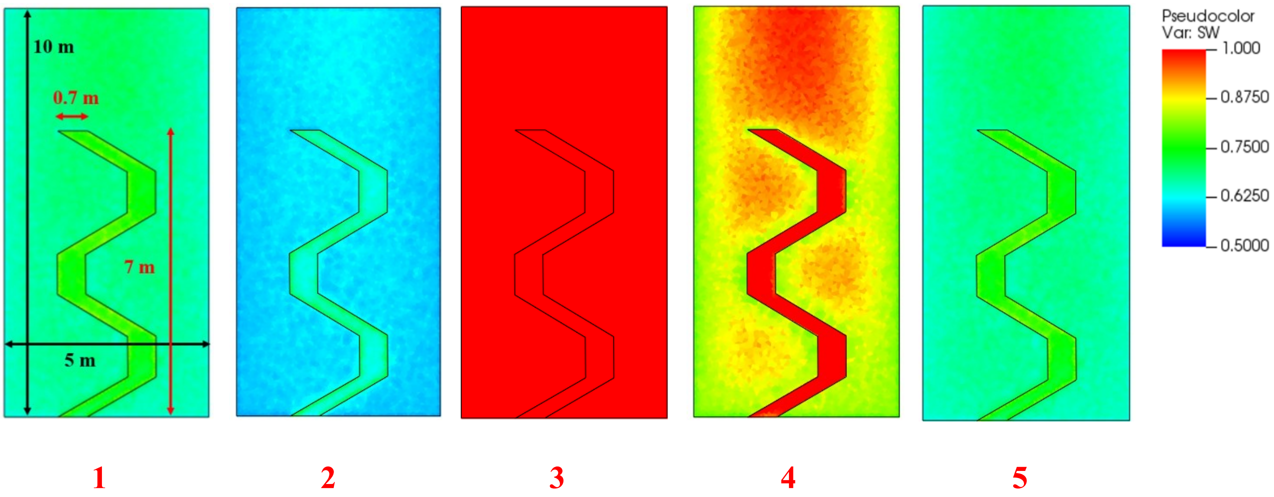

Figure 38: Case S2a - saturation distribution on the marsh top /creek bottom for the selected five representative times. A sinusoidal tide is imposed.

Again, quite similarly to case S0a and case S1a, the H_w values on the marsh surface and creek bottom at time 1 were negative. As the tide rose to its peak, the pressure head increased, transitioning to positive values. Once again when the tide began to fall, the pressure head gradually shifted back to negative values. Notably, the bottom of the channel showed a relatively uniform pressure head distribution, with consistent values from the inner sections to the outlet. This behaviour differed slightly from those at the top surface, influenced by the elevation of the channel bottom. The results of the potential head evolution are presented in Figure 39.

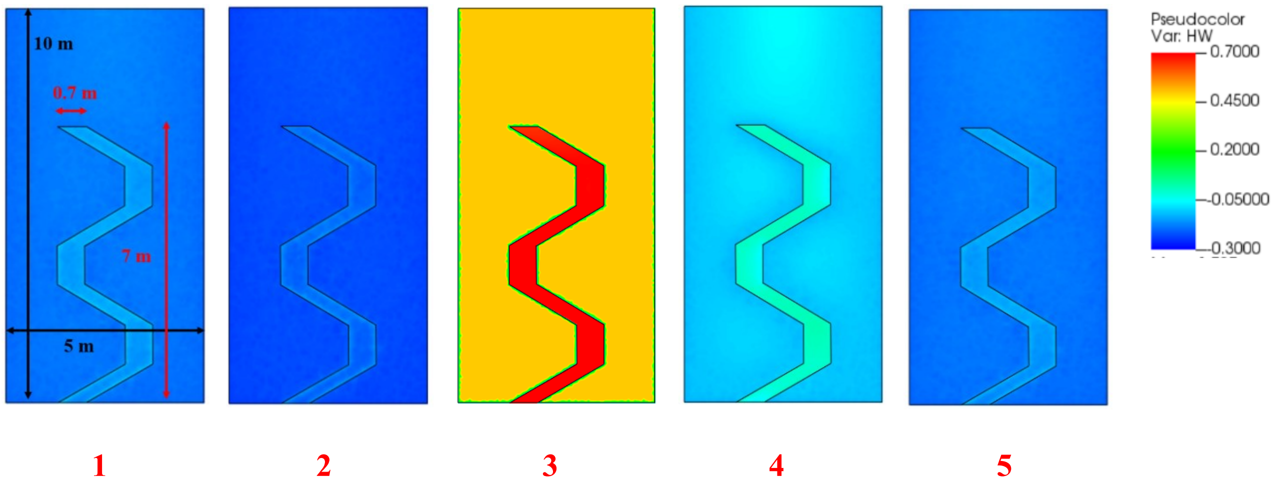

Figure 39: Case S2a - pressure head distribution on the marsh top /creek bottom for the selected five representative times. A sinusoidal tide is imposed.

Lastly, the behaviour of S_w along a vertical cross-section of the marsh at $Y = 5$ m is shown in Figure 40. The saturation evolution was quite similar to that obtained in case S1a, with a profile of the water table that shifted from convex (time 1) to gently concave (time 2). Notice that the shallower creek depth made the concavity less evident than in case S1a. During the tide falling phase, lower S_w values were observed on the lateral surfaces as well as in the areas surrounding the creek. It is also important to note that the extent of desaturation varies depending on the specific cross-section analysed. The particular cross-section shown in the figure was taken from the central region of the marsh, which likely influences the observed saturation distribution.

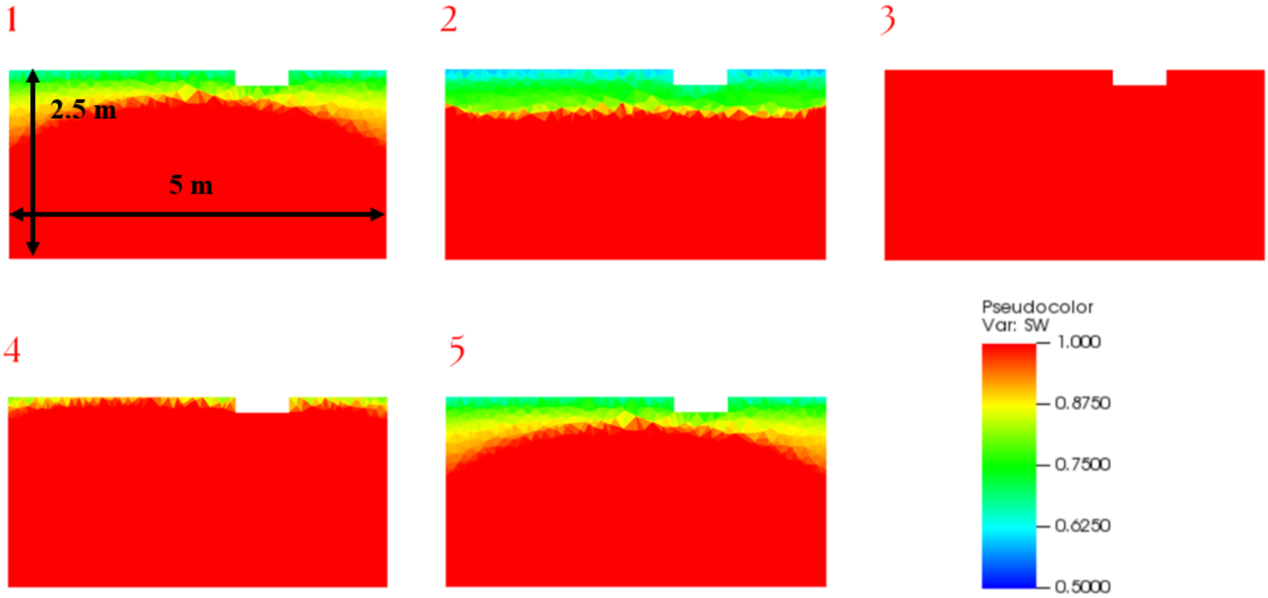

Figure 40: Case S2a - saturation distribution on a vertical cross section through the simple marsh at the five representative times. A sinusoidal tide is imposed.

A comparison was made between the three configurations by analysing the evolution of S_w at the location with X = -1 m, Y = 6.5 m, Z = 0.5 m above msl (Figure 41). Notice that X = 0 m corresponds to the symmetry axis of the marsh and Y = 0 m to the front boundary. Saturation degree was reported with a timestep of 10 minutes.

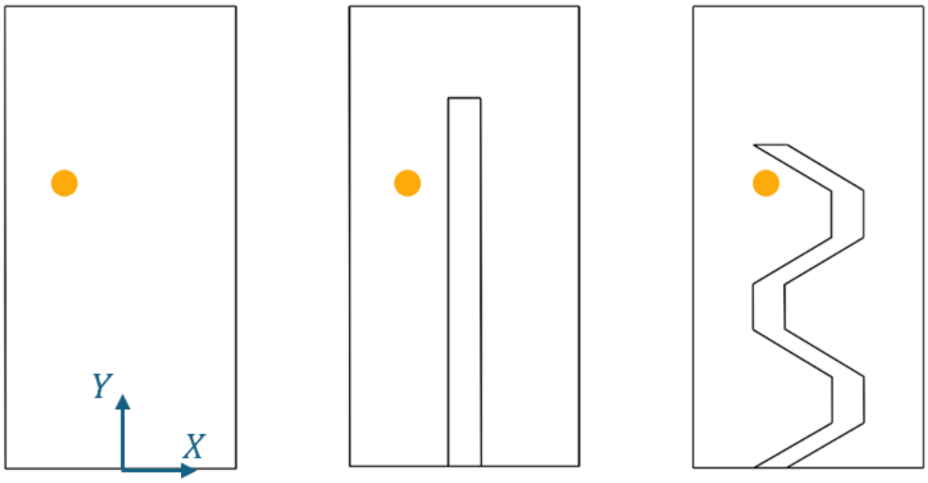

Figure 41: Location selected for the saturation evolution comparison: X = -1 m, Y = 6.5 m, Z = 0.5 m.

Figure 42 shows that S_w kept a value equal to 1 for a longer period of time (20 minutes more within each cycle) in case S0a than in the other two cases. This indicates that the presence of a tidal creek effectively helps in draining groundwater, creating unsaturated conditions in the upper soil for longer periods of time. In case S0a the minimum saturation degree was $S_w = 0.6$ (Figure 43). Throughout each cycle, case S1a exhibited lower saturation levels compared to the other two cases. This can be attributed to the specific location selected for visualizing the S_w profile over time, as in case S2a the measurement point was located close to the end of the tidal creek, which had a shallower depth (0.15 m) compared to the that in case S1a (0.35 m), affecting the saturation behaviour. However, case S2a showed the most pronounced drop in saturation towards the end of the tidal cycle, $S_w = 0.54$.

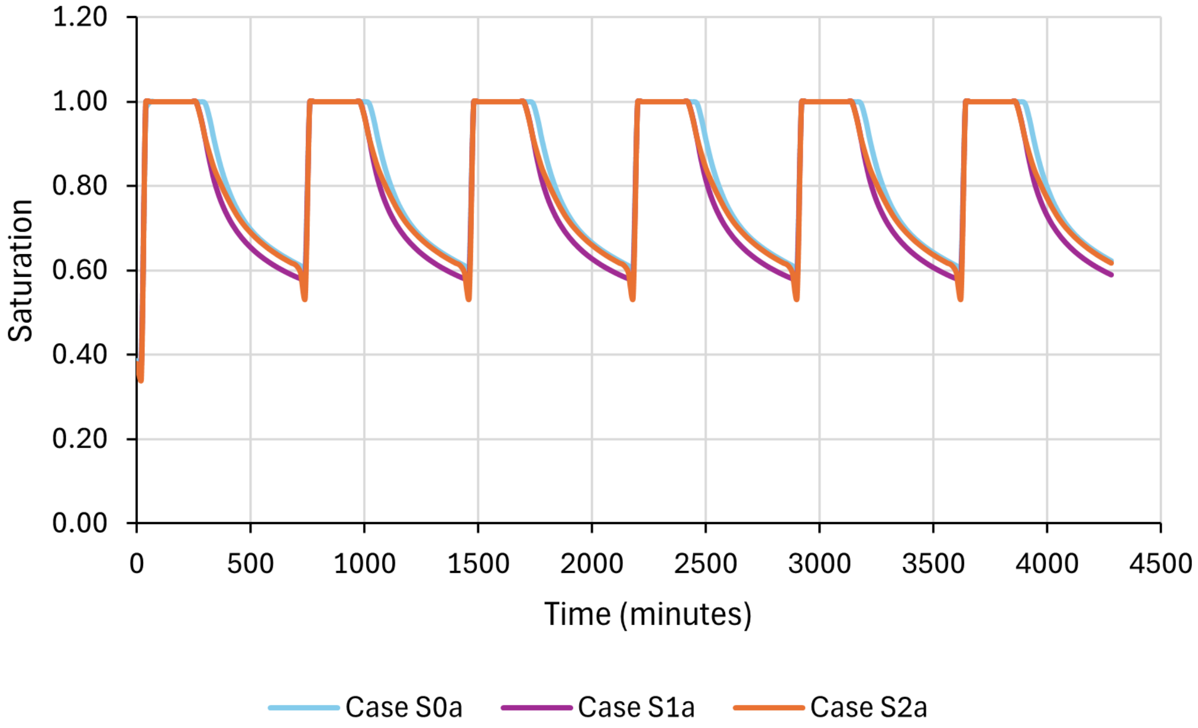

Figure 42: Saturation evolution at location X = -1 m, Y = 6.5 m, Z = 0.5 m above msl for the three simulations with the "a" setting. A sinusoidal tide is imposed.

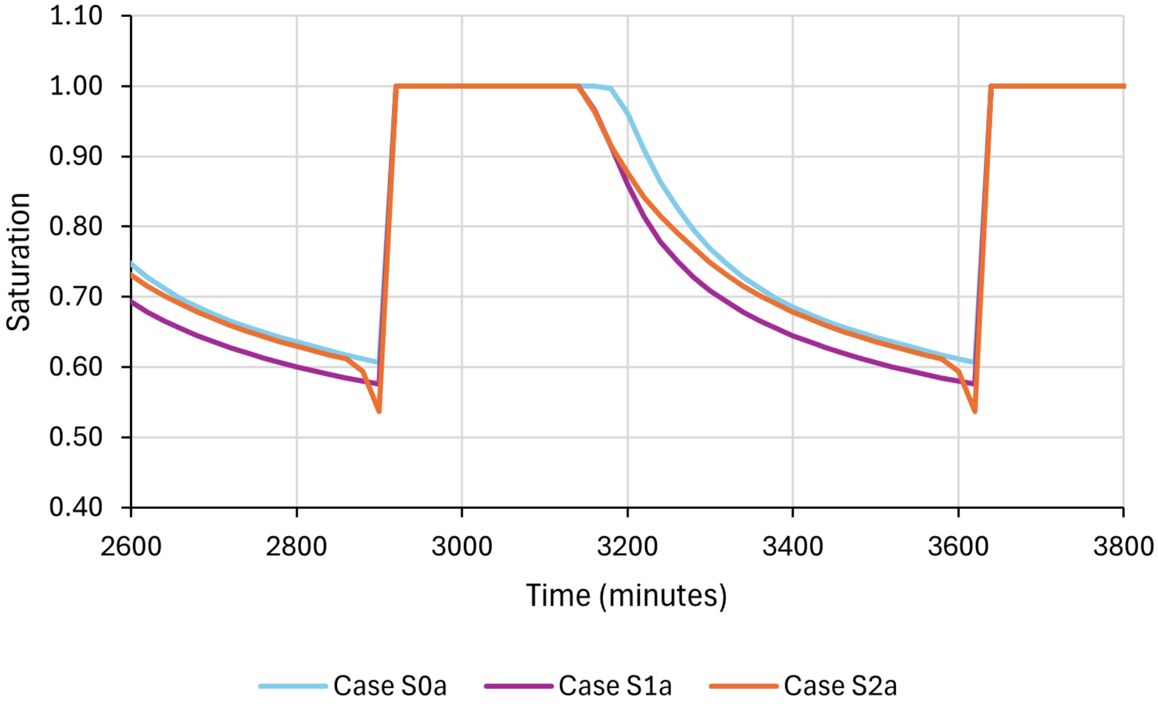

Figure 43: One-cycle saturation evolution at location with coordinates X = -1 m, Y = 6.5 m, Z = 0.5 m above msl for the three simulations with the "a" setting. A sinusoidal tide is imposed.

5.1.2 Setting "b": one-side drainage

Subsequently, three additional simulations were conducted for the three cases S, assuming that only the front side of the simulated salt marsh faces a lagoon channel.

The results in terms of S_w for case S0b are shown in Figure 44. The presence of the lagoon channel on the marsh front boundary only allowed for rapid drainage near the channel but the inner marsh portions were unable to drain. In contrast to the "a" setting, here the lateral zones of the salt marsh remained saturated throughout. At time 1 (3420 minutes), when the domain had experienced the most favourable condition to drainage, more than half of the top surface was still fully saturated, with S_w gradually decreasing towards the front. By time 2 (3600 minutes), saturation degree on the top surface had dropped further, and unsaturated consition extended more towards the inner portion of the marsh. As the tide rose and peaked at 1 m, the marsh became fully saturated. Once the tide began to decline (time 4), the inner zone remained largely saturated, with only a thin portion at the marsh front experiencing a certain desaturation. By the end of the tidal cycle (4140 minutes), saturation levels returned to conditions similar to those observed at time 1.

In terms of pressure head evolution for S0b (Figure 45), it was possible to observe a spatial variability at the top surface greater than in setting “a”. At the beginning of the simulation, the pressure head on the top surface showed negative values near the lagoon channels, gradually shifting to positive values towards the inner marsh portion. As the tide rose to 1 m (time 2 and time 3), the pressure head became entirely positive, reaching approximately $H_w = 0.45$ m over most of the surface, with slightly lower values (around $H_w = 0.20$ m) on the channel edge. As water levels began to fall, the pressure head gradually returned to negative values at the front, decreasing across the entire top surface (step 4 and step 5).

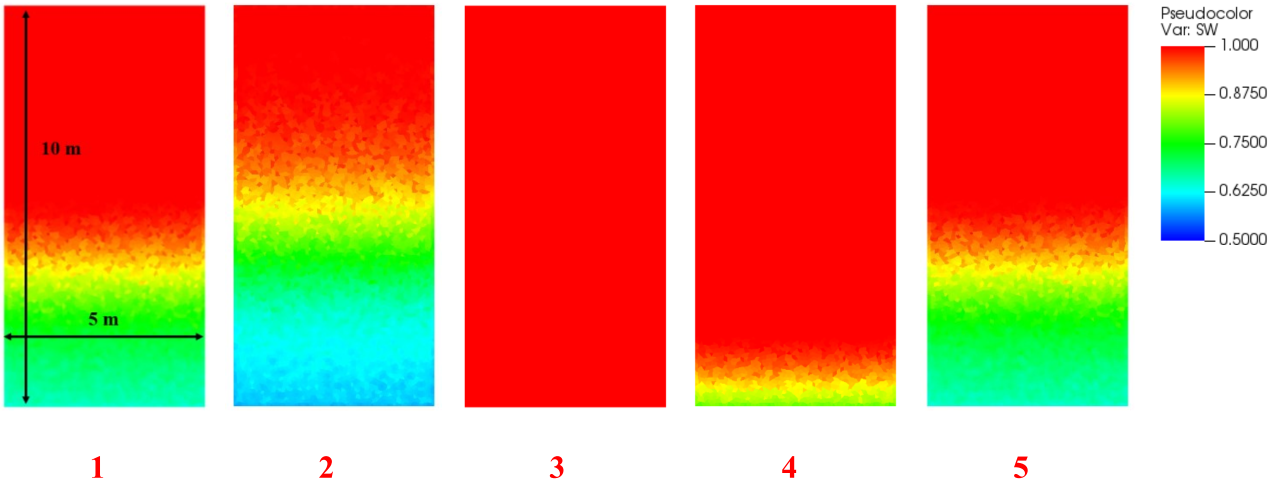

Figure 44: Case S0b - saturation distribution on the marsh top surface for the selected five representative times. A sinusoidal tide is imposed.

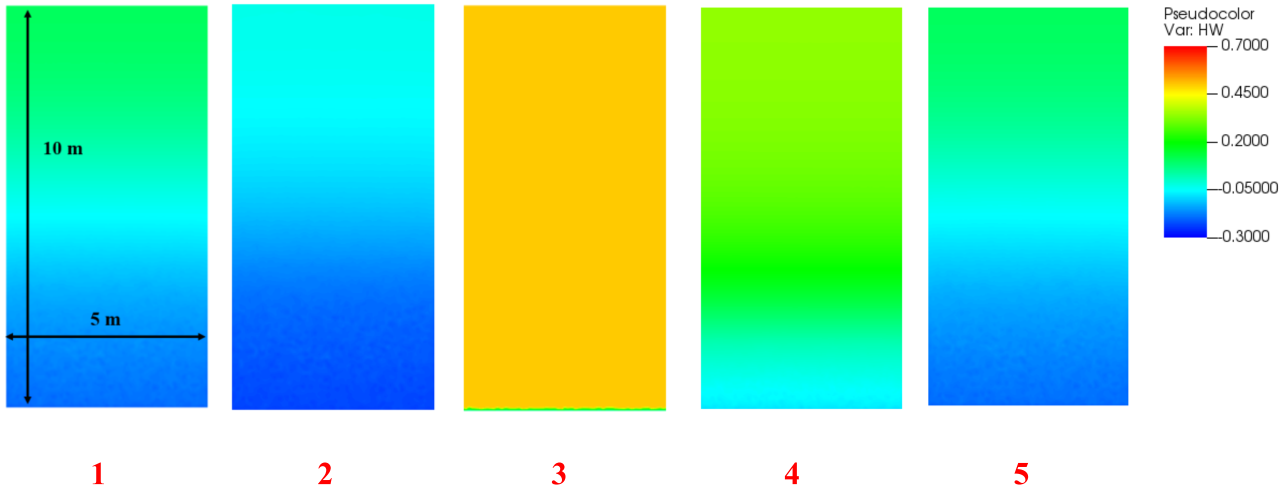

Figure 45: Case S0b - pressure head distribution (m) on the simple marsh top surface for the five representative times. A sinusoidal tide is imposed.

In the case S1b, saturation exhibited a markedly different behavior (Figure 46) compared to case S1a. At time 1, saturation was lower towards the front and increased inland, with a significantly larger unsaturated zone than in case S1a. The influence of the tidal creek was much evident showing lower S_w values near the creek edges. The bottom of the channel had a similar saturation degree near the outlet but remained fully saturated towards the back. At time 2, the behavior was similar, showing saturation values generally lower. At the peak of the tide (step 3), as previously observed, the marsh became fully saturated (S_w = 1). At step 4 the inner and lateral portions of the top surface were still fully saturated, while only the areas near the creek and the front of the marsh were unsaturated. The bottom of the channel remained fully saturated, owing to its lower elevation relative to the top surface. Finally, saturation degree returned to conditions similar to those observed at the step 1.

Focusing on the evolution of the pressure head of S1b (Figure 47), its distribution varied from the front to the back of the marsh, and the influence of the straight creek was more pronounced than in setting “a”. The bottom of the creek exhibited a stronger gradient, with lower H_w values near the inlet and higher values towards the inner marsh. As the tide reached its peak at 1 m, the pressure head on the top surface reached approximately H_w = 0.45 m, while the bottom of the creek remained uniformly saturated. Once the tide began to fall, the pressure head gradually returned to negative values, reflecting the drainage of the top surface.

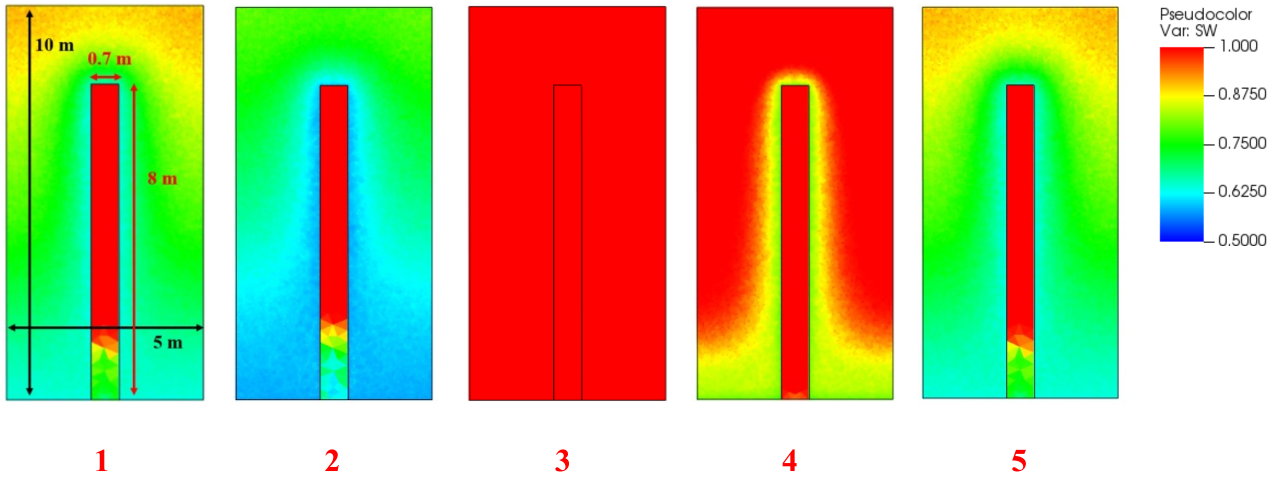

Figure 46: Case S1b - saturation distribution on the marsh top surface for the selected five representative times. A sinusoidal tide is imposed.

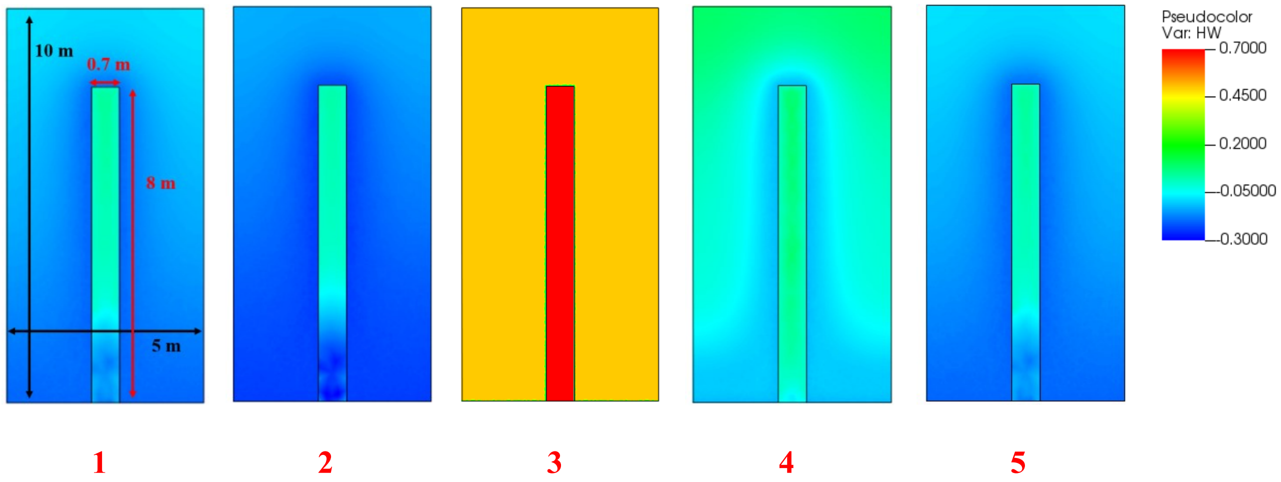

Figure 47: Case S1b - pressure head (m) distribution on the simple marsh top surface for the five representative times. A sinusoidal tide is imposed.

Lastly, the case S2b was investigated. Also in this case, the unsaturated area was much larger than in case S0b, highlighting the impact of the creek in draining the groundwater within the marsh landform. Full saturation persisted only in the inner marsh, while areas near the creek edges and the tidal channel at the marsh front desaturated more rapidly (Figure 48).

As in the previous cases, the pressure head distribution varied from the front to the back of the salt marsh, and the bottom of the tidal creek displayed a stronger gradient, with lower values near the inlet and higher values toward the inner part of the marsh. By time 3, the bottom of the creek exhibited a uniform pressure head that was higher than that of the top surface, reflecting the difference in elevation between the two. Once the tide began to fall, the pressure head values gradually decreased, refelcting the drainage of the top surface (Figure 49).

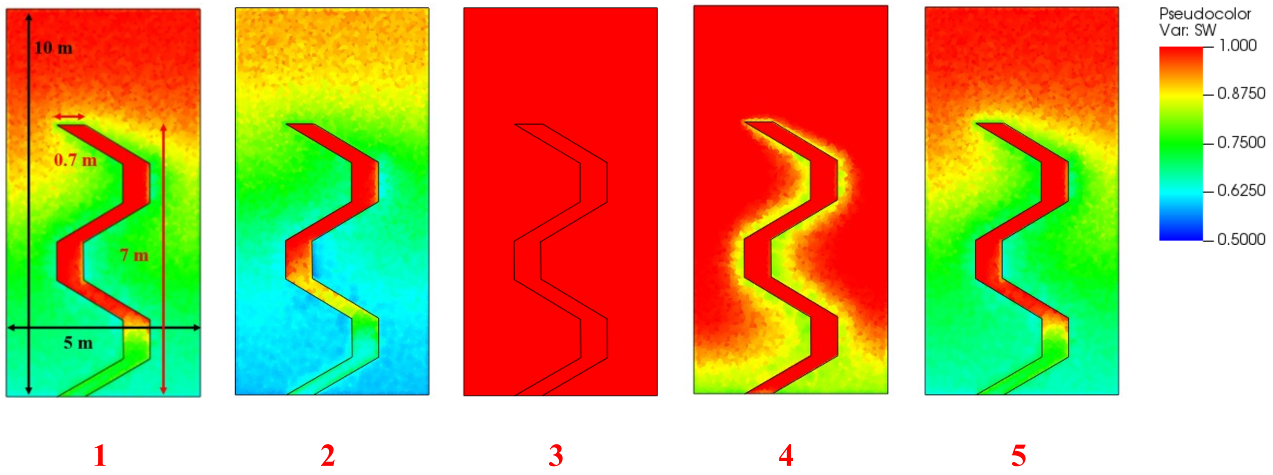

Figure 48: Case S2b - saturation distribution on the marsh top surface for the selected five representative times. A sinusoidal tide is imposed.

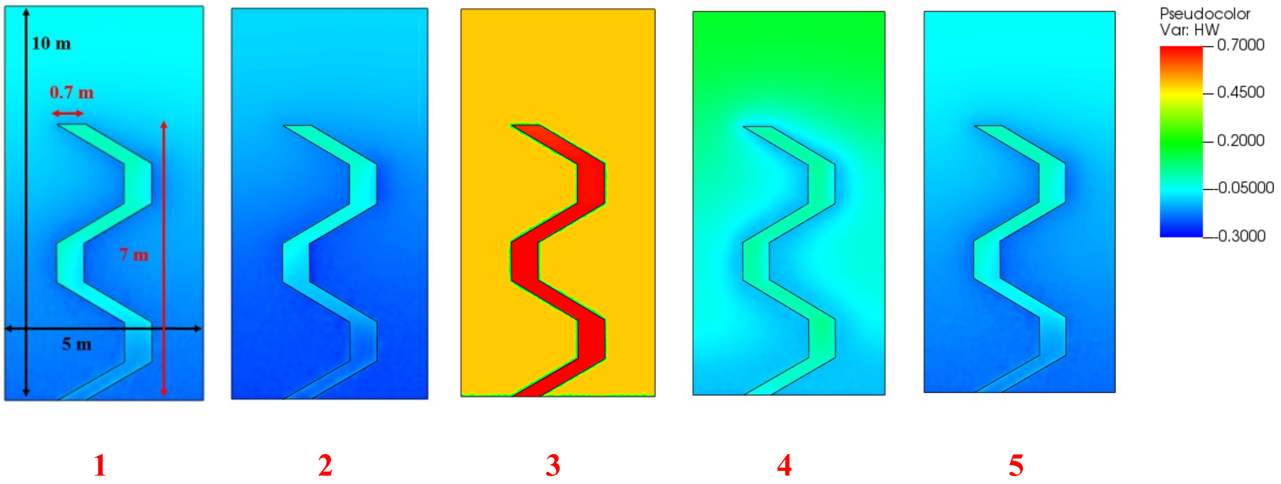

Figure 49: Case S2b - pressure head (m) distribution on the simple marsh top surface for the five representative times. A sinusoidal tide is imposed.

For the “b” setting too, we proposed a comparison of the saturation evolution at location X = -1 m, Y = 6.5 m, Z = 0.5 m above msl (Figure 50 and Figure 51). In general, the saturation degree observed in “b” setting are significantly higher than those in “a” setting, as water is allowed to drain only through the front boundary. In particular, the case S0b is characterised by higher saturation degree for an extended period, with $S_w = 1$ for 340 minutes more than in case S1b and case S2b. This indicates a slower drainage process in case S0b, which limits the drainage and thereby traps the water in the system for longer time.

Among the investigated configurations, case S1b achieved the lowest saturation degree throughout the cycles, with a minimum of approximately $S_w = 0.63$. In case S2b a minimum saturation value of $S_w = 0.79$. This can be attributed to the more complex flow paths introduced by the creek geometry, as well as the specific measurement point chosen for comparison, which was located at the end of the meandering creek where the depth is shallower. This shallower depth likely influenced the local drainage characteristics, locally affecting the overall saturation behaviour.

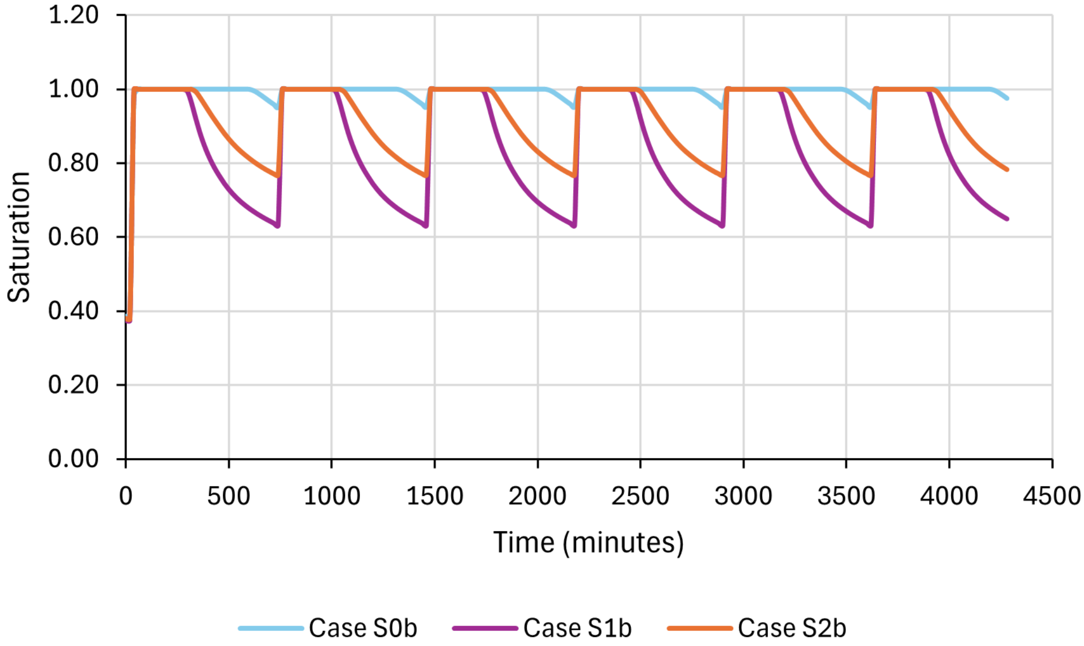

Figure 50: Saturation evolution at location with coordinates X = -1 m, Y = 6.5 m, Z = 0.5 m above msl for the three simulations with the "b" setting. A sinusoidal tide is imposed.

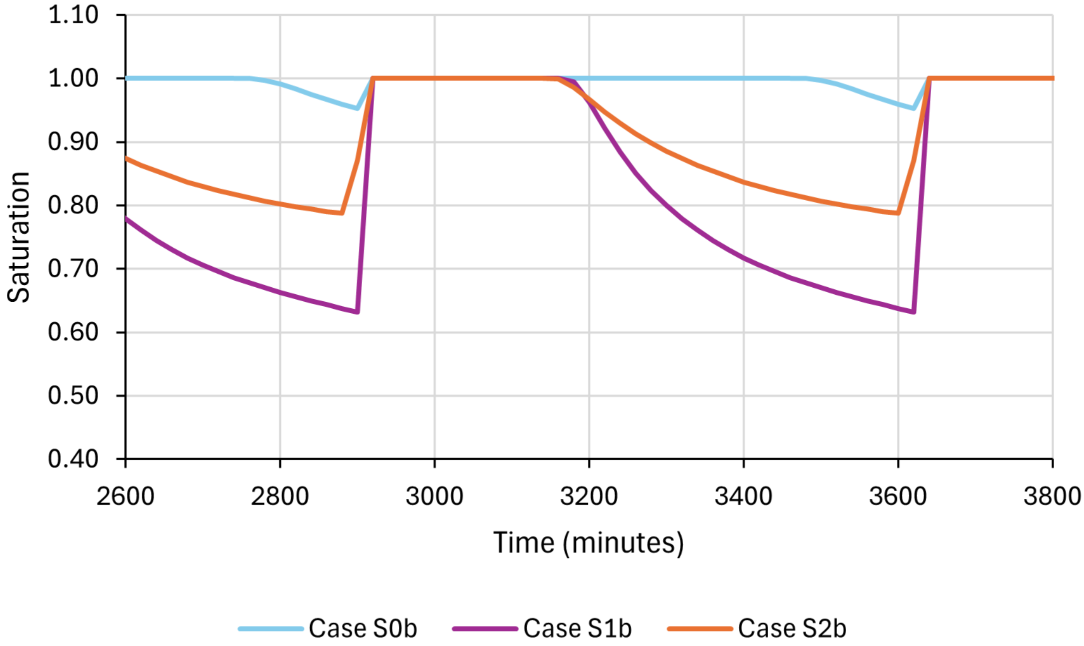

Figure 51: One-cycle saturation evolution at location with coordinates X = -1 m, Y = 6.5 m, Z = 0.5 m above msl for the three simulations with the "b" setting. A sinusoidal tide is imposed.

5.2 Simplified salt marsh with real tide

The real tide fluctuation recorded in March 2010 in the Venice Lagoon was applied as boundary condition (Figure 52). Also in this case, five representative times have been selected for the visualisation of the results, corresponding to one peak, one low, and representative intermediate values:

1. 18/03/2010 21:00, which corresponds to a tide hight of 0.34 m above msl;
2. 19/03/2010 07:00, which corresponds to a tide hight of -0.29 m above msl;
3. 19/03/2010 16:00, which corresponds to a tide hight of -0.01 m above msl;
4. 19/03/2010 22:00, which corresponds to a tide hight of 0.41 m above msl;
5. 30/03/2010 23:00, which corresponds to a tide hight of 1.08 m above msl.

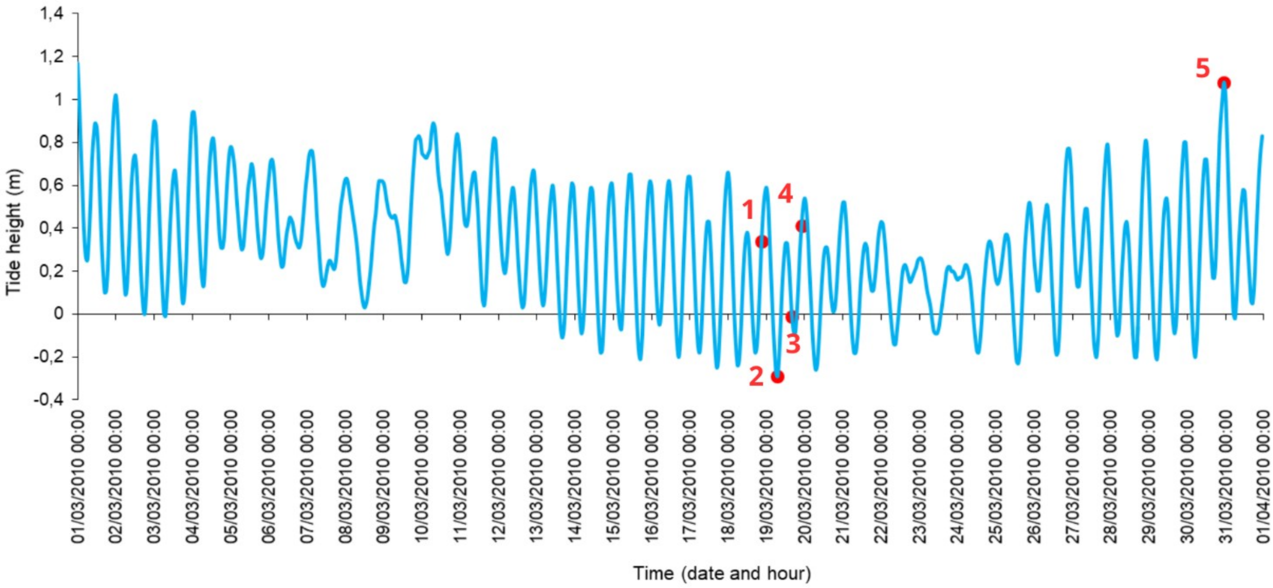

Figure 52: Real tide evolution recorded in March 2010 and used as boundary condition. The five selected times for result visualisation are highlighted in red.

Examining the saturation evolution for case S0a, the lower saturation values observed at time 1 developed along the three sides facing the lagoon, while the inner part remained fully saturated. At time 2, when the tide dropped to its minimum of −0.29 m above msl, the marsh appeared more saturated than expected, with nearly the entire surface fully saturated. The behaviour of the subsequent times aligned more closely with expectations, and as the tidal peaked at 1.08 m above msl the surface was again fully saturated. The results are presented in Figure 53.

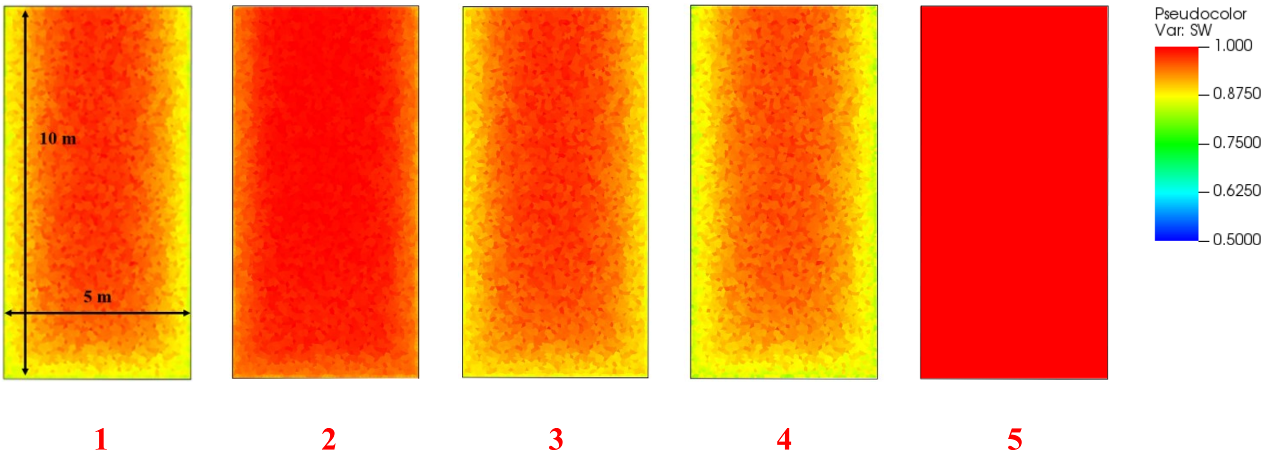

Figure 53: Case S0a - saturation distribution on the marsh top surface for the selected five representative times. The March 2010 tide records are imposed.

To further investigate the saturation behaviour, a graph versus time was generated showing the comparison between tidal fluctuations and S_w at the point with coordinates X = −2.5 m, Y = 6 m, Z = 0.5 m above msl (Figure 54). By restricting the y-axis to the hours corresponding to the first four times, a relationship between the two variables became apparent. Given that the ground elevation at the selected point was equal to 0.5 m above msl, only the highest tidal peaks were able to induce full saturation on the marsh platform, whereas smaller tidal oscillations did not raise the water level enough to inundate the point. Following each saturation peak, a rapid decline in saturation was observed, which progressively slowed as the tide began to rise again but remained below the 0.5 m above msl elevation threshold. By combining the information from Figure 53 and Figure 54, a clearer understanding of the process was achieved. At time 1, when the tide was rising, saturation showed relatively low values along the edges as this time followed a 20-hour time interval with the tidal level always below the marsh elevation. At time 2, although the tide is lower than the value in time 1, S_w was larger because the time interval from the last marsh submersion was 6 hours only. A similar consideration holds for time step 3 and even more for time 4.

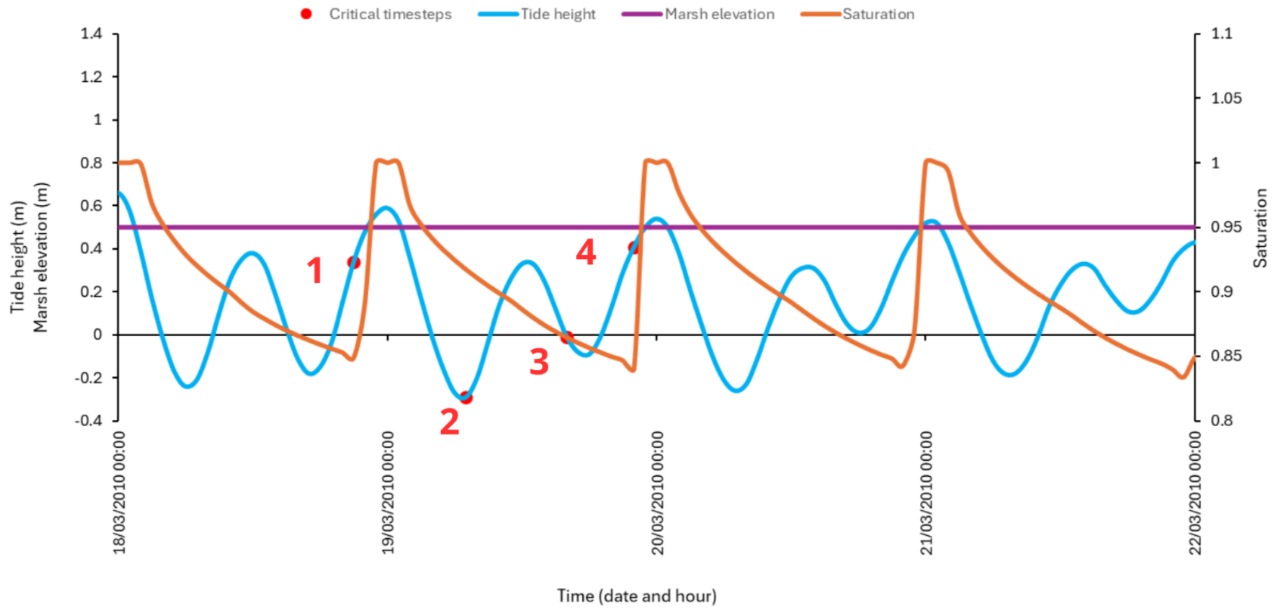

Figure 54: Case S0b - tide height between March 18 and 22, 2010, and saturation evolution at the point with coordinates $X = -2.5$ m, $Y = 6$ m, $Z = 0.5$ m above msl. The selected times and the elevation of the salt marsh are reported.

The pressure head showed little variation for the times where the tide remained below 0.5 m above msl, i.e. below the marsh platform, maintaining a negative value of approximately -0.5 m. When the tide reached its peak of 1.08 m (step 5), the trend reversed with positive values observed across the entire surface, and just slightly lower H_w values along the front and lateral edges of the marsh (Figure 55).

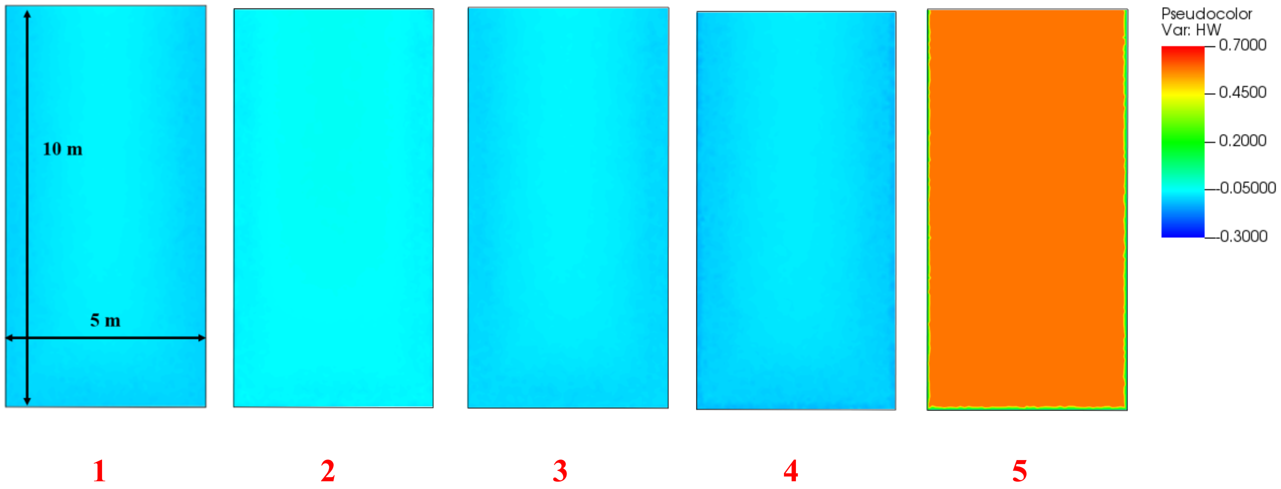

Figure 55: Case S0a - pressure head (m) distribution on the simple marsh top surface for the five representative times. The March 2010 tide records are imposed.

Including a straight creek (case S1a) caused the development of a larger unsaturated zone in the inner part of the marsh, especially along the channel edges (Figure 56). Also in this case, time 2, when the minimum tide hight was registered, showed a higher saturation values than other times with higher tide levels due to the phase difference observed between the two variables.

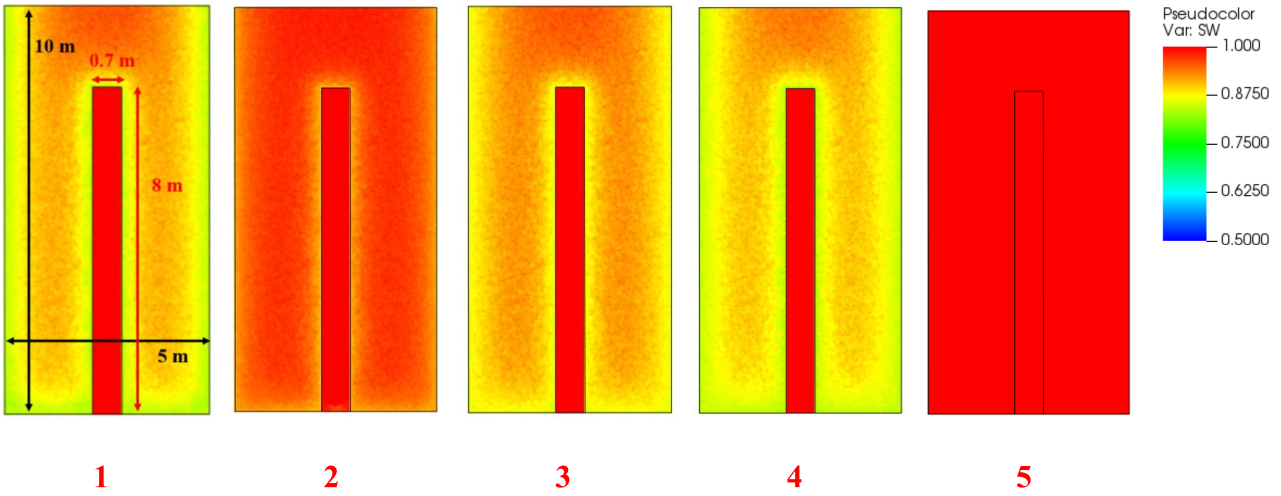

Figure 56: Case S1a - saturation distribution on the marsh top surface for the selected five representative times. The March 2010 tide records are imposed.

Moreover, Figure 57 shows that the pressure head maintained negative values in the first four selected times selected, while positive values were registered only when the tide reached its peak (step 5). The bottom of the channel is characterized by a higher pressure head due to its lower elevation. Again, the difference between case S0a and case S1a is more evident in term of S_w than H_w.

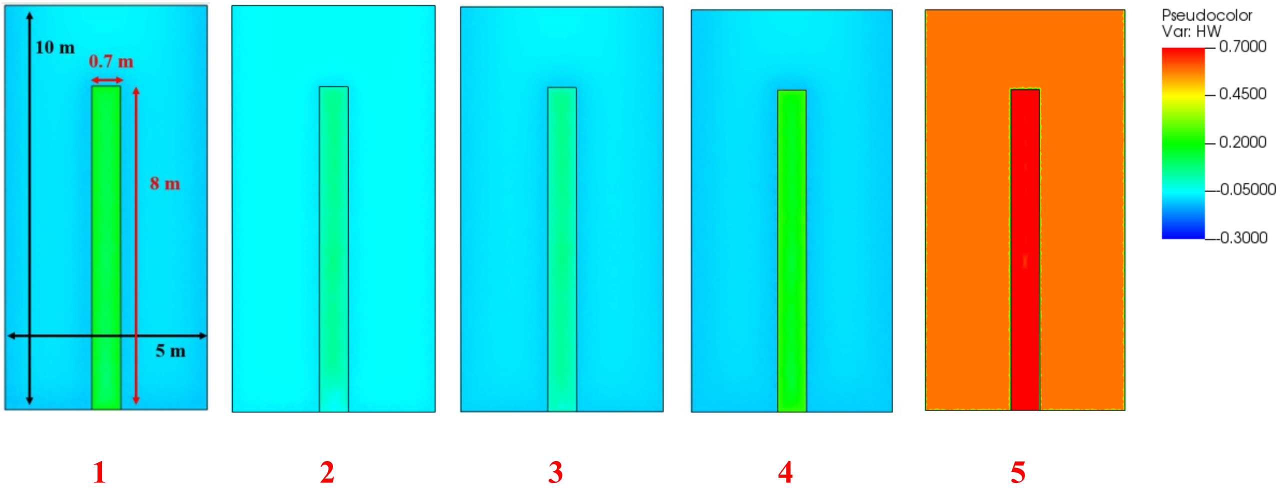

Figure 57: Case S1a - pressure head (m) distribution on the simple marsh top surface for the five representative times. The March 2010 tide records are imposed.

Lastly, the case S2a was analysed. Saturation exhibited an evolution similar to case S1a, while the pressure head showed its main difference in the gradient along the channel bottom surface, particularly at time 5, with higher values near the inlet where the channel is deeper. The saturation and pressure head evolutions are presented in Figure 58 and Figure 59, respectively.

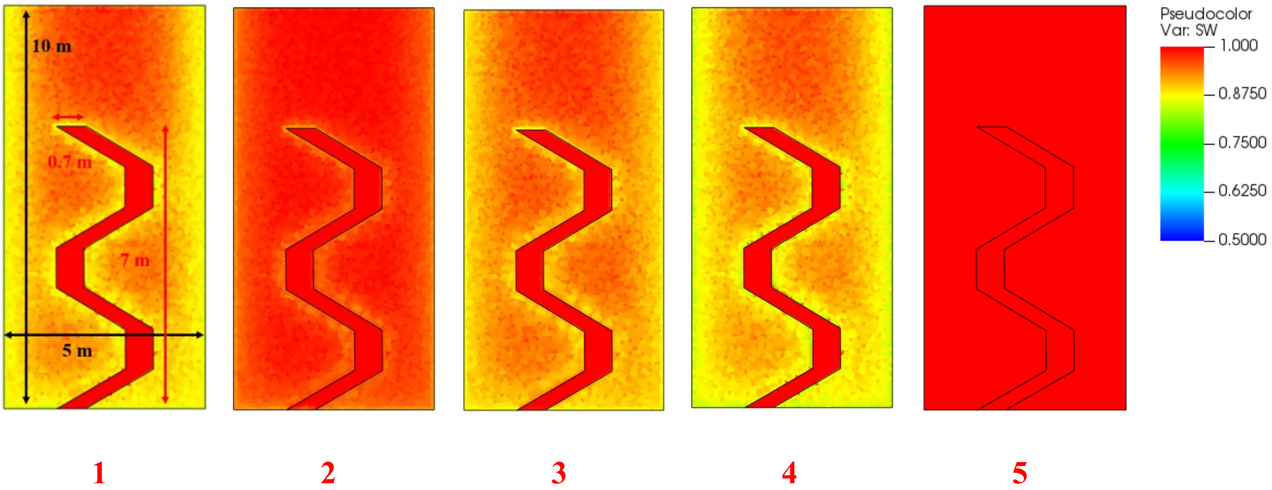

Figure 58: Case S2a - saturation distribution on the marsh top surface for the selected five representative times. The March 2010 tide records are imposed.

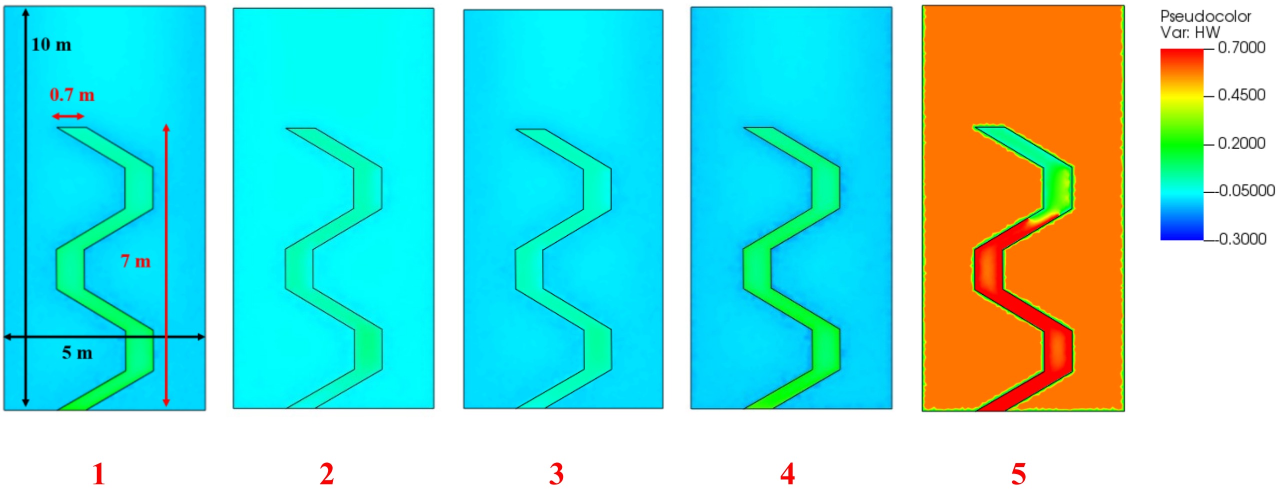

Figure 59: Case S2a - pressure head (m) distribution on the simple marsh top surface for the five representative times. The March 2010 tide records are imposed.

5.3 The Amira salt marsh with a sinusoidal tidal regime

Focusing on the Amira artificial salt marsh section, the analysis was conducted on both saturation and pressure head evolution, following the same methodology as in previous simulations. The simulations were first performed under sinusoidal tidal forcing, as previously described, and results were presented for the same five critical times highlighted in Figure 31.

The distribution of S_w for case A1 (as defined in Figure 22) is provided in Figure 61. Due to its large dimensions and the fact that only one side of the marsh is directly in contact with the lagoon, most of the marsh remained fully saturated. Limited unsaturated conditions established at time 1 and 5 along the boundary of the marsh facing the lagoon. This behaviour is consistent with field observations of the Amira marsh taken on 20 April 2021. As shown in Figure 60, the marsh exhibits high saturation levels and ponding condition in large portions of the landform irrespective of the low tide elevation. The marsh platform is tabular, not intersected by a creek network, confirming that large, flat marsh surfaces tend to remain waterlogged.

Examining the pressure head distribution for A1 (Figure 62), at time 1 a negative pressure head was computed along the side exposed to tidal fluctuations, as well as in areas of higher elevation, particularly in the northern part of the section. The values then became more uniform by time 2, also due to the vertical resolution of the mesh. As the tide began to fall, the pressure head values also declined, returning to levels similar to those observed at the beginning by time 5.

Figure 60: Photo of the Amira salt marsh taken on April 20, 2021, showing high saturation and ponding condition in a large portion of the marsh irrespective of the low tide elevation (courtesy, Pietro Teatini)

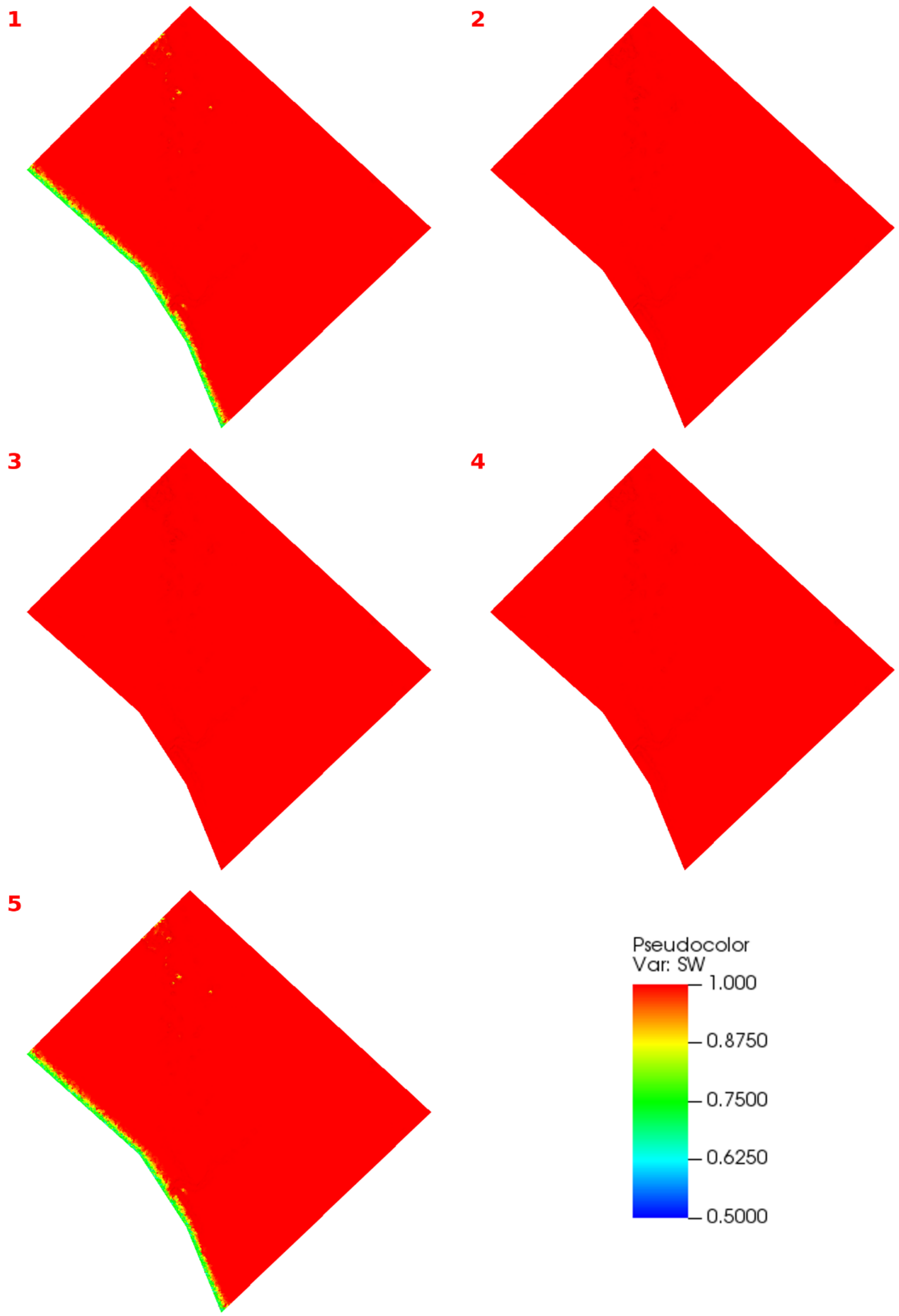

Figure 61: Case A1 - saturation distribution on the top surface of the Amira salt marsh for the selected five representative times. A sinusoidal tide is imposed.

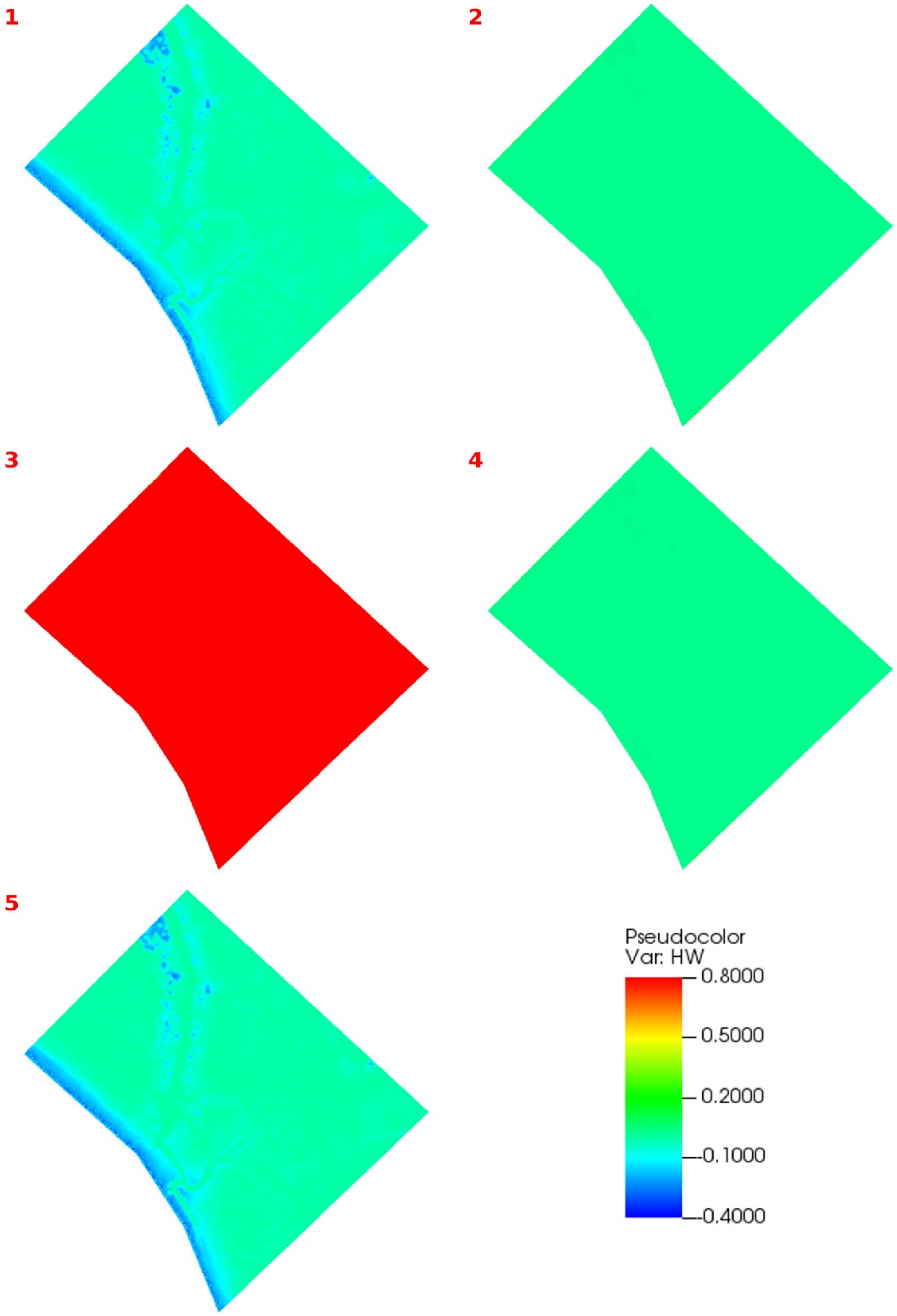

Figure 62: Case A1 - pressure head (m) distribution on the top surface of the Amira salt marsh for the selected five representative times. A sinusoidal tide is imposed.

In case A2 unsaturated conditions were mainly noticeable at the time 1 and time 5 along the lagoon marsh boundary and along the creek. However, even at time 2, $S_w < 1$ was visible in certain spots that were fully saturated case A1. Results are presented in Figure 63.

The evolution of the pressure head for A2 with the insertion of the creek led to a decrease in pressure head values within the inner part of the marsh, particularly along the creek edges (Figure 64). Initially, lower values were observed along the boundary facing the lagoon. By time 2, H_w showed higher positive values at the bottom of the creek than on the marsh platform due to the different elevation. As the tide peaked, the pressure head values across the marsh section became relatively homogeneous, with only a few more elevated areas showing lower values. By time 4, the bottom of the channel maintained its positive pressure head, while the more elevated zones did not reach the same values observed at time 2, despite having imposed the same tidal height. This behaviour reflects the system's dynamic response, indicating that the result is governed not only by the instantaneous tidal elevation but also by previous tidal conditions. At time 5, the configuration was similar to time 1.

Case A3 behave like case A2, with lower saturation values were mainly observed at the first and last timesteps. The addition of lateral creek resulted in larger unsaturated areas (Figure 65). A similar distribution was obtained in terms of H_w too, with a more evident variability in the area crossed by the creek system (Figure 66).

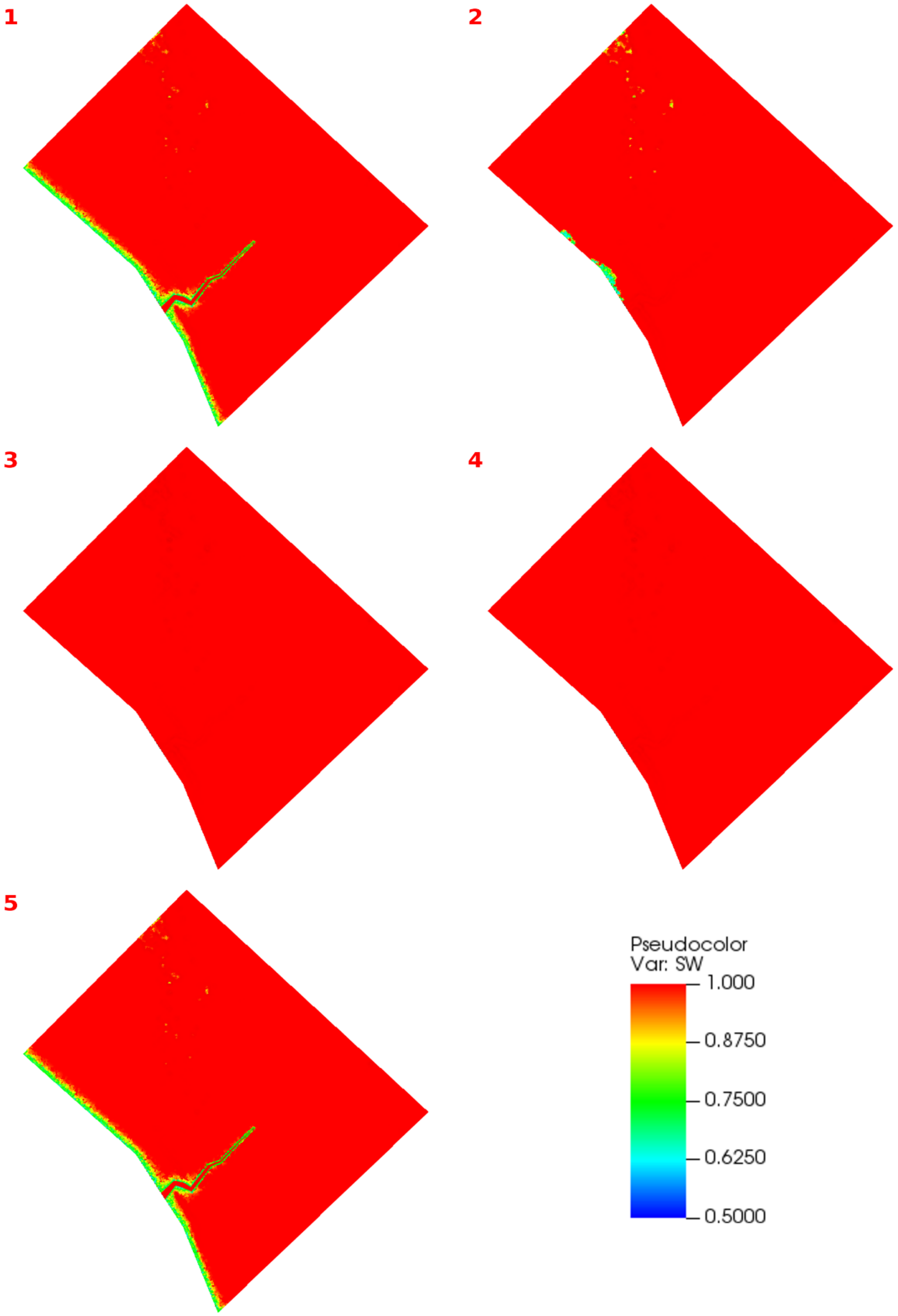

Figure 63: Case A2 - saturation distribution on the top surface of the Amira salt marsh for the selected five representative times. A sinusoidal tide is imposed.

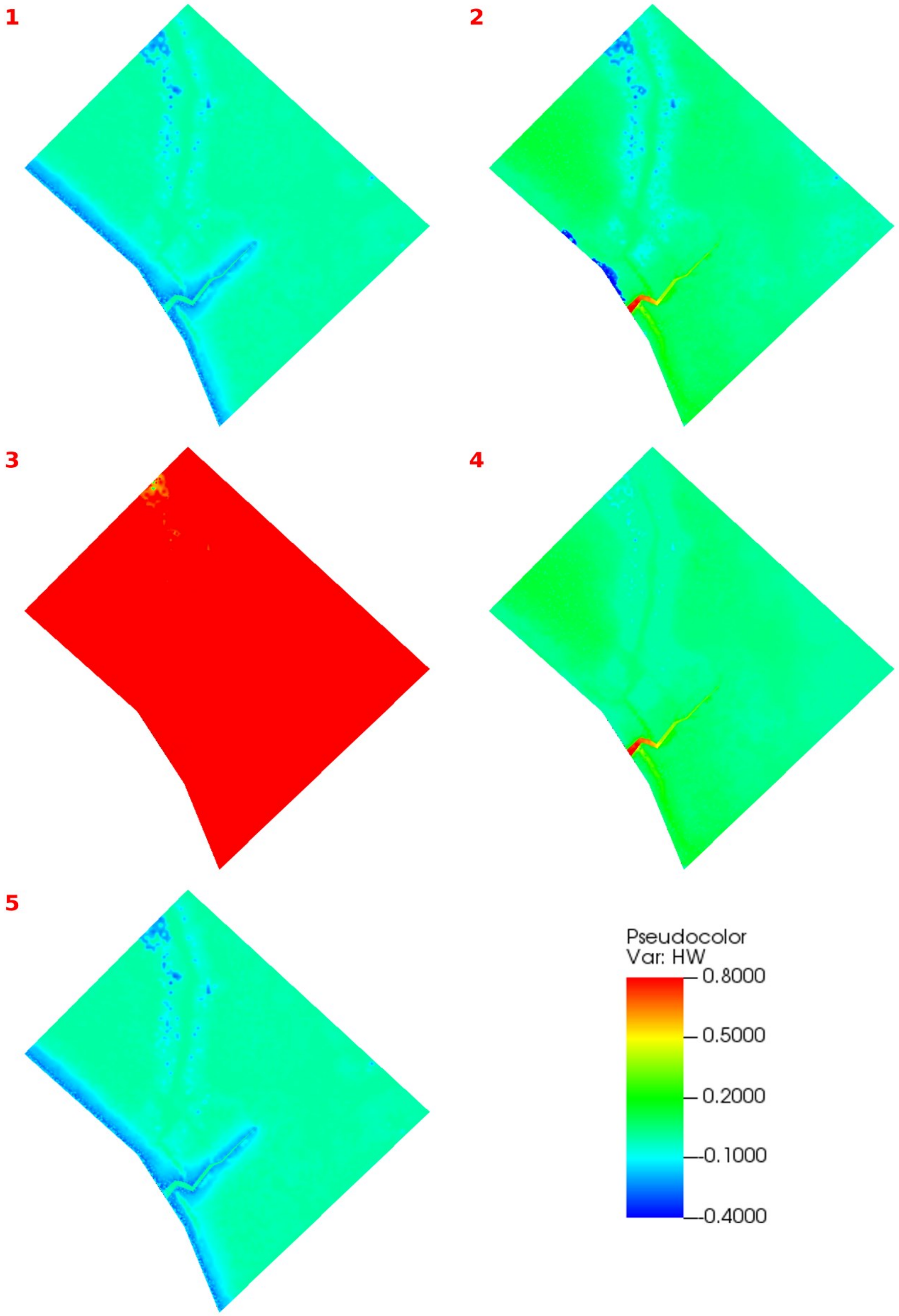

Figure 64: Case A2 - pressure head (m) distribution on the top surface of the Amira salt marsh for the selected five representative times. A sinusoidal tide is imposed.

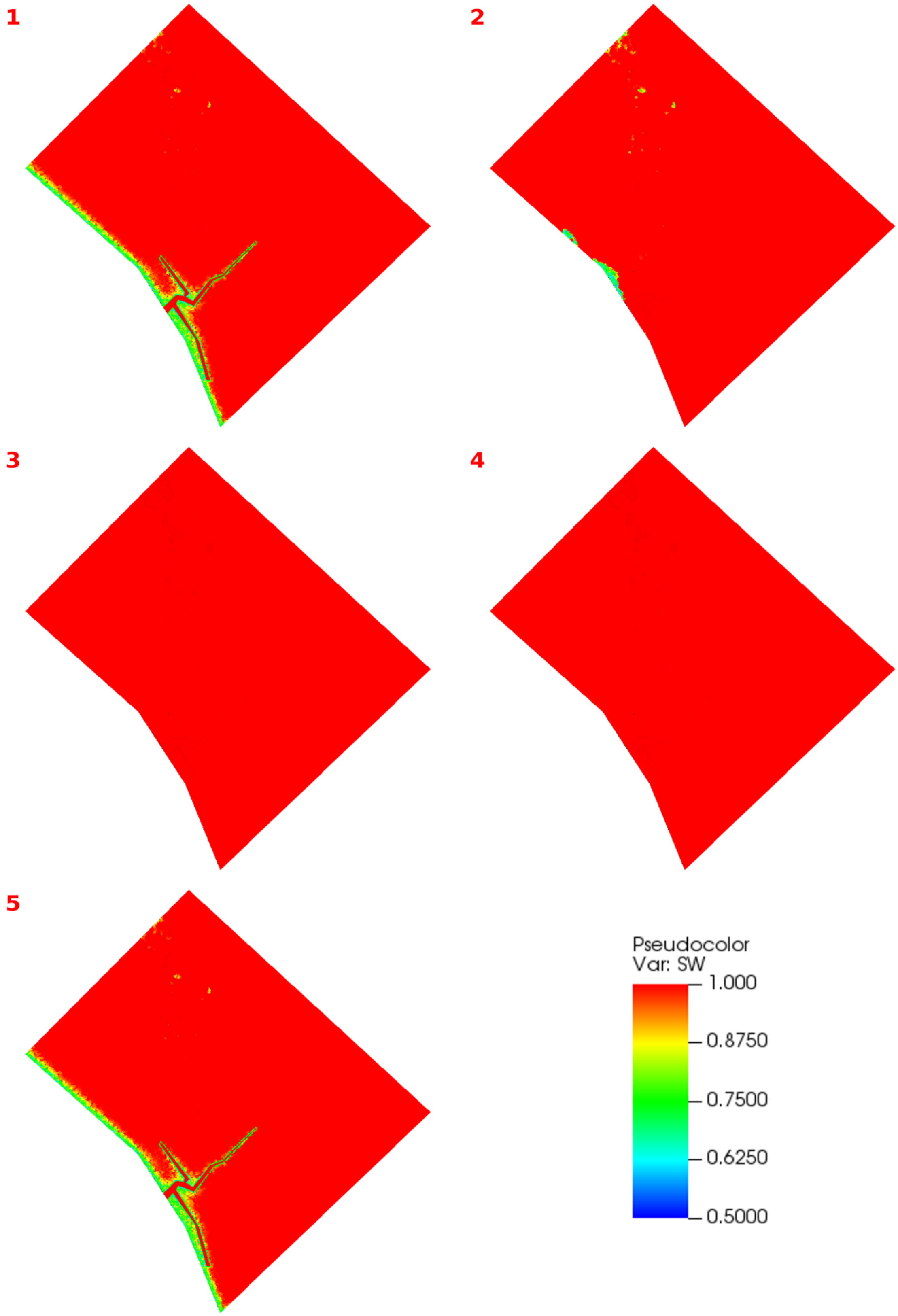

Figure 65: Case A3 - saturation distribution on the top surface of the Amira salt marsh for the selected five representative times. A sinusoidal tide is imposed.

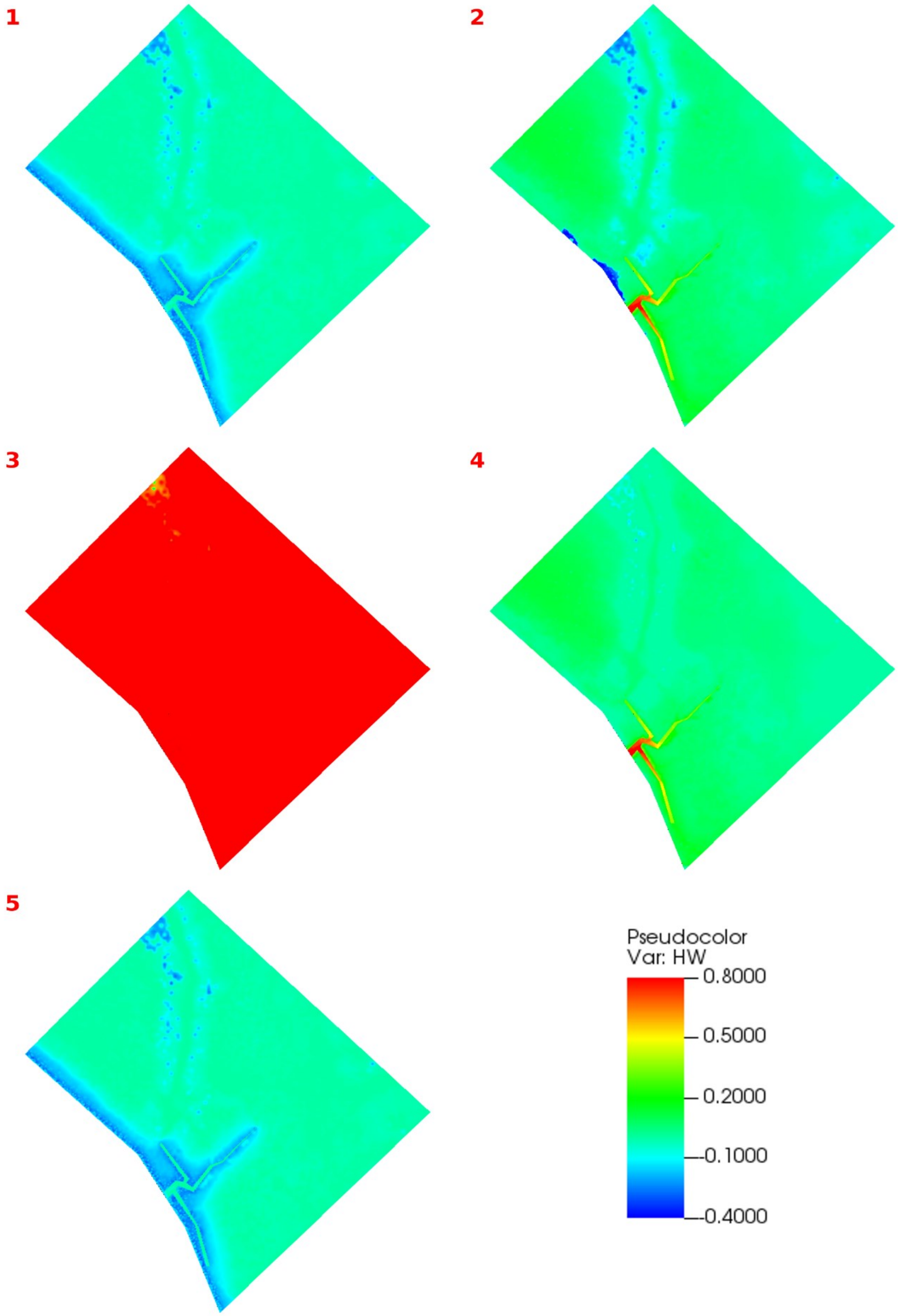

Figure 66: Case A3 - pressure head (m) distribution on the top surface of the Amira salt marsh for the selected five representative times. A sinusoidal tide is imposed.

5.4 The Amira salt marsh with a real tidal regime

A number of simulations were carried out for the Amira salt marsh considering the real tidal regime recorded by a tide gauge installed directly within the marsh. Two 72-hour simulations were conducted: one reflecting summer conditions (from 15th to 17th of July 2023) and the other representing autumn conditions (from 12th to 14th of November 2023). In the summer tide simulations, five critical times were selected for result visualization (Figure 67):

1. 16/07/2023 23:00, which corresponds to a tide hight of 0.32 m above msl;
2. 17/07/2023 02:00, which corresponds to a tide hight of 0.03 m above msl;
3. 17/07/2023 04:20, which corresponds to a tide hight of -0.36 m above msl;
4. 17/07/2023 06:40, which corresponds to a tide hight of -0.64 m above msl;
5. 17/07/2023 09:00, which corresponds to a tide hight of -0.37 m above msl.

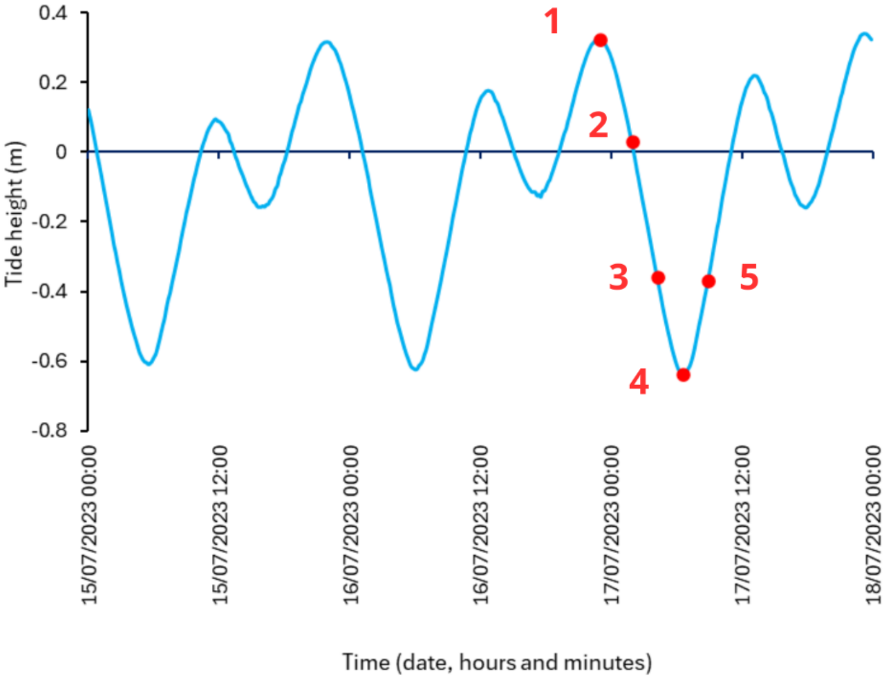

Figure 67: Tide fluctuation recorded at the Amira salt marsh from 15th to 17th of July 2023 and applied in the simulations. The five selected times for result visualisation are highlighted in red.

The previous three configurations, i.e. case A1, case A2, and case A3, were investigated. In case A1 (Figure 68), the saturation remained constant and equal to 1 in correspondence of the first two times. It gently change only at time 3, where an unsaturated zone emerged along the marsh boundary facing the lagoon. This unsaturated area enlarged in time 4 and time 5 when the highest elevated zones in the northern part of the marsh started to experience $S_w < 1$. Although time 2 and time 5 were characterized by a very similar tide height, the previous behaviour of the tidal oscillation impacted differently the saturation values at the two steps, showing causing a gently different S_w distribution on the marsh platform.

As for the pressure head for A1, it initially exhibited positive values that began to decline as the tide lowered. Starting from the time 3, the difference in elevation throughout the top of the marsh became more evident, resulting in a detailed green-blue variation in many areas of the marsh. By the last time the highest portions of the marsh located to the north, as well as some areas near the marsh boundary displayed low pressure head values, reaching $H_w = -0.4$ m (Figure 69).

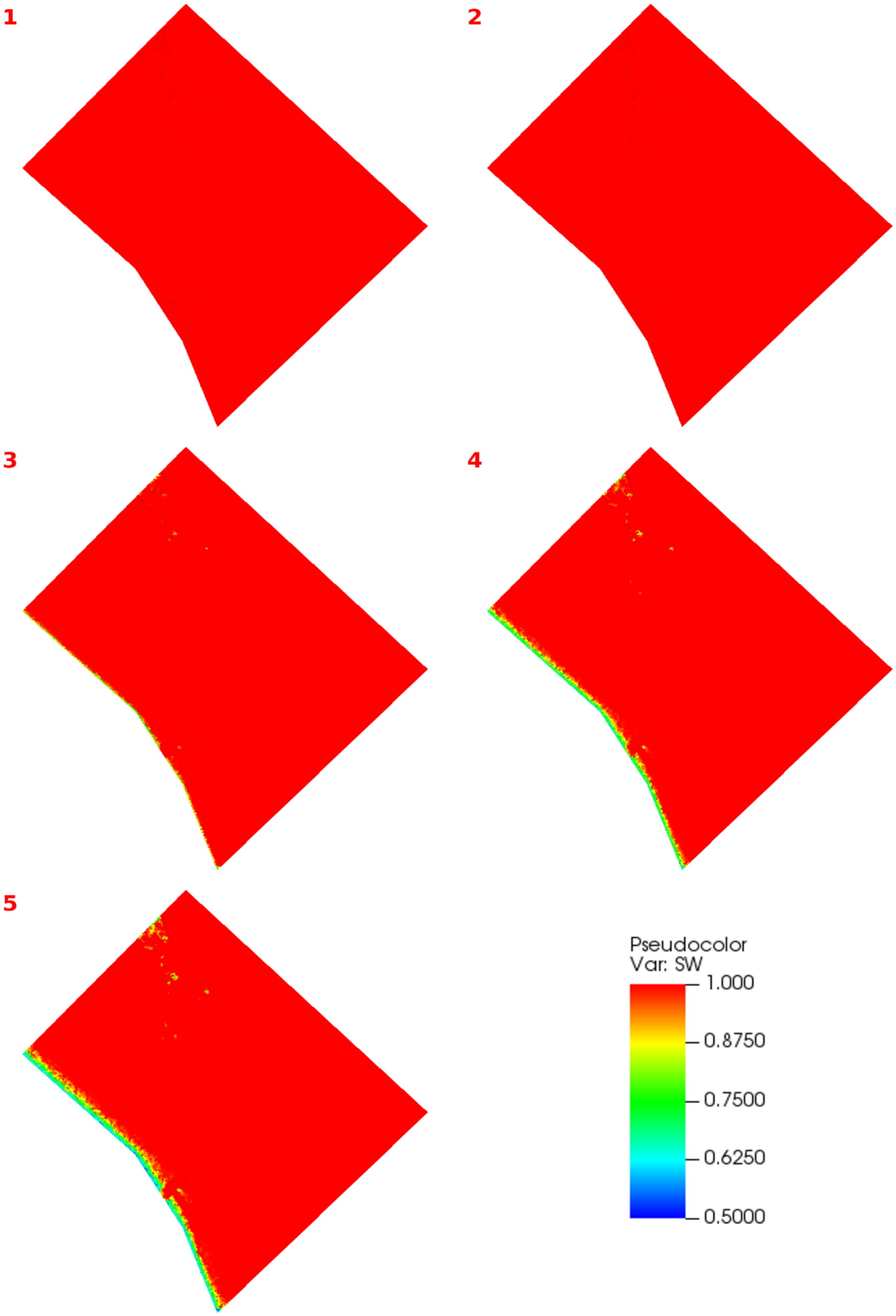

Figure 68: Case A1 - saturation distribution on the top surface of the Amira salt marsh for the selected five representative times. The summer tide from July 15th to 17th 2023 was applied.

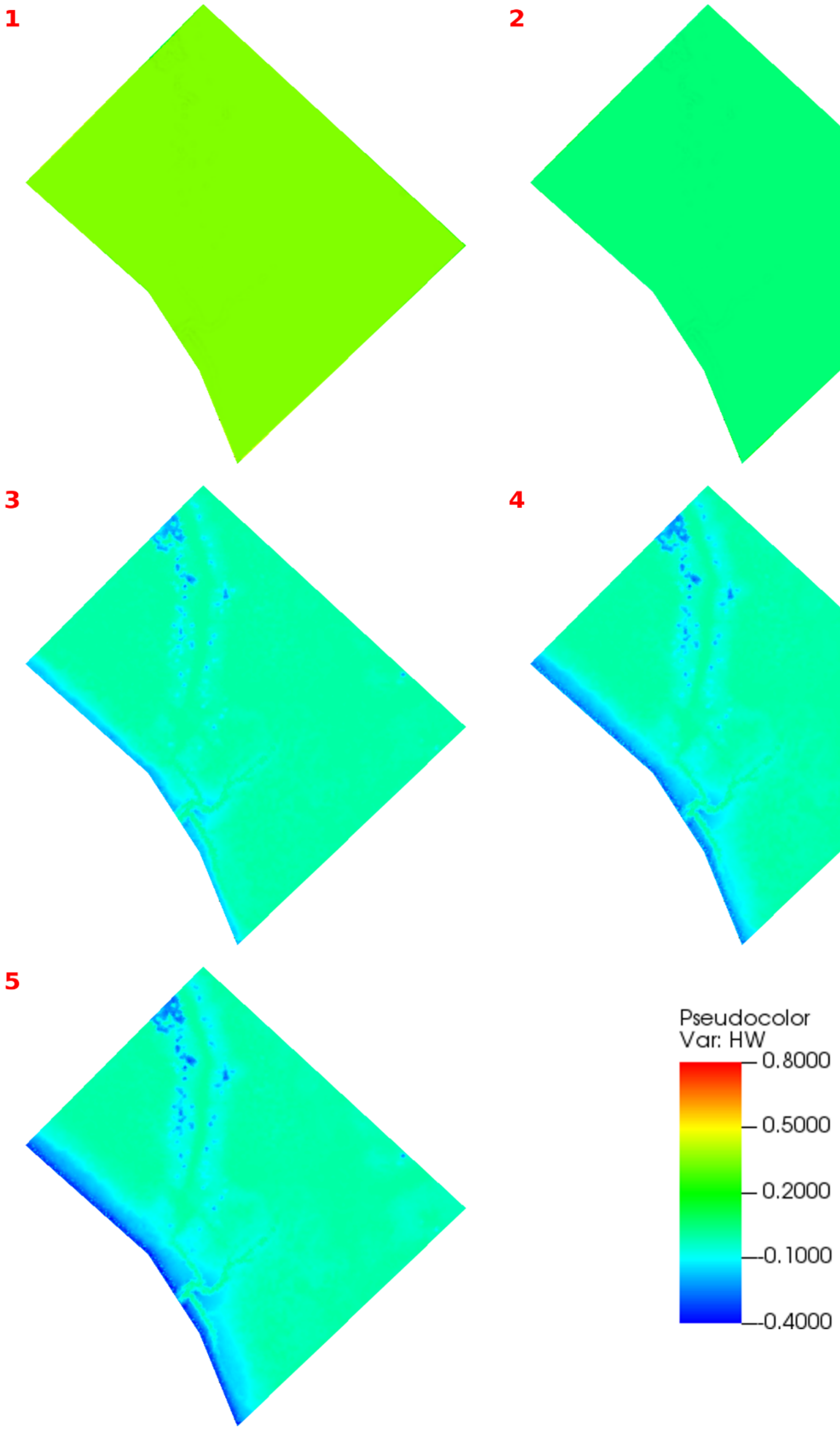

Figure 69: Case A1 - saturation distribution on the top surface of the Amira salt marsh for the selected five representative times. summer tide from July 15th to 17th 2023 was applied.

In case A2 (Figure 70) the general behaviour of the model outcomes was quite similar to the previous case. However, the presence of the tidal creek facilitated drainage in the inner parts of the marsh along the creek trace, whereas in case A1 only a limited number of areas within the marsh exhibited unsaturated zones.

The pressure head for A2, on the other hand, showed a quite different behaviour in the values distribution since the beginning (Figure 71). Previously, the marsh displayed relatively homogeneous H_w values across its surface, while the introduction of the creek enabled a variation that reflected the differences in the top elevation. As the tide began to fall, generally lower values were observed, particularly along the creek path, in the northern more elevated zones, and in the area nearby the marsh boundary more affected to tide fluctuations.

Lastly, in case A3 further drainage was facilitated in the inner parts of the marsh (Figure 72). Similar to case A2, the presence of a more complex creep network caused a more variable H_w distribution (Figure 73).

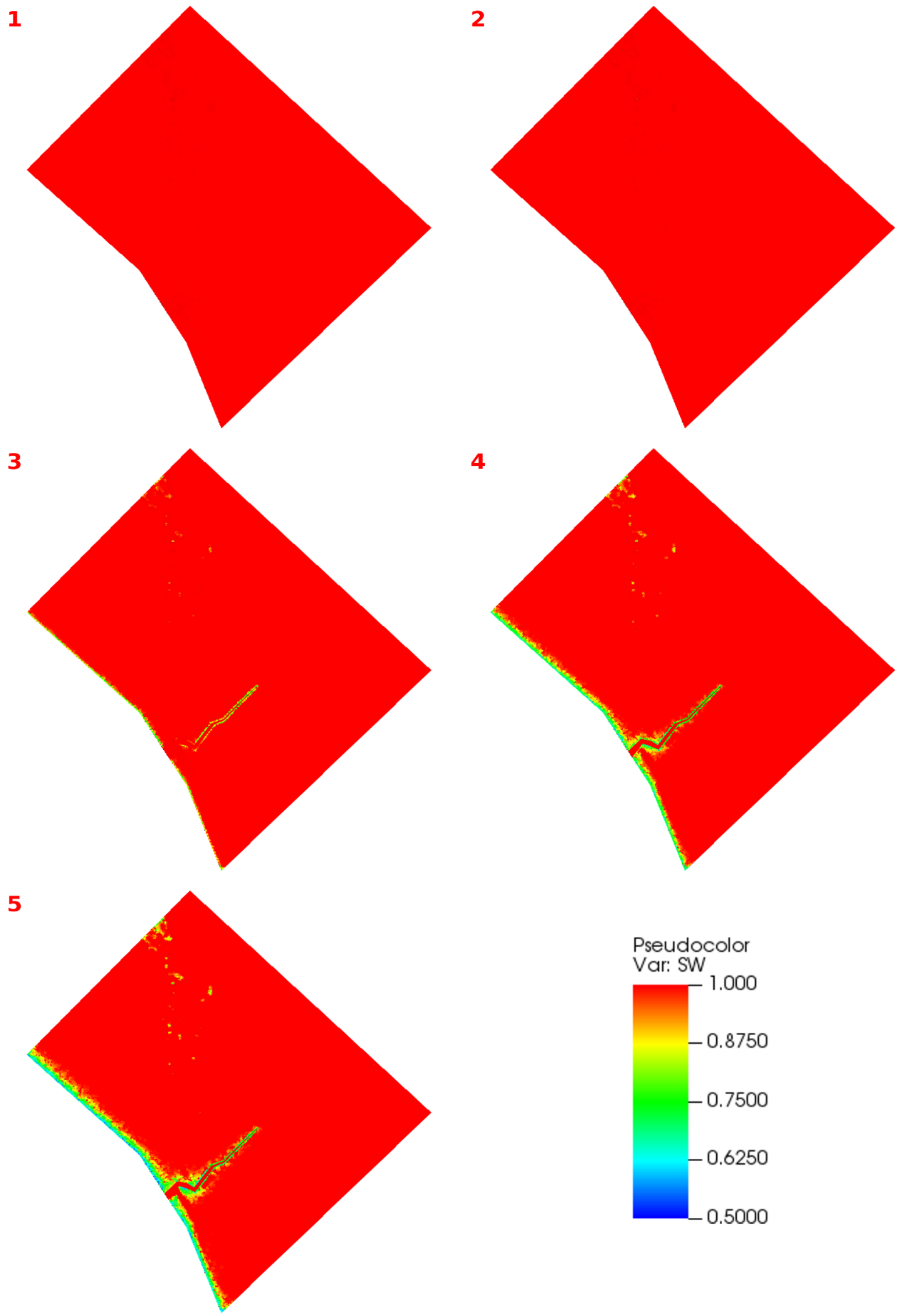

Figure 70: Case A2 - saturation distribution on the top surface of the Amira salt marsh for the selected five representative times. The summer tide from July 15th to 17th 2023 was applied.

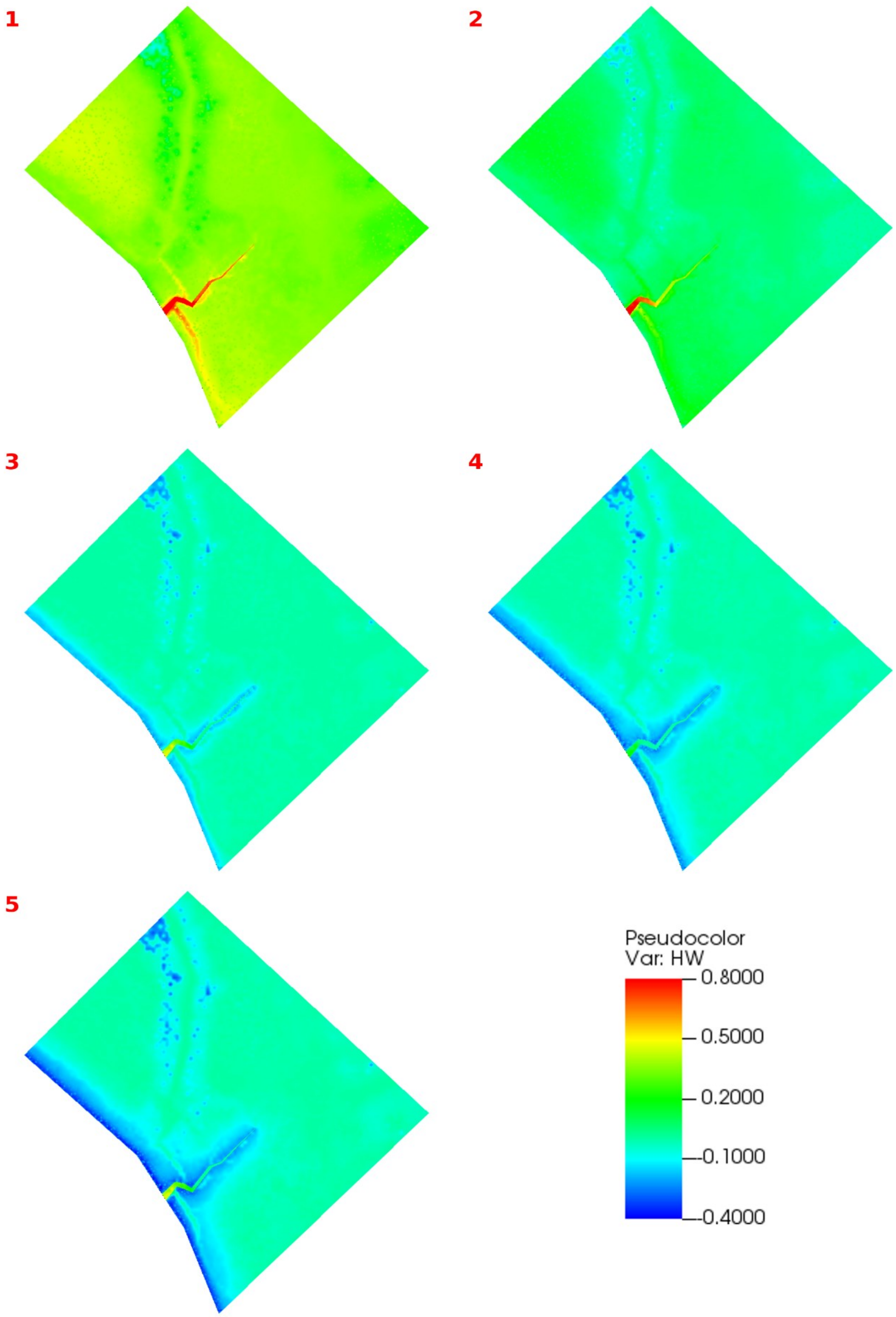

Figure 71: Case A2 – pressure head (m) distribution on the top surface of the Amira salt marsh for the selected five representative times. The summer tide from 15th to 17th July 2023 was applied.

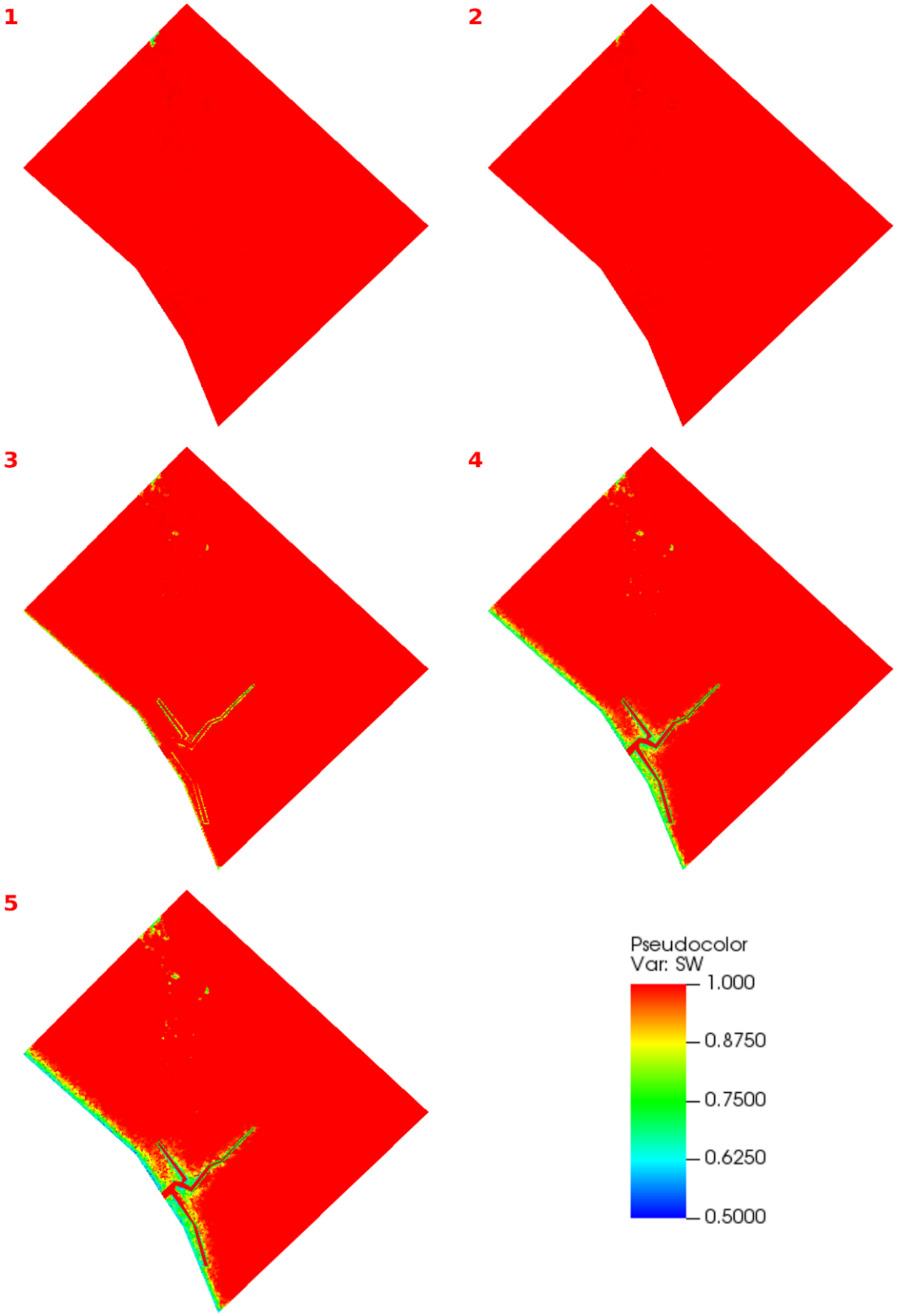

Figure 72: Case A3 - saturation distribution on the top surface of the Amira salt marsh for the selected five representative times. The summer tide from 15th to 17th July 2023 was applied.

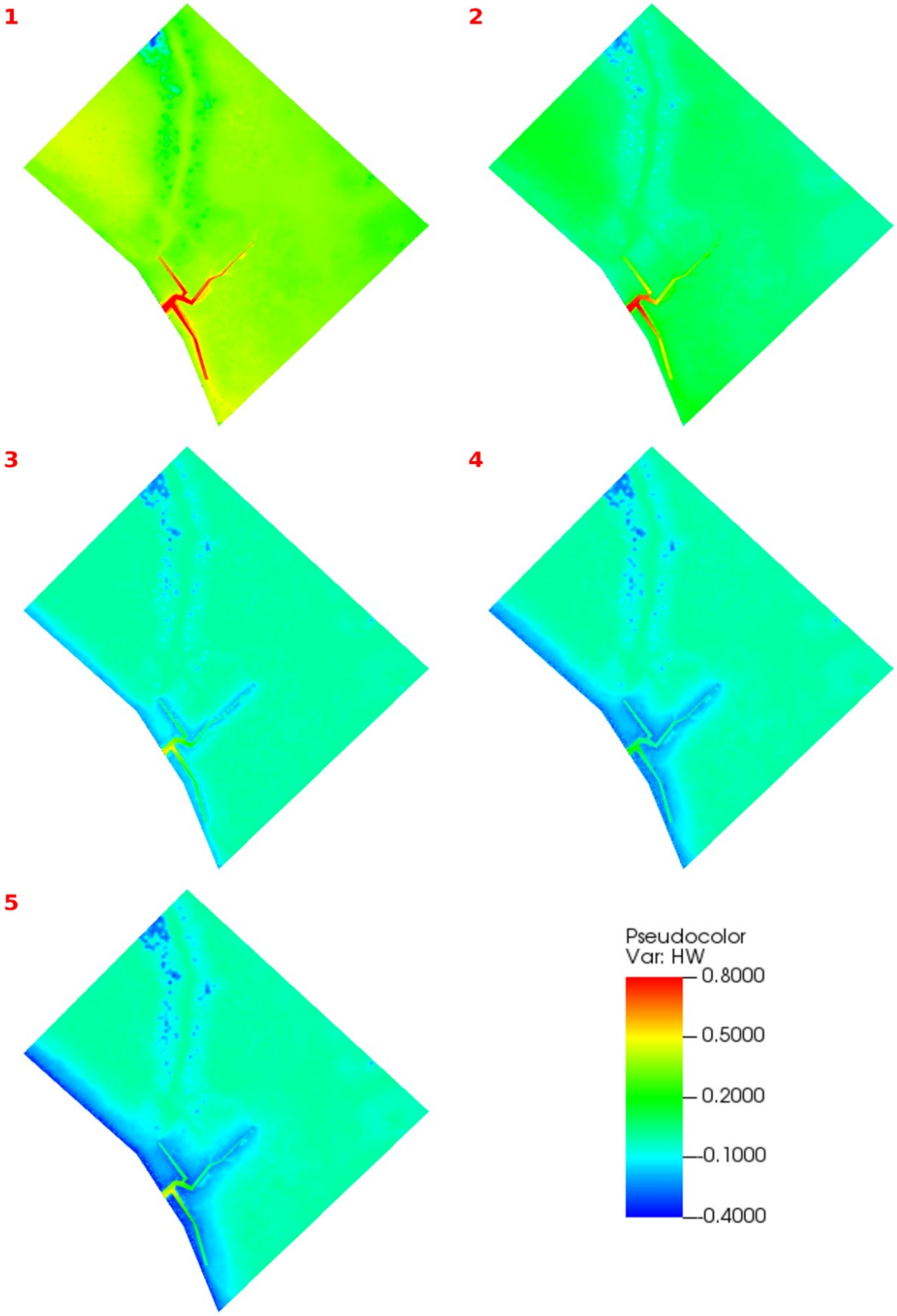

Figure 73: Case A3 – pressure head (m) distribution on the top surface of the Amira salt marsh for the selected five representative times. The summer tide from 15th to 17th July 2023 was applied.

As in the previous cases, the saturation evolution over time was compared across the three configurations at a location near the creek edge, as shown in Figure 74.

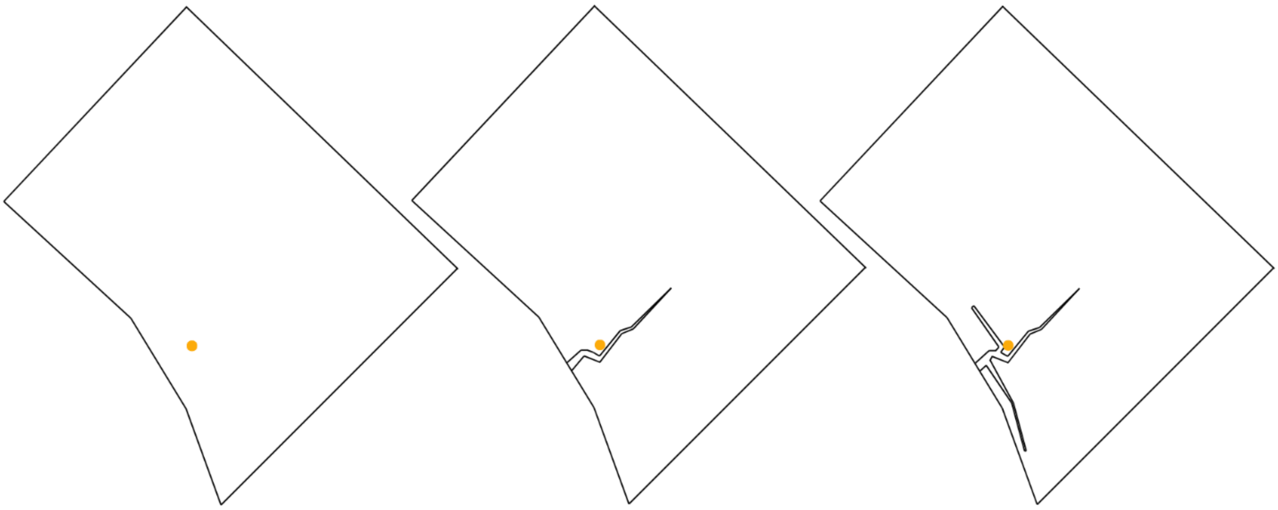

Figure 74: Location selected for the comparison of saturation evolution over time for the Amira salt marsh.

S_w at the selected point remained equal to 1 throughout the entire simulated period in case A1. In contrast, with the other two configurations, the presence of the creek network yielded lower saturation values (Figure 75). For case A2, the minimum saturation recorded was 0.76, whereas in case A3 reached a minimum of 0.56. These results further highlight that saturation evolution is highly dependent on the creek network and the selected location relative to the creek network. As shown in Figure 76, saturation in case A3 remained lower than 1 for a longer period, approximately 40 minutes, than in case A2. This time corresponds to approximately 10 % of the time interval where the portion of the salt marsh remained unsaturated.

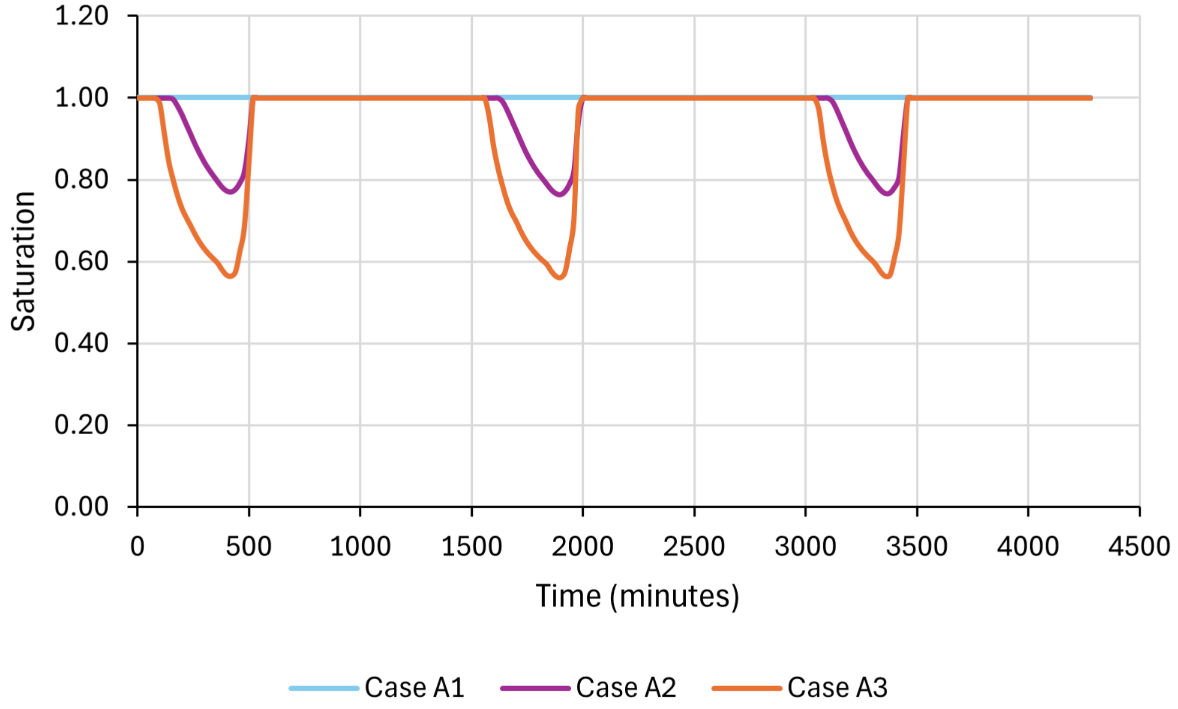

Figure 75: Saturation over time at the selected location in the Amira salt marsh with the tide fluctuation recorded from 15th to 17th of July 2023.

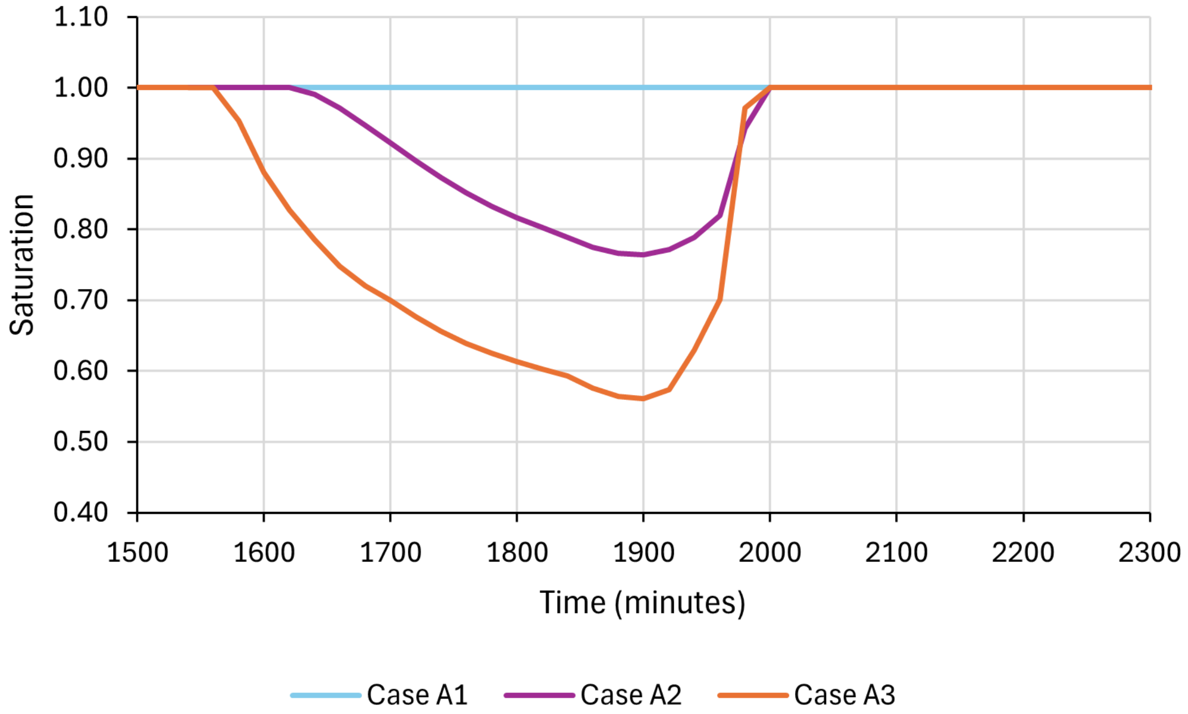

Figure 76: Saturation over time at the selected point in the Amira salt marsh caused by one high tide cycle recorded between 15th and 17th July 2023-.

A similar analysis was carried out for the tide fluctuations recorded in Autumn, between November 12 and 14, 2023. Five critical times were selected for result visualization (Figure 77). These times were chosen to capture the highest peak of the autumn dataset, a low point, and a few intermediate stages, providing a representative overview of the tidal behaviour:

1. 12/11/2023 11:00, which corresponds to a tide hight of 0.63 m above msl;
2. 13/11/2023 15:00, which corresponds to a tide hight of 0.01 m above msl;
3. 13/11/2023 16:20, which corresponds to a tide hight of -0.24 m above msl;
4. 13/11/2023 18:20, which corresponds to a tide hight of -0.51 m above msl;
5. 13/11/2023 20:20, which corresponds to a tide hight of -0.27 m above msl.

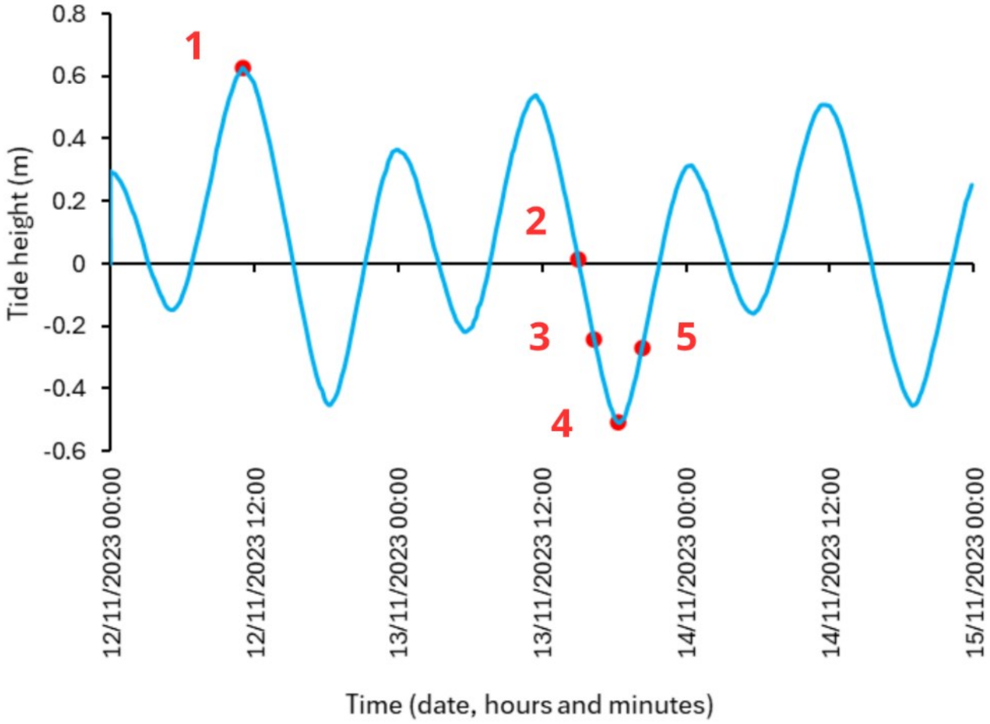

Figure 77: Tide fluctuation recorded at the Amira salt marsh from 12th to 14th of November, 2023, and applied in the simulations. The five selected times for result visualisation are highlighted in red.

The results obtained by the GWS were similar to the cases run with the summer tide evolution (Figure 78 - Figure 83). However, as the tide reached a higher peak than that of the summer tide, with a hight of 0.63 m above msl, the pressure head registered higher values compared to the summer analyses.

The results from the different configurations clearly demonstrated that the introduction of tidal creeks significantly improved drainage in the inner zones of the marsh, which would otherwise remain saturated under flat terrain conditions. The results showed a significant variability particularly in the northern part of the marsh, where areas with higher elevations were present, and along the edge exposed to tidal fluctuations. This outcome has direct ecological implications, as improved drainage can foster more favourable conditions for vegetation colonization and growth.

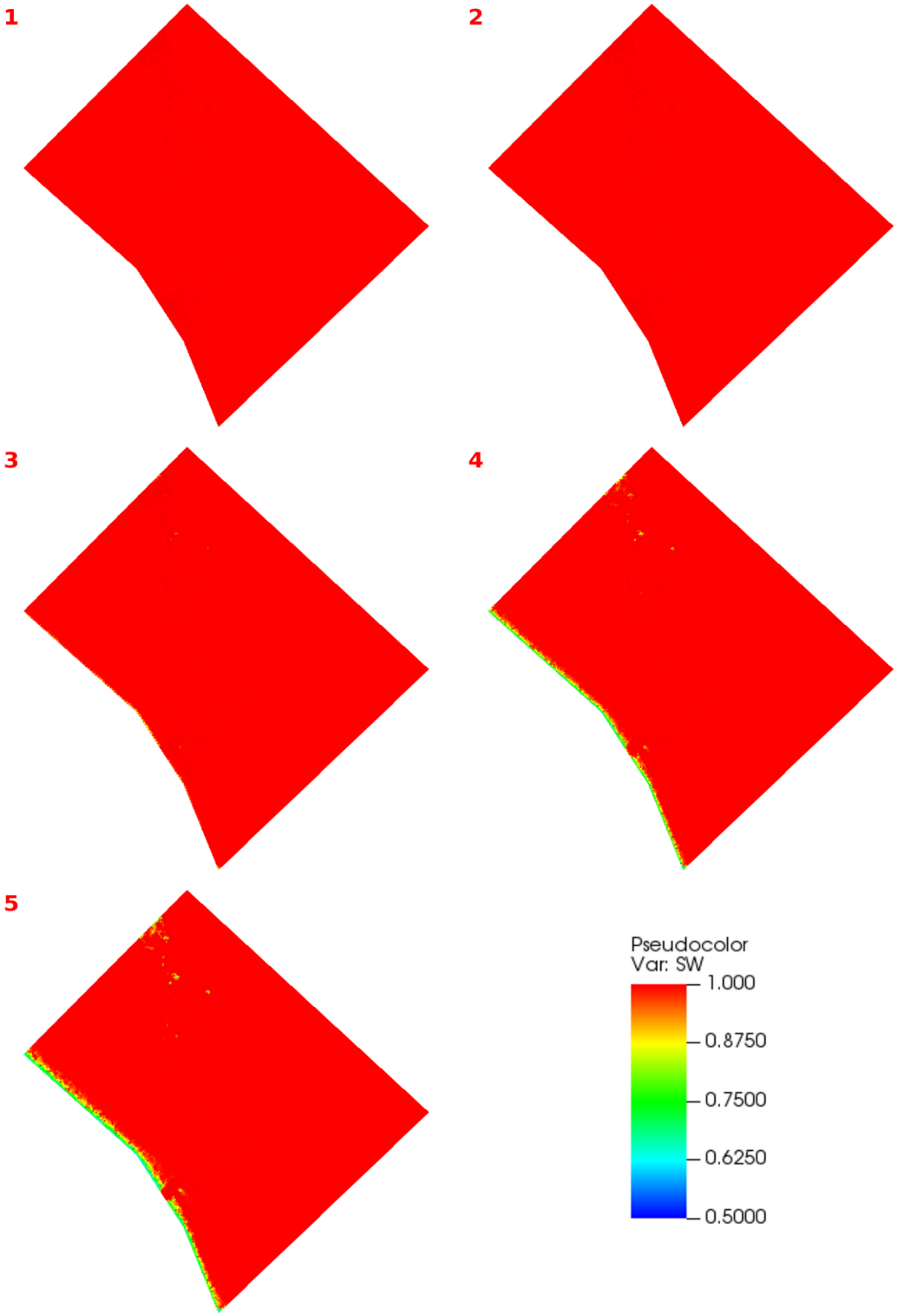

Figure 78: Case A1 - saturation distribution on the top surface of the Amira salt marsh for the selected five representative times. The autumn tide from November 12th to 14th 2023 was applied.

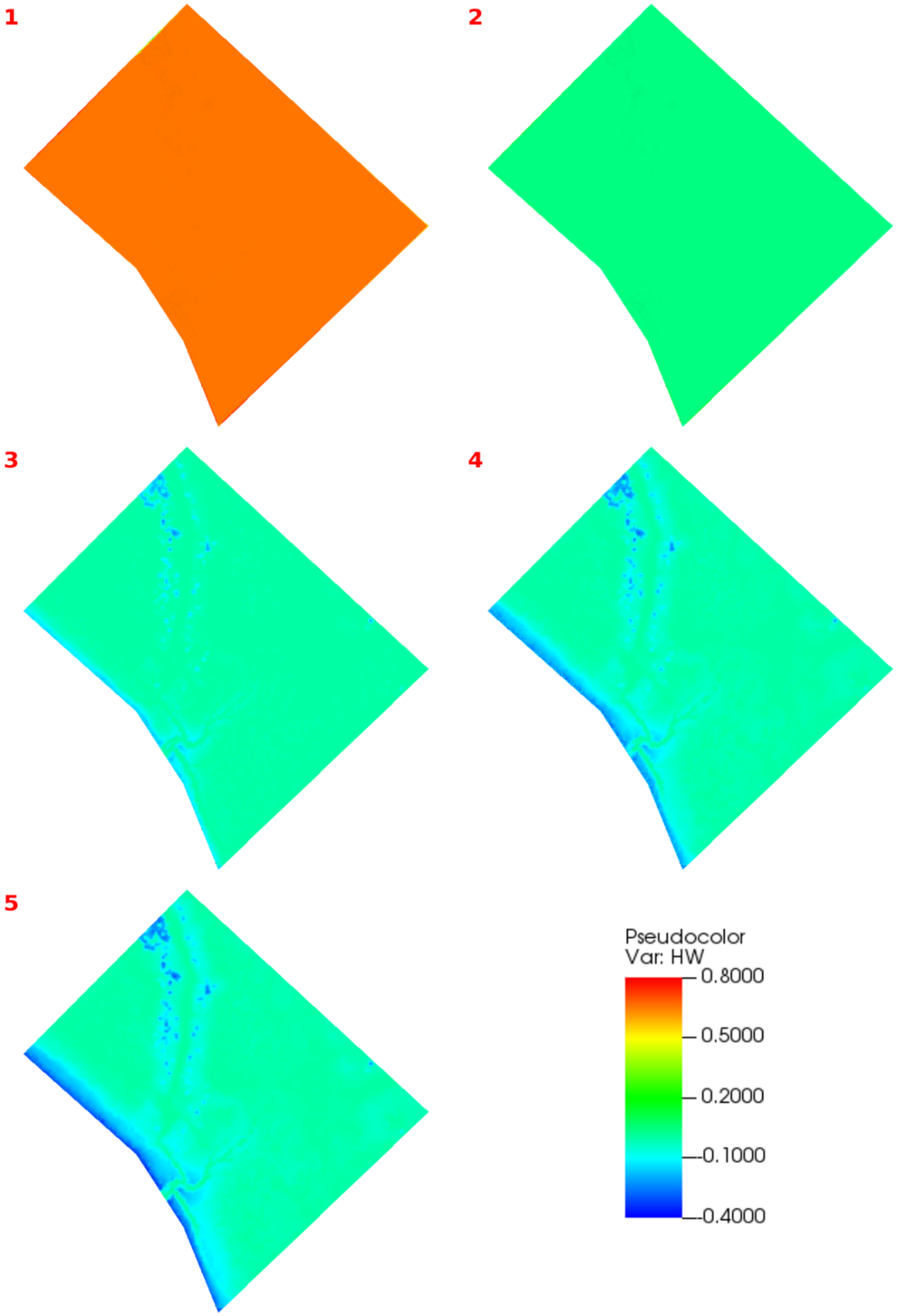

Figure 79: Case A1 - pressure head (m) distribution on the top surface of the Amira salt marsh for the selected five representative times. The autumn tide from November 12th to 14th 2023 was applied.

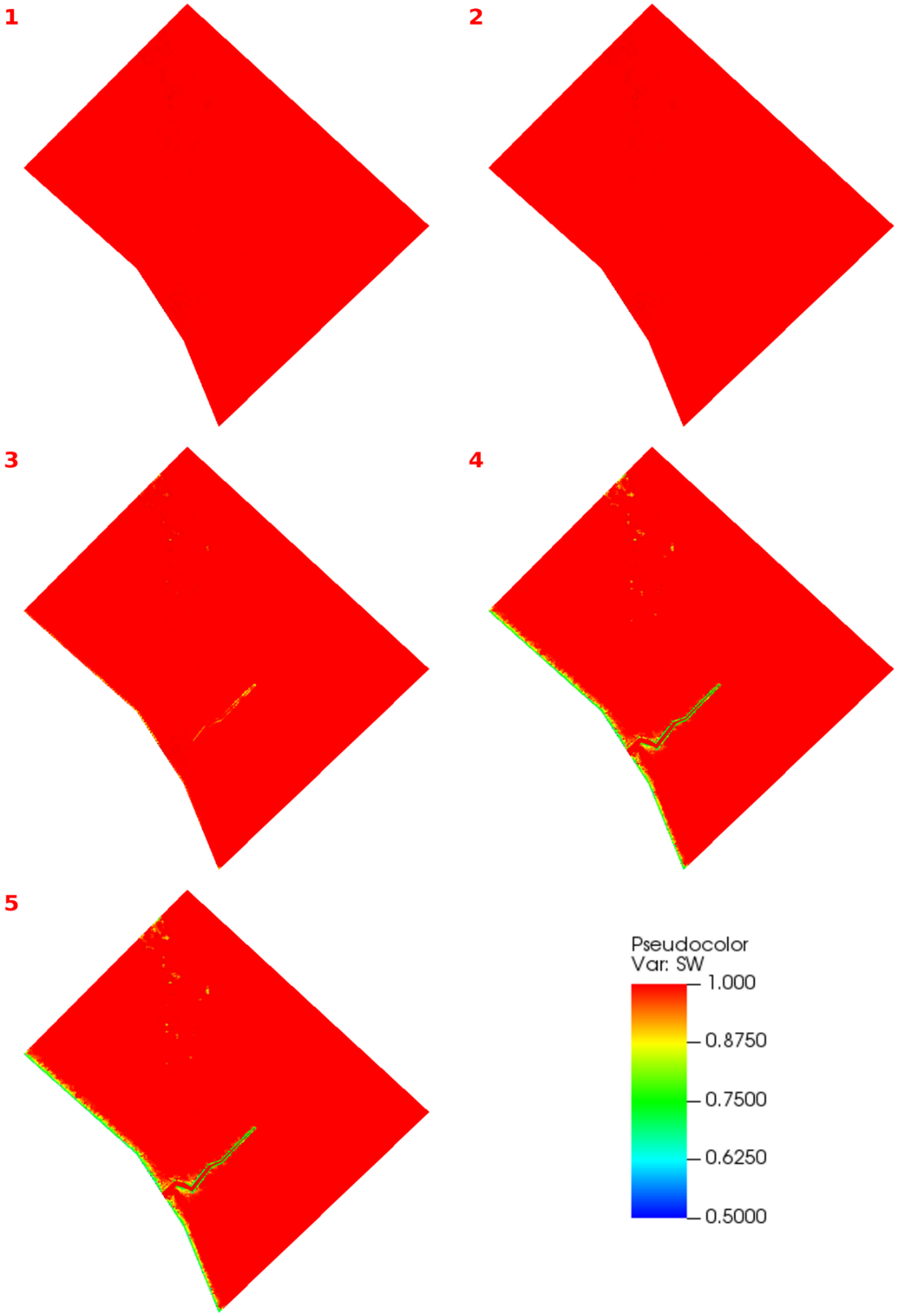

Figure 80: Case A2 - saturation distribution on the top surface of the Amira salt marsh for the selected five representative times. The autumn tide from November 12th to 14th 2023 was applied.

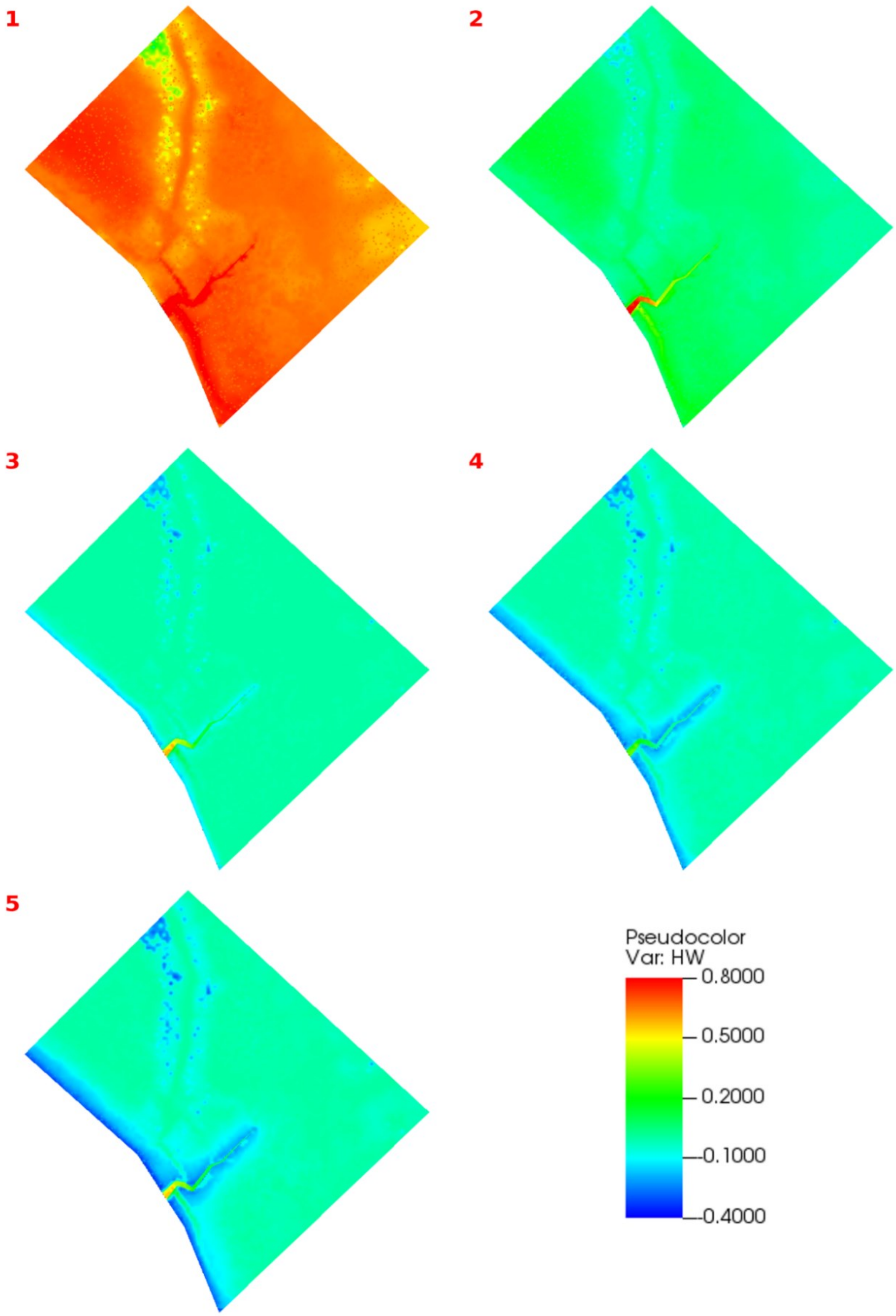

Figure 81: Case A2 – pressure head (m) distribution on the top surface of the Amira salt marsh for the selected five representative times. The autumn tide from November 12th to 14th 2023 was applied.

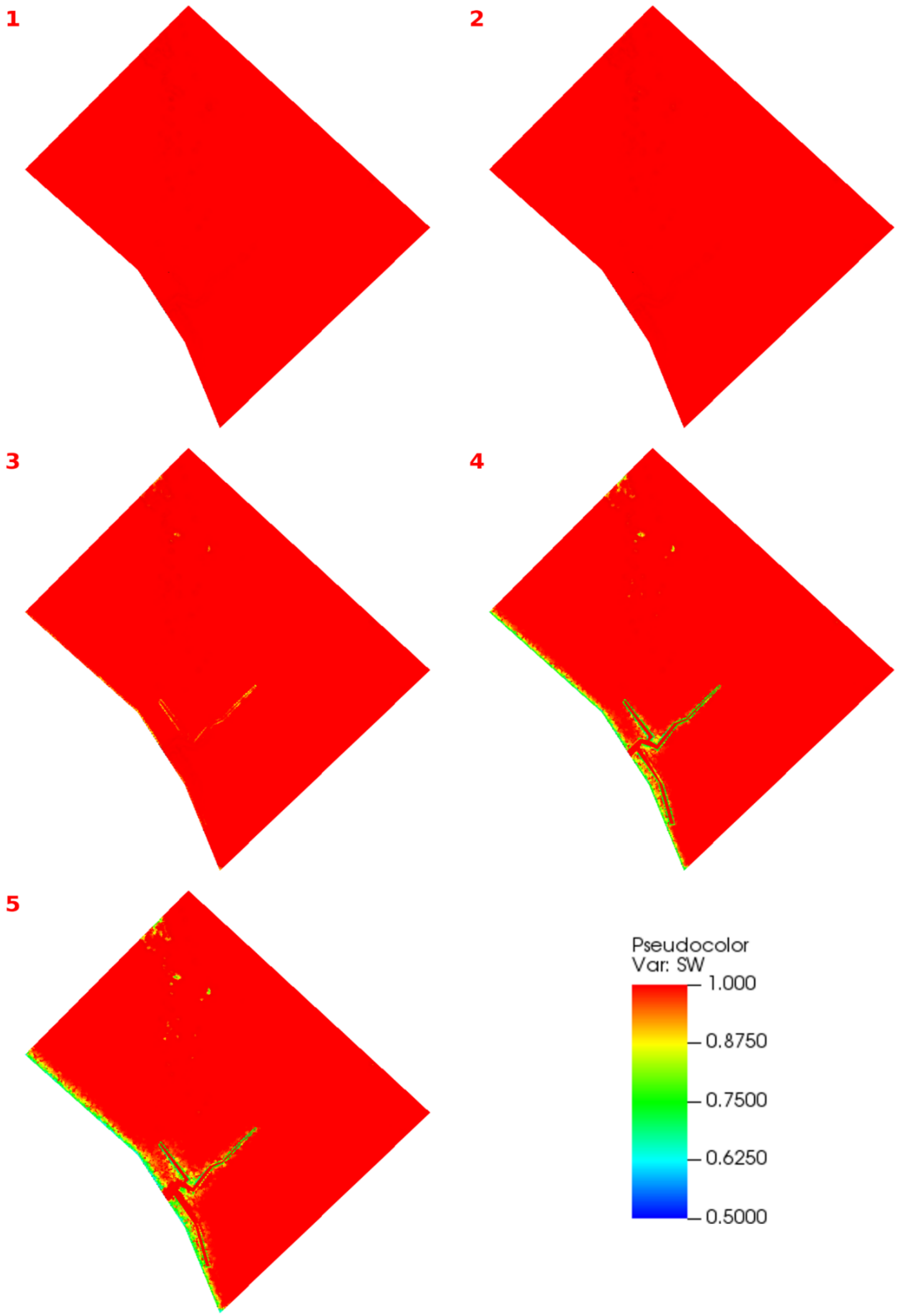

Figure 82: Case A3 - saturation distribution on the top surface of the Amira salt marsh for the selected five representative times. The autumn tide from November 12th to 14th 2023 was applied.

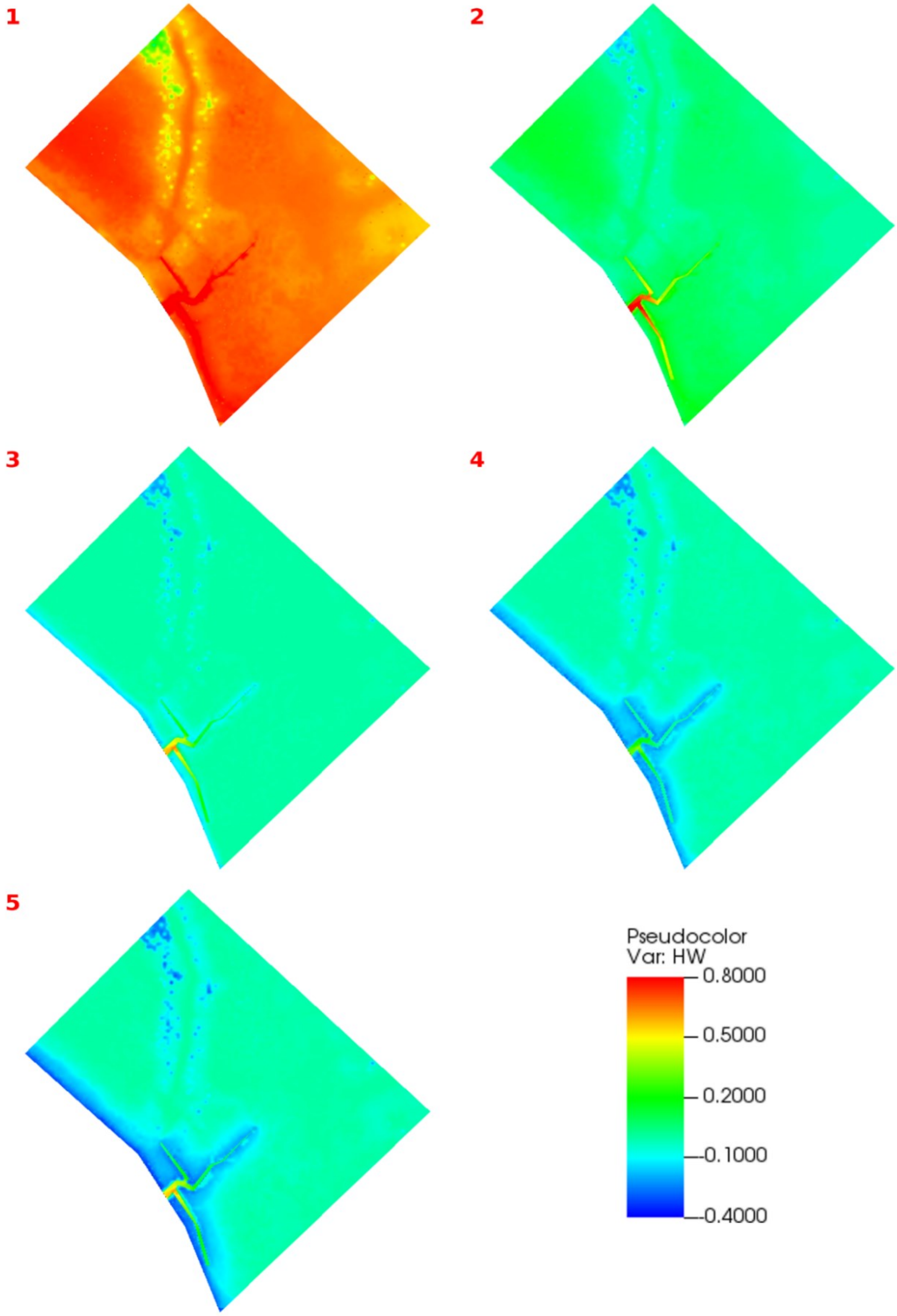

Figure 83: Case A3 – pressure head (m) distribution on the top surface of the Amira salt marsh for the selected five representative times. The autumn tide from November 12th to 14th 2023 was applied.

5.5 Saturation variability and model sensitivity analysis

Further analyses were carried out on the Amira salt marsh using the summer tide data, as the summer tide reached the lowest height value (-0.64 m above msl), making it the most interesting for investigating drainage processes. The study focused on several key aspects to enhance the understanding of the system dynamics:

- First, the volume of elements with a saturation degree between 0 and 0.99 was calculated for each timestep, allowing for a detailed assessment of temporal variations in water content.
- Second, the influence of mesh refinement was evaluated to determine its impact on the accuracy of the results.
- Finally, the effect of hydraulic conductivity on the model response was examined, providing insights on how soil permeability governs water flow and saturation patterns.

Together, these investigations offer a more comprehensive picture of the hydrodynamic behaviour of the salt marsh under low-tide conditions.

5.5.1 Unsaturated marsh volume

The analysis began with the calculation of the cumulative volume of the finite elements characterized by a saturation degree lower than 1 at each timestep. This was carried out using the isovolume post-processing feature in VisIt. Isovolumes allow the extraction and visualization of regions of the mesh that share a common range of values for a given variable, in this case the degree of saturation. By isolating only those elements within the defined saturation interval, it was possible to quantify the volumetric temporal evolution of the partially saturated zone within the model domain, offering valuable insights into drainage processes and dynamics under summer tide conditions. The volume was computed for the three mesh configurations (case A1, case A2, and case A3), to investigate how the presence of channels affects the development of unsaturated zones within the domain and to delineate the resulting area of influence. Results are presented in Figure 84.

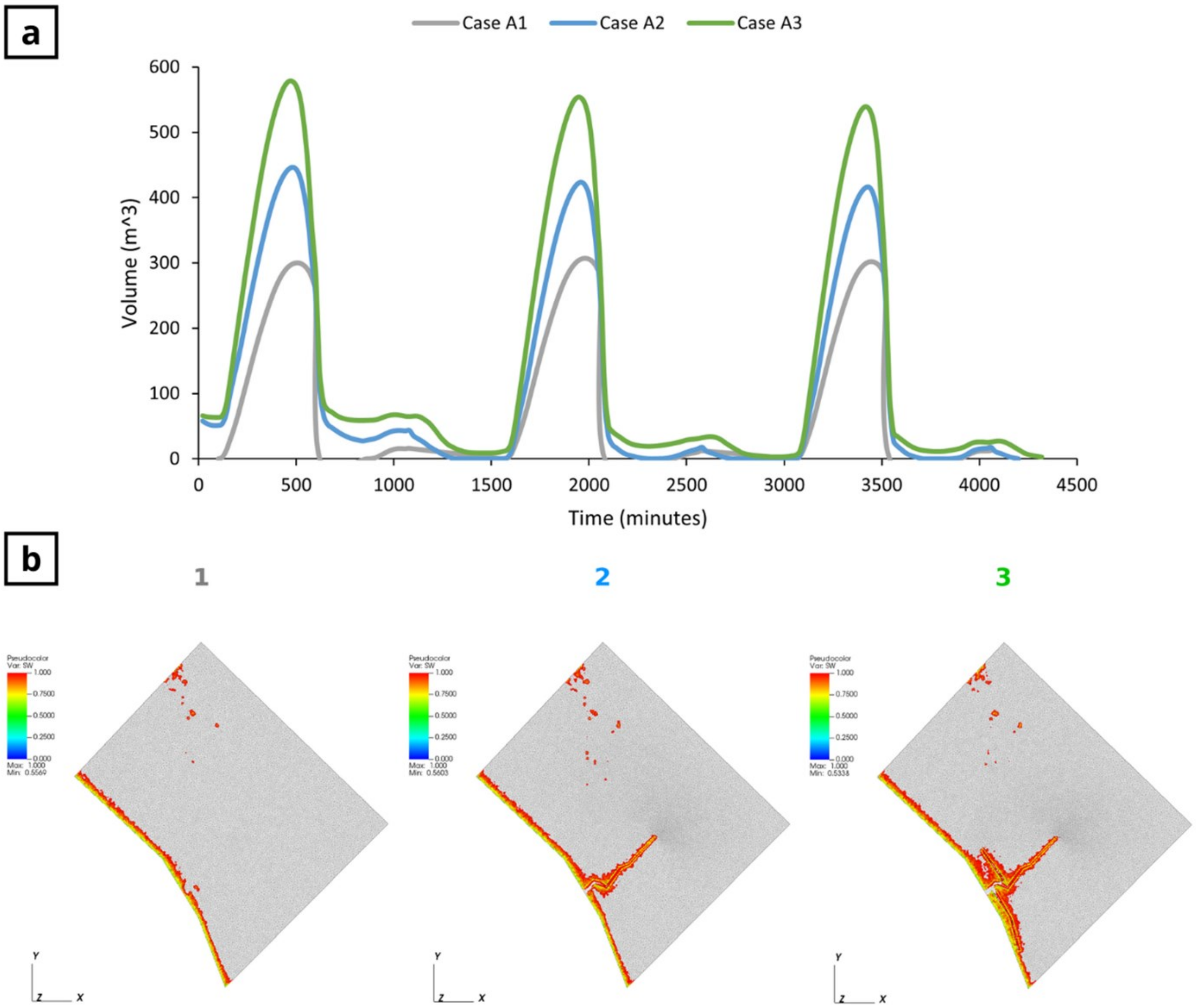

Figure 84: a) Temporal evolution of the volume of elements exhibiting a saturation degree between 0 and 0.99 at each timestep. b) Isovolumes visualisation at the timestep corresponding to the lowest summer tide level. Plot 1 refers to case A1, plot 2 to case A2, and plot 3 to case A3.

As expected, case A1 exhibited the lowest unsaturated volume values compared to the other two cases. Its maximum volume reached 307.3 m^3, whereas in case A2 peaked at 446.5 m^3 and in case A3 reached 578.2 m^3. Despite these differences, the overall temporal trends were quite similar across the three scenarios, each displaying three distinct peaks over the simulation period corresponding to the minimum tide level.

The visualization of the isovolumes at the timestep corresponding to the lowest summer tide clearly highlighted the distribution of the unsaturated zones within the marsh. In all three cases, the marsh side at the lagoon boundary consistently exhibited unsaturated conditions, along with some of the northern most elevated portions of the marsh. Moreover, the inclusion of the tidal creek network had a critical effect: even the inner portions of the marsh, previously less affected, experienced significant desaturation. In particular, the complex creek network characterizing case A3 amplified this effect, facilitating water drainage and expanding the area influenced by lower saturation levels.

Overall, this comparative analysis demonstrates that the presence and geometry of tidal creek crossing the salt marsh play a critical role in controlling desaturation dynamics within the marsh. Tidal creeks not only increase the marsh volume in partially saturated condition but also extends this condition in inner marsh portions.

5.5.2 Mesh refinment

Further analysis was carried out to assess the sensitivity of the model to spatial resolution, focusing on case A3. The mesh used for all the simulations described till this point had a dimensionless characteristic element length (lc) equal to 1, which was divided by 2 on the top surface points, providing an increased resolution near the surface and around the creek system. To evaluate the impact of the mesh resolution on the results, a new, finer mesh was generated. In this refined mesh, the characteristic element length was set to 0.4, with $lc/2$ applied to the same top-surface points as before. Overall, the baseline mesh consisted of 76,887 nodes, while the number of nodes in the refined mesh increased to 659,893. This allowed for a more detailed representation of the domain and a more accurate computation of pressure head and saturation degree evolution over time and space. The impact on mesh resolution is visualised in Figure 85. Mesh refinement allowed for a more detailed representation of the variable (S_w and H_w) distribution within the marsh landform. Panels (b) and (f) highlight the smoother variability of the saturation degree. Additionally, while the sides of the channel were previously represented by a single element, the refined mesh was able to includes two elements along the vertical direction, making it clearer that desaturation occurs primarily in the upper portion of the channel.

The volume of elements with a saturation degree between 0 and 0.99 was also calculated at each timestep with the refined mesh and compared with the value obtained for the baseline mesh (Figure 86). A smaller value was obtained with the former, reaching only 417.8 m^3, less than 150 m^3 than the latter. This is probably due to the fact that, as saturation is calculated at the centroid of each element, thicker elements in the coarser mesh appear desaturated, representing a greater portion of the domain compared to the finer mesh. The width of unsaturated zone around the tidal creeks appears larger with the finer than the coarser mesh, ranging from around 1 m to up to 3 m.

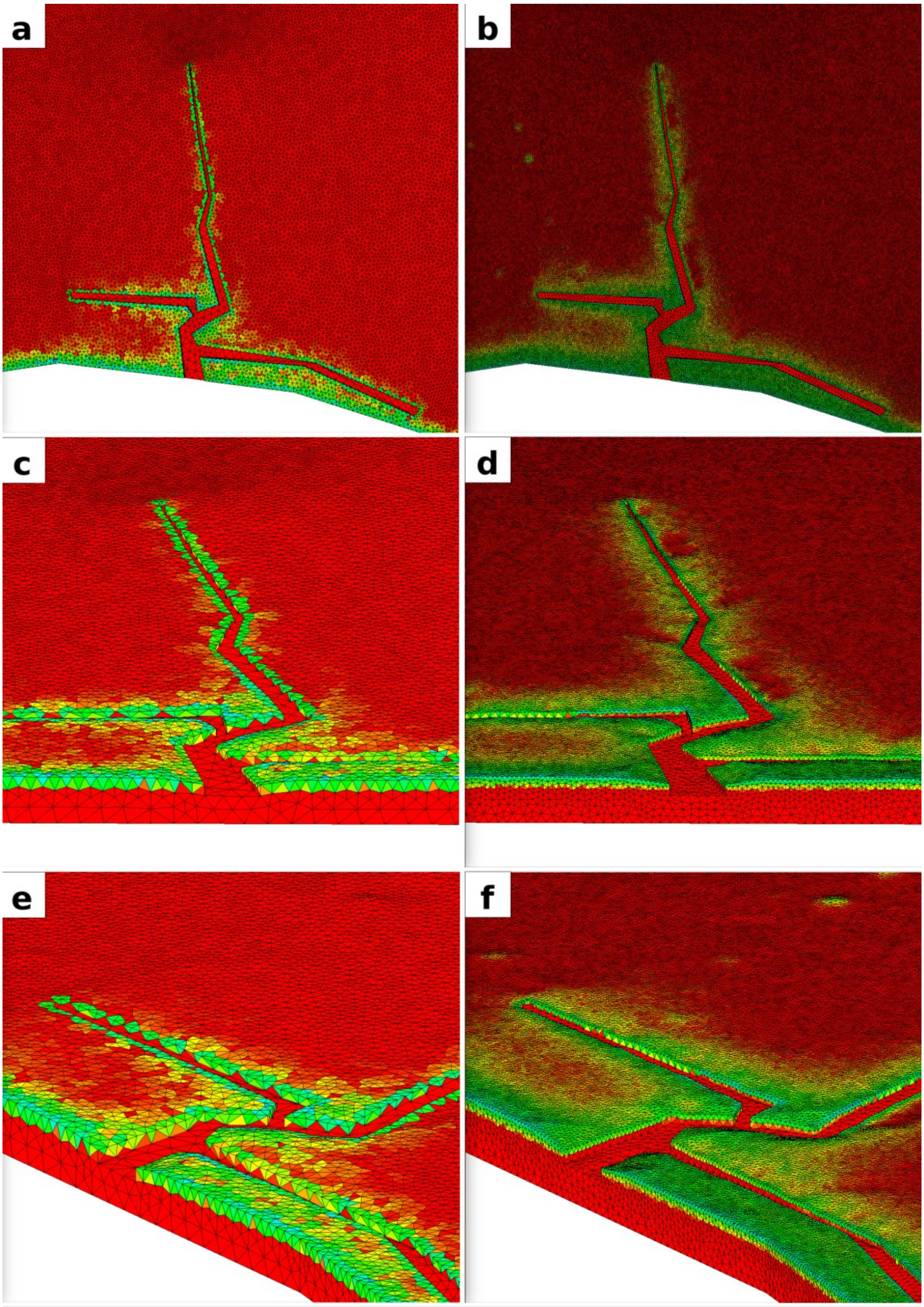

Figure 85: Impact of mesh refinement on the computed $\boldsymbol{S_w}$ *in correspondence of the lowest summer tide level. The images to the left and right columns correspond to the initial and refined mesh, respectively. Panels (a) and (b) show the mesh near the channel from a top view, panels (c) and (d) show the mesh near the channel from a front view, and panels (e) and (f) show the mesh near the channel from a side view.*

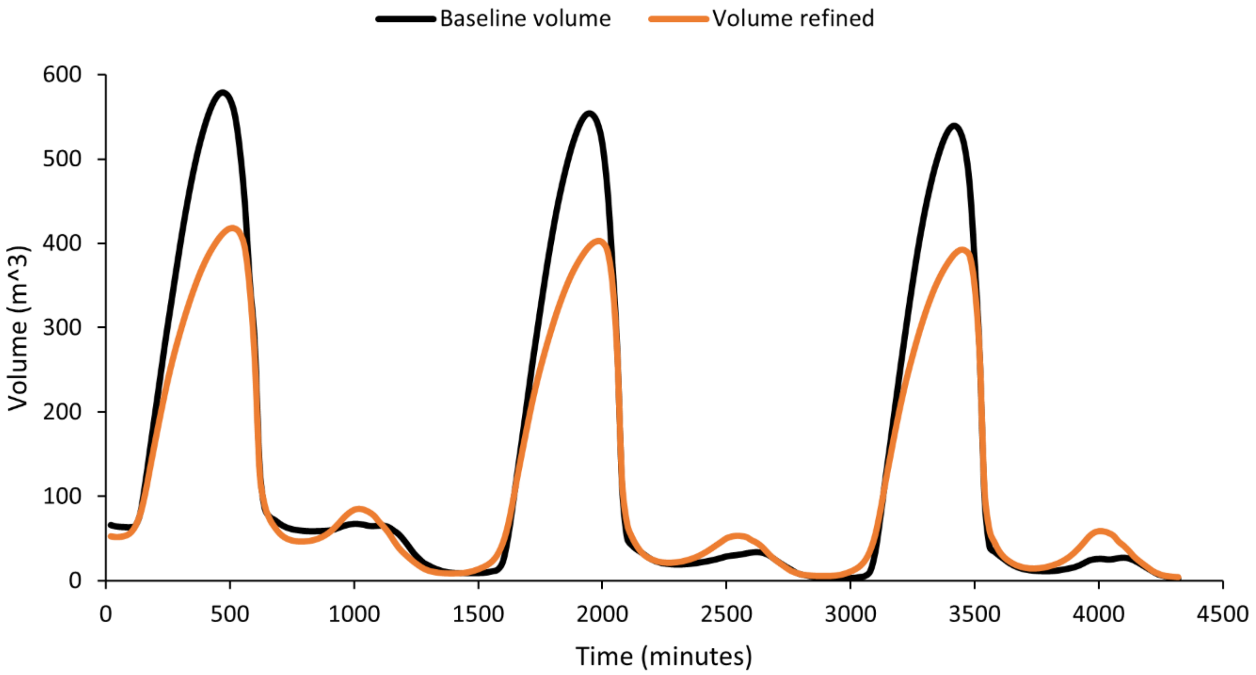

Figure 86: Temporal evolution of the volume of elements exhibiting a saturation degree between 0 and 0.99 for the baseline and refined meshes.

5.5.3 Sensitivity analysis on hydraulic condictivity

Finally, a sensitivity analysis on hydraulic conductivity was performed. In the previous simulations, the baseline value of $K = 7 \cdot 10^{-4}$ m/s was used. To evaluate how changes in hydraulic conductivity affect saturation, two additional simulations (focusing on case A3) were conducted with an order of magnitude lower $K = 7 \cdot 10^{-5}$ m/s and higher $K = 7 \cdot 10^{-3}$ m/s values. The results of this analysis are presented in Figure 87.

As expected, the series corresponding to the highest conductivity $K = 7 \cdot 10^{-3}$ m/s exhibited the largest volumes, reaching a maximum of 1532.4 m³. On the other hand, the series with the lowest conductivity reached a peak of only 212.2 m³, highlighting a drastic reduction in the extent of unsaturated marsh under low-permeability conditions. Beyond the difference in volume magnitude, the simulation with the highest hydraulic conductivity was also able to capture smaller tidal fluctuations, exhibiting minor volume peaks corresponding to small decreases in tidal height. These variations were not visible in the lower conductivity scenarios, suggesting that higher permeability not only increases the total volume drained but also enhances the system's sensitivity to tidal fluctuations. Overall, these results highlight the critical role of hydraulic conductivity in regulating both the magnitude and responsiveness of groundwater drainage in tidal marshes.

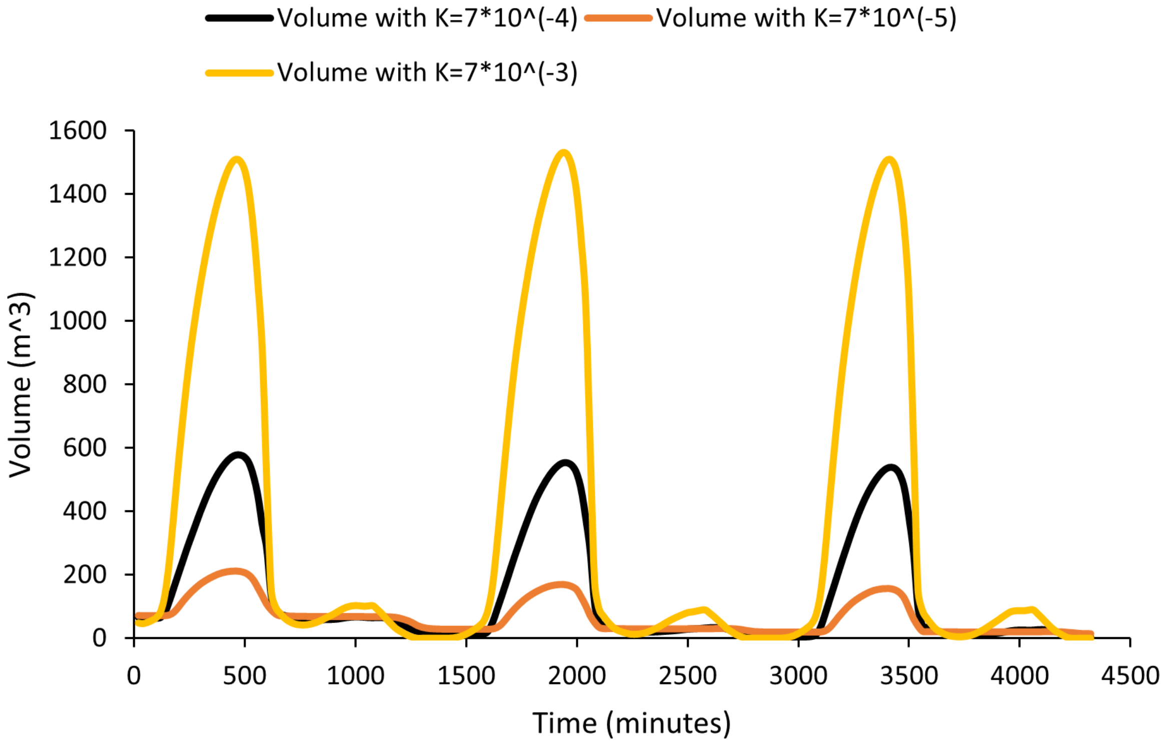

Figure 87: Temporal evolution of the volume of elements exhibiting a saturation degree between 0 and 0.99 for simulations with $K = 7 \cdot 10^{-4}\ m/s$ *(baseline),* $K = 7 \cdot 10^{-5}\ m/s$ *and* $K = 7 \cdot 10^{-3}\ m/s$.

6. Conclusions

Artificial salt marshes are constructed to restore the ecological functions and coastal defence benefits of degraded marshlands. Nevertheless, they often remain unvegetated for extended periods of time, both during sediment nourishment and after the disposal completion. These conditions are largely due to their low surface elevation and the absence of tidal creeks, which result in prolonged soil saturation and inhibit vegetation establishment. To address these limitations, recent experimental projects have focused on creating openings in marsh boundaries to encourage the development of tidal creeks and improve overall marsh functionality.

To further investigate the influence of creek networks on the saturation condition in artificial marshes, this study applied a three-dimensional variable-saturated finite-element model to simulate and visualize drainage dynamics in an artificial salt marsh in the Venice Lagoon, where marsh restoration practices have been implemented as adaptive strategies to enhance both ecological integrity and coastal resilience. Simulations were conducted using the GroundWater Simulator, initially on an idealised rectangular marsh and subsequently on a portion of the real Amira artificial marsh, assessing the impact of tidal creek networks on saturation patterns. Both sinusoidal and real tides regimes were tested, and the influence of different boundary conditions was also evaluated.

Results from the idealised marsh highlighted the impact of creek on the drainage of the inner parts of the marsh, as well as the effects of boundary conditions. In the case of a marsh bounded by the lagoon along one side only where a sinusoidal tide is applied, the presence of the creek in a barycentric position reduced the period of full saturation by 340 minutes per each semi-diurnal tidal cycle. When a real tidal regime was applied, more complex saturation patterns were observed. On the mash surface, which was fixed at 0.5 m above msl, only the highest tidal peaks induced full saturation, whereas smaller tidal fluctuations were not able to inundate the marsh. Consequently, the upper marsh still continued the desaturation process, highlighting the more intricate relationship between tidal amplitude and soil moisture dynamics. In the analysis of the Amira salt marsh, the simulations clearly indicated that the creek network facilitated the marsh drainage. The volume of elements with a saturation degree lower than 1 was calculated at each timestep, and the area influenced by drainage differed by over 250 m^3 between the simulated configurations: in the marsh with no creek, which is representative of the condition soon after the soil nourishment, this value reached a maximum of 307.3 m^3, whereas almost doubled in the configuration with a complex creek network, reaching 578.2 m^3.

Lastly, a sensitivity analysis of the model response to mesh refinement and soil hydraulic conductivity was performed. The effect of mesh refinement was evaluated to assess its impact on result accuracy, revealing a larger number of surficial elements experiencing unsaturated conditions than those obtained with the coarser mesh. However, the overall unsaturated volume was larger in the coarse mesh, as thicker elements are characterized a saturation degree less than 1. The influence of hydraulic conductivity was also examined, showing that higher hydraulic conductivity not only increases the overall unsaturated area but also improves the system's sensitivity to tidal fluctuations.

This study establishes a baseline understanding of drainage dynamics in artificial salt marshes, providing critical insights to guide restoration strategies that:

1. Enhance ecological functions;
2. Promote long-term resilience;
3. Mitigate sea level rise impacts on coastal ecosystems.

List of figures

List of tables

References

Alley, W. M., Reilly, T. E., & Franke, O. L. (1999). *Sustainability of ground-water resources* (Vol. 1186). US Department of the Interior, US Geological Survey. https://pubs.usgs.gov/circ/circ1186/pdf/circ1186.pdf

Atangana, A. (2018). Principle of groundwater flow. In *Elsevier eBooks* (pp. 15–47). https://doi.org/10.1016/b978-0-12-809670-3.00002-3

Avanzi, C., Fossato, V., Gatto, P., Rabagliati, R., Rosa Salva, P., & Zitelli, A. (1980). *Ripristino, conservazione ed uso dell'ecosistema lagunare Veneziano*. Comune di Venezia.

Baptist, M. J., Dankers, P., Cleveringa, J., Sittoni, L., Willemsen, P. W. J. M., Van Puijenbroek, M. E. B., ... & Elschot, K. (2021). Salt marsh construction as a nature-based solution in an estuarine social-ecological system. *Nature-Based Solutions*, *1*, 100005. https://doi.org/10.1016/j.nbsj.2021.100005

Barausse, A., Grechi, L., Martinello, N., Musner, T., Smania, D., Zangaglia, A., & Palmeri, L. (2015). An integrated approach to prevent the erosion of salt marshes in the lagoon of Venice. *EQA-International Journal of Environmental Quality*, *18*, 43-54. https://doi.org/10.6092/issn.2281-4485/5799

Barbero, R. S., Albani, A. D., & Bonardi, M. (2004). Ancient and modern salt marshes in the Lagoon of Venice. *Palaeogeography, Palaeoclimatology, Palaeoecology*, *202*(3-4), 229-244. https://doi.org/10.1016/S0031-0182(03)00636-9

Barbier, E. B., Hacker, S. D., Kennedy, C., Koch, E. W., Stier, A. C., & Silliman, B. R. (2011). The value of estuarine and coastal ecosystem services. *Ecological monographs*, *81*(2), 169-193. https://doi.org/10.1890/10-1510.1

Bettinetti, A., Mattarolo, F., & Silva, P. (1995). Reconstruction of saltmarshes in the Venice Lagoon. In: E. Özhan (ed.) *Proc. MEDCOAST 94 Conf., 22–27 October 1995*, pp. 921–935, Tarragona, Spain.

Boato, S., (n.d..). *Riequilibrare e riqualificare la laguna di Venezia per un futuro sostenibile*. https://unaltrolido.com/pdf/Riequilibrare%20e%20riqualificare%20la%20lacuna.pdf

Bondesan, A., & Furlanetto, P. (2012). Artificial fluvial diversions in the mainland of the Lagoon of Venice during the 16th and 17th centuries inferred by historical cartography analysis. *Géomorphologie: relief, processus, environnement*, *18*(2), 175-200. https://doi.org/10.4000/geomorphologie.9815

Bonometto, L. (2003) Ecologia applicata e ripristino ambientale nella Laguna di Venezia: analisi e classificazione funzionale delle “barene” e delle tipologie di intervento sulle barene." Comune di Venezia, Venezia.

Brambati, A., Carbognin, L., Quaia, T., Teatini, P., & Tosi, L. (2003). The Lagoon of Venice: geological setting, evolution and land subsidence. *Episodes Journal of International Geoscience*, *26*(3), 264-268. https://doi.org/10.18814/epiiugs/2003/v26i3/020

Carbognin, L., Teatini, P., & Tosi, L. (2005). Land subsidence in the Venetian area: known and recent aspects. *Geol. Appl*, *1*, 5-11. https://www.aigaa.org/aiga/public/GGA.2005-01.0-01.0001.pdf

Cohen-Shacham, E., Walters, G., Janzen, C. and Maginnis, S. (eds.) (2016). Nature-based Solutions to address global societal challenges. Gland, Switzerland: IUCN. xiii + 97pp. https://doi.org/10.2305/IUCN.CH.2016.13.en

Comune di Venezia (2024). *Archivio storico: livello di marea a Venezia – valori orari 2010.* https://www.comune.venezia.it/node/6214

Da Lio, C., Teatini, P., Strozzi, T., & Tosi, L. (2018). Understanding land subsidence in salt marshes of the Venice Lagoon from SAR Interferometry and ground-based investigations. *Remote sensing of environment*, *205*, 56-70. https://doi.org/10.1016/j.rse.2017.11.016

Day Jr, J. W., Rybczyk, J., Scarton, F., Rismondo, A., Are, D., & Cecconi, G. (1999). Soil accretionary dynamics, sea-level rise and the survival of wetlands in Venice Lagoon: a field and modelling approach. *Estuarine, Coastal and Shelf Science*, *49*(5), 607-628. https://doi.org/10.1006/ecss.1999.0522

Favero, V. 1992. Evoluzione morfologica e trasformazioni ambientali dalla conterminazione lagunare al nostro secolo. In:Conterminazione lagunare: storia, ingegneria, politica e diritto nella laguna di Venezia. Proceedings of the Conference Convegno di studio nel bicentenario della conterminazione lagunare, 14–16 March, 1991, Venezia.

Freeze, R. A., & Cherry, J. A. (1979). *Groundwater*. Englewood Cliffs, NJ: Prentice-Hall. https://fc79.gw-project.org/

Gatto, P. (1984). Il cordone litoraneo della laguna di Venezia e le cause del suo degrado. *Ist. Veneto Sci. Lett. Arti Comm. Provved. Conserv. Dif. Laguna Città Venezia Rapp. Studi*, *9*, 163-193.

Gatto, P., & Carbognin, L. (1981). The Lagoon of Venice: natural environmental trend and man-induced modification/La Lagune de Venise: l'évolution naturelle et les modifications humaines. *Hydrological Sciences Journal*, *26*(4), 379-391. https://doi.org/10.1080/02626668109490902

Gatto, P., & Previatello, P. (1974). *Significato stratigrafico, comportamento meccanico e distribuzione nella laguna di Venezia di una argilla sovraconsolidata nota come" caranto": TR 70*. CNR, Laboratorio per lo studio della dinamica delle grandi masse.

Gedan, K. B., Silliman, B. R., & Bertness, M. D. (2009). Centuries of human-driven change in salt marsh ecosystems. *Annual review of marine science*, *1*(1), 117-141. https://doi.org/10.1146/annurev.marine.010908.163930

Géhu, J. M., Scoppola, A., Caniglia, G., Marchiori, S., & Géhu-Franck, J. (1984). Les systèmes végétaux de la côte nord-adriatique italienne: leur originalité à l'échelle européenne. *Documents phytosociologiques*, *8*, 485-558.

Giupponi, C., Bidoia, M., Breil, M., Di Corato, L., Gain, A. K., Leoni, V., ... & Umgiesser, G. (2024). Boon and burden: economic performance and future perspectives of the Venice flood protection system. *Regional environmental change*, *24*(2), 44. https://doi.org/10.1007/s10113-024-02193-9

Italy. (1973). *Law No. 171 of 16 April 1973, Measures for the safeguarding of Venice* (Gazzetta Ufficiale No. 106, 21 April 1973).

Italy. (1984). *Law No. 798 of 29 November 1984: New measures for the safeguarding of Venice* (Gazzetta Ufficiale No. 337, 8 December 1984).

Italy. (1991). *Law No. 360 of 8 November 1991: Further measures for the safeguarding of Venice* (Gazzetta Ufficiale No. 270, 18 November 1991).

Italy. (1992). *Law No. 139 of 5 February 1992: Additional measures for the safeguarding of Venice* (Gazzetta Ufficiale No. 33, 10 February 1992).

ISPRA (2012). *Features of the tide*. https://www.venezia.isprambiente.it/index.php?folder_id=60&lang_id=2#:~:text=The%20meteological%20component,compared%20with%20normal%20astronomical%20oscillations.

Istituto Veneto (n.d.). *Morfologia lagunare*. https://www.istitutoveneto.org/venezia/documenti/tesi_laurea_dott/tesi_salviato/cap_1.pdf

Istituto Veneto (n.d.). *Saltmarshes*. https://www.istitutoveneto.org/venezia/divulgazione/pirelli/pirelli_2005_en/Banca_Dati_Ambientale/192.168.10.66/pirelli_new/divulgazione/valli/barene.html

Liakopoulos, A. C. (1965). Theoretical solution of the unsteady unsaturated flow problems in soils. *International Association of Scientific Hydrology. Bulletin*, *10*(1), 5-39. https://doi.org/10.1080/02626666509493368

Marani, M., Silvestri, S., Belluco, E., Ursino, N., Comerlati, A., Tosatto, O., & Putti, M. (2006). Spatial organization and ecohydrological interactions in oxygen-limited vegetation ecosystems. *Water resources research*, *42*(6). https://doi.org/10.1029/2005WR004582

Mcowen, C. J., Weatherdon, L. V., Van Bochove, J. W., Sullivan, E., Blyth, S., Zockler, C., ... & Fletcher, S. (2017). A global map of saltmarshes. *Biodiversity data journal*, (5), e11764. https://doi.org/10.3897/BDJ.5.e11764

Mitsch, W. J., & Gosselink, J. G. (2015). *Wetlands*. John wiley & sons. https://download.e-bookshelf.de/download/0000/5929/20/L-G-0000592920-0002363128.pdf

Ministero dell'Ambiente (1993). *Criteri di sicurezza ambientale per gli interventi di escavazione, trasporto e reimpiego dei fanghi estratti dai canali di Venezia (art. 4, comma 6, Legge 360/91).* https://sistemavenezia.regione.veneto.it/sites/default/files/documents/05_Moranzani/MOR_930408_ProtocolloFanghi.pdf

MOSE (2025). *Difesa ambientale*. https://mosevenezia.eu/difesa-ambientale/

MOSE (2025). *Ecosistema*. https://mosevenezia.eu/ecosistema/

Paniconi, C., & Putti, M. (1994). A comparison of Picard and Newton iteration in the numerical solution of multidimensional variably saturated flow problems. *Water Resources Research*, *30*(12), 3357-3374. https://doi.org/10.1029/94WR02046

Pétillon, J., McKinley, E., Alexander, M., Adams, J. B., Angelini, C., Balke, T., ... & Skov, M. W. (2023). Top ten priorities for global saltmarsh restoration, conservation and ecosystem service research. *Science of the Total Environment*, *898*, 165544. https://doi.org/10.1016/j.scitotenv.2023.165544

Qi, M., & Gedan, K. (2025). Tidal attenuation and poor drainage make interior microtidal marshes vulnerable to sea level rise. *Geophysical Research Letters*, *52*(19), e2025GL118637. https://doi.org/10.1029/2025GL118637

Ramsar Convention on Wetlands. (2018). Global Wetland Outlook: State of the World's Wetlands and their Services to People. Gland, Switzerland: Ramsar Convention Secretariat.

Runca, E., Bernstein, A., Postma, L., & Di Silvio, G. (1996). Control of macroalgae blooms in the Lagoon of Venice. *Ocean & coastal management*, *30*(2-3), 235-257. https://doi.org/10.1016/0964-5691(95)00065-8

Smart, M., & Viñals, M. J. (2004). *The Lagoon of Venice as a Ramsar site*. Provincia di Venezia. https://www.birdingveneto.eu/venezia/biblio/smart_e_vinals_2004.pdf

Tognin, D., D'Alpaos, A., Marani, M., & Carniello, L. (2021). Marsh resilience to sea-level rise reduced by storm-surge barriers in the Venice Lagoon. *Nature Geoscience*, *14*(12), 906-911. https://doi.org/10.1038/s41561-021-00853-7

Ursino, N., Silvestri, S., & Marani, M. (2004). Subsurface flow and vegetation patterns in tidal environments. *Water Resources Research*, *40*(5). https://doi.org/10.1029/2003WR002702

USGS, 2013. Unsaturated flow basics. https://wwwrcamnl.wr.usgs.gov/uzf/unsatflow/unsatflow.html

Van Genuchten, M.Th., 1980. A Closed-form Equation for Predicting the Hydraulic Conductivity of Unsaturated Soils. Soil Sci. Soc. Am. J. 44, 892–898. https://doi.org/10.2136/sssaj1980.03615995004400050002x

Verhoeven, J. T., Arheimer, B., Yin, C., & Hefting, M. M. (2006). Regional and global concerns over wetlands and water quality. *Trends in ecology & evolution*, *21*(2), 96-103. https://doi.org/10.1016/j.tree.2005.11.015

VITAL (2024). Segni di efficacia degli interventi sul sito pilota. https://www.v-i-t-a-l.org/it/journal/segni-di-efficacia-degli-interventi-nel-sito-pilota

Xin, P., Wilson, A., Shen, C., Ge, Z., Moffett, K. B., Santos, I. R., ... & Barry, D. A. (2022). Surface water and groundwater interactions in salt marshes and their impact on plant ecology and coastal biogeochemistry. *Reviews of Geophysics*, *60*(1), e2021RG000740. https://doi.org/10.1029/2021RG000740

Zoccarato, C., & Teatini, P. (2017). Numerical simulations of Holocene salt-marsh dynamics under the hypothesis of large soil deformations. *Advances in Water Resources*, *110*, 107-119. https://doi.org/10.1016/j.advwatres.2017.10.006

Zoccarato, C., Minderhoud, P. S., Zorzan, P., Tosi, L., Bergamasco, A., Girardi, V., ... & Teatini, P. (2022). In-situ loading experiments reveal how the subsurface affects coastal marsh survival. *Communications Earth & Environment*, *3*(1), 264. https://doi.org/10.1038/s43247-022-00600-9